UFS·UV

UNIVERSITY OF THE FREE STATE
UNIVERSITEIT VAN DIE VRYSTAAT
YUNIVESITHI YA FREISTATA

This work is licensed under a Creative Commons Attribution-NonCommercial-ShareAlike 4.0 International License.

How to cite this thesis / dissertation (APA referencing method):

Surname, Initial(s). (Date). *Title of doctoral thesis* (Doctoral thesis). Retrieved from http://scholar.ufs.ac.za/*rest of thesis URL on KovsieScholar*

Surname, Initial(s). (Date). *Title of master's dissertation* (Master's dissertation). Retrieved from http://scholar.ufs.ac.za/*rest of thesis URL on KovsieScholar*

Development of an optical thermometry system for phosphor materials.

Lucas Johannes Bartel Erasmus

Development of an optical thermometry system for phosphor materials.

by

Lucas Johannes Bartel Erasmus
Bachelor of Science Honours: Physics

Submitted in fulfilment of the requirements
in respect of the Master´s Degree

Magister Scientiae: Physics

in the
Department of Physics
of the
Faculty of Natural and Agricultural Sciences
at the
University of the Free State

Supervisor: **Professor Jacobus Johannes Terblans** (Head of Department)

Co-Supervisor: **Professor Hendrik Christoffel Swart** (SARCI Chair)

25 October 2017

This dissertation is dedicated to Anja Mari

"Of making many books there is no end,
and much study is a weariness to the flesh."

Acknowledgements

I want to give appreciation to:

- The Almighty Father, for without His Creation, Physics will be obsolete.
- My parents Mr. L.J.B. and Mrs. R. Erasmus, companion Miss. M. Ferreira, family and friends, for their continuous support.
- Prof. J.J. Terblans for his mentorship and interest throughout this study.
- Prof. H.C. Swart for his mentorship and support throughout this study.
- Prof. R.E. Kroon for his assistance with the Photoluminescence technique.
- Prof. W.D. Roos for his assistance with the X-Ray Photo-Electron Spectroscopy technique and data analysis.
- Mrs. M.H. Stander for her assistance with the language usage throughout this dissertation.
- The personnel and students at the Department of Physics (University of the Free State) for their inspiration and innovation.
- The personnel at the Electronics Division (University of the Free State) for the development of specialised electronic equipment for this study.
- The personnel at the Instrumentation Division (University of the Free State) for the development of high quality and bespoke instrumentation for this study.

Abstract

This study is focussed on the development of a system that was used to investigate the emission of thermographic phosphors at various temperatures. The photoluminescence (PL) system at the Department of Physics at the University of the Free State was studied in detail and modified for temperature measurements. Modifications include a purpose-built heating unit, used to measure and control the phosphor material´s temperature, a beam splitter together with a power meter to be used as a reference detector for the excitation source and a sample holder together with an XYZ stage that ensures position-stability and position-control for the samples throughout the measurements. A software program was developed to allow user-friendly control and automation of the modified system. The wavelength, excitation energy and temperature were calibrated.

The modified system was used to measure the emission of commercially available lanthanum oxysulphide doped with europium(III) (La_2O_2S:Eu(III)) phosphor material at different temperatures. For the thermal quenching process, the average activation energies for the emission from the $^5D_2$, $^5D_1$ and $^5D_0$ excited states were determined as 0.49 eV, 0.55 eV and 0.77 eV respectively and the average pre-exponential constant was determined as 9.5×10^7 s^{-1}. It was also shown that La_2O_2S:Eu(III) can be utilised as a temperature sensor by using the fluorescence intensity ratio of the emission from the $^5D_1$ and $^5D_0$ excited states. This worked well for the temperature range from 80 °C to 180 °C.

The optical band gap of La_2O_2S:Eu(III) was determined as 2.75 eV. It was also established that the sulphur(II) to europium(III) (Eu(III)) charge transfer band absorbs ultraviolet radiation and transfers the excited electrons to the excited states of the Eu(III) ions from where emission can take place. Lifetime of luminescence results show that the higher excited states have a double exponential lifetime that results from the emission from both the conventional Eu(III) ions and Eu(III) ions that are in the vicinity of a defect or impurity group. It was determined that in the case of the La_2O_2S:Eu(III) phosphor material, the presence of defect or impurity groups is due to the hydroxide groups that forms when the material is exposed to water vapour in the atmosphere at room temperature. The average emission decay constants of the $^5D_2$, $^5D_1$ and $^5D_0$ excited states were determined as 0.01 ms, 0.08 ms and 0.34 ms respectively.

The modified PL system was also designed to study the stability of the emission of thermographic phosphors at various temperatures. It was observed that the overall luminescence intensity of the La_2O_2S:Eu(III) increased with annealing time at a constant temperature of 400 °C. The x-ray diffraction results indicate a decrease of the strain of the lattice as a function of period of annealing which is due to the removal of defects or impurities in the crystal lattice. The reduction of hydroxide impurities as a function of annealing time was observed using both x-ray photoelectron spectroscopy and measurement of the lifetime of luminescence. The increase in luminescence intensity as a function of annealing time can therefore be attributed to the reduction of the hydroxide impurities, however it was shown that these instability effects did not have an influence on the relative luminescence intensity from the different excited levels of the phosphor material and therefore La_2O_2S:Eu(III) can be used as a stable optical temperature sensor.

Opsomming

Dié studie fokus op die ontwikkeling van ´n stelsel wat gebruik kan word vir die bestudering van die emissie van termografiese fosfors by verskillende temperature. Die Fotoluminesensie (FL) sisteem in die Fisika Departement by die Universiteit van die Vrystaat is volledig bestudeer en aangepas vir temperatuur afhanklike metings. Die aanpassings sluit in, ´n doelgeboude verhittingsisteem, wat gebruik is om die fosformateriaal se temperatuur te meet en te beheer, ´n lig-verdeler tesame met ´n intensiteitsmeter wat gebruik word as ´n verwysingsdetektor om die opwekkingsbron te monitor en ´n monsterhouer tesame met ´n XYZ staander wat posisie-stabiliteit en posisie-beheer van die monsters verseker gedurende metings. ´n Sagtewareprogram is ontwikkel om gebruikersvriendelike beheer en outomatisering van die gewysigde stelsel moontlik te maak. Die golflengte, opwekkingsintensiteit en temperatuur is gekalibreer.

Die aangepaste stelsel is gebruik om die emissie te meet by verskillende temperature van die kommersiële fosfor, lantaanoksisulfied wat gedoteer is met europium(III) (La_2O_2S:Eu(III)). Vir die termiese kwyning proses is die gemiddelde aktiveringsenergie van die $^5D_2$, $^5D_1$ en $^5D_0$ opgewekte toestande bepaal as 0,49 eV, 0,55 eV en 0,77 eV onderskeidelik, terwyl die gemiddelde voor-eksponensiële-konstante bepaal is as 9.0×10^7 s^{-1}. Dit is ook bepaal dat La_2O_2S:Eu(III) as ´n temperatuursensor gebruik kan word, deur gebruik te maak van die fosforiese-intensiteitsverhouding van die emissie vanaf die $^5D_1$ en $^5D_0$ opgewekte toestande. Die werk goed vir die temperatuur gebied vanaf 80 °C tot 180 °C.

Die optiese bandgaping van La_2O_2S:Eu(III) is bepaal as 2,75 eV. Dit is vasgestel dat die swawel(II) na europium(III) (Eu(III)) ladingsoordragband ultravioletstraling absorbeer en dra die opgewekte elektrone oor na die opgewekte toestande van die Eu(III)-ione van waar emissie kan plaasvind. Die leeftyd van elke oorgang is ook bestudeer en dit is waargeneem dat die hoër opgewekte toestande dubbele eksponensiële leeftye het. Die rede hiervoor is emissie wat afkomstig is van die konvensionele Eu(III)-ione, asook die Eu(III)-ione wat in die omgewing van onsuiwerhede is. Dit is bevind dat in die geval van La_2O_2S:Eu(III) fosformateriaal, die teenwoordigheid van defekte of onsuiwerhede afkomstig is vanaf hidroksiedgroepe wat vorm wanneer die materiaal by kamertemperatuur blootgestel word aan waterdamp in die atmosfeer.

Die gemiddelde emissieleeftydkonstantes van die $^5D_2$, $^5D_1$ en $^5D_0$ opgewekte toestande is bepaal as 0,01 ms, 0,08 ms en 0,34 ms respektiewelik.

Die aangepaste FL stelsel is ook ontwerp om die emissie-stabiliteit van termografiese fosfors by verskillende temperature te bestudeer. Daar is opgemerk dat die algehele fosforiese-intensiteit van die La_2O_2S:Eu(III) toeneem met uitgloeityd by ´n temperatuur van 400 °C. Die x-straaldiffraksie resultate dui op die afname van die kristalroosterspanning as ´n funksie van uitgloeityd wat te wyte is aan die verwydering van defekte of onsuiwerhede in die kristalrooster. Die vermindering van hidroksieddefekte as ´n funksie van uitgloeityd is waargeneem met behulp van beide x-straalfoto-elektron-spektroskopie en ook die meting van leeftyd van luminessensie. Die toename in fosforiese-intensiteit as ´n funksie van uitgloeityd kan daarom toegeskryf word aan die vermindering van die hidroksieddefekte. Dit is egter vasgestel dat dié onstabiliteits-effekte nie ´n invloed op die fosforiese-intensiteitsverhouding van die fosformateriaal het nie en die materiaal kan dus as suksesvolle optiese-temperatuursensor benut word.

Key terms

Thermographic phosphors
Lanthanum oxysulphide doped with europium(III)
Photoluminescence
Software program
Thermal quenching
Activation energy
Intensity ratio
Emission stability
Hydroxide impurities
Optical temperature sensor

Abbreviations

Throughout this dissertation the following terms are abbreviated as follow:

Arbitrary unit	-	a.u.
Carbon	-	C
Copper	-	Cu
Europium(III)	-	Eu(III)
Fluorescence intensity ratio	-	FIR
Full width at half maximum	-	FWHM
Gold	-	Au
Hydrogen(I)	-	H(I)
Lanthanum(III)	-	La(III)
Lanthanum hydroxide	-	$La(OH)_3$
Lanthanum oxide	-	La_2O_3
Lanthanum oxysulphide	-	La_2O_2S
Lanthanum oxysulphide doped with europium(III)	-	La_2O_2S:Eu(III)
Oxygen(II)	-	O(II)
Photoluminescence	-	PL
Photomultiplier tube	-	PMT

Sulphur(II)	-	S(II)
X-ray diffraction	-	XRD
X-ray photoelectron spectroscopy	-	XPS

Table of Content

1. Introduction

It is generally known that the energy-to-light conversion efficiency of some inorganic phosphor materials is temperature dependent and therefore gives these phosphor materials their temperature sensing characteristics. Phosphor materials that exhibit this characteristic are also known as thermographic phosphors [1]. A generic phosphor thermometry system consists of an excitation source that is used to stimulate the phosphor material that is bonded to the surface of interest. One or multiple of the emission and/or absorption properties of the phosphor material is then analysed and compared to pre-calibrated data to determine the temperature of the surface in question. This provides a non-contact optical alternative for measuring temperature in contrast to other conventional techniques and can therefore also be employed in systems where other thermographic techniques are not suitable [2].

1.1 Research objectives

The main objective of this study was to develop a system that can be used to measure the photoluminescence of thermographic phosphors at various temperatures. The photoluminescence (PL) system at the Department of Physics at the University of the Free State was studied in detail and modified. Modifications include a purpose-built heating unit, used to measure and control the phosphor material´s temperature, a beam splitter together with a power meter to be used as a reference detector for the excitation source and a sample holder together with an XYZ stage that ensures position stability and position control for the samples throughout measurements. A software program was also developed to allow user-friendly control and automation of the modified system. This system was modified in such a fashion to allow the direct comparison of emission at different temperatures. The modified system was used to measure the emission of commercially available lanthanum oxysulphide doped with europium(III) (La_2O_2S:Eu(III)) phosphor powder at different temperatures.

La_2O_2S:Eu(III) phosphor material was chosen because it is a well-tested thermographic phosphor as shown in previous studies [2] [3] [4]. To obtain a better understanding of the mechanism behind the photoluminescence process, the absorption, charge transfer bands and lifetime properties of this material were studied by using the ultraviolet-visible and fluorescence spectroscopy techniques. The modified PL system was used to study the mechanism of the photoluminescence process and to determine if the emission properties of this material could be used for optical thermometry, and if possible the necessary universal pre-calibrated data. Another objective of this study was to develop the above-mentioned PL system to allow the study of the stability of the emission of thermographic phosphors at various temperatures. The emission stability results were investigated with the aid of the structural, chemical and optical properties by utilising respectively the X-ray diffraction (XRD), X-ray photoelectron spectroscopy (XPS) and fluorescence spectroscopy techniques. The structural properties that were measured include the structure, strain and crystallite size, while the chemical environment of the lanthanum (La) and oxygen (O_2) atoms were studied together with the decay of luminescence from the higher exited states.

1.2 Layout of this dissertation

In this dissertation, Chapter 2 provides a detailed theory and literature review of the mechanism behind the photoluminescence properties of phosphor materials in general, which includes the absorption of radiation, emission and lifetime of luminescence processes. The mechanism for the thermal quenching effect is also presented and explained in terms of the configurational coordinate model. The method behind the different thermographic techniques is also discussed together with possible applications. Included in Chapter 2 is optical, structural and chemical information about the lanthanum oxysulphide (La_2O_2S) host material and the optical properties of the europium(III) (Eu(III)) activator ion. Lastly the thermographic properties of the La_2O_2S:Eu(III) phosphor material are discussed together with the properties predicted to be observed during experimentation.

In Chapter 3, the experimental procedure and methodology are given for each technique used in this study. The different components of the PL system at the Department of Physics at the University of the Free State are discussed in detail and the necessary modifications that were designed and developed to achieve the research objectives, are shown. Details of the software program that was developed are also given together with procedures followed for the necessary excitation energy, wavelength and temperature calibrations. Ultraviolet-visible and fluorescence spectroscopy, XRD and XPS techniques are also discussed while details are given about the different calibrations that were necessary. Included at the back of the dissertation are the apparatus specifications (Appendix A) and programing code (Appendix B) that are referenced throughout this chapter. Included with this dissertation is a compact disc which contains a copy of the developed software program and the full programming code.

Chapter 4 focusses on the experimental results that were obtained by the different techniques used in this study. After the analysis of these results the measured optical, structural and chemical properties of the La_2O_2S:Eu(III) phosphor material are compared to previous studies and interpreted in accordance with theory as explained in Chapter 2. Possible reasons are given in the cases where the experimental results do not agree with the predicted theoretical results. In Chapter 5 conclusions are made which evaluate if the research objectives of this study have been achieved and suggestions are given for possible future studies. Included in Chapter 6 is a bibliography that is referenced throughout the dissertation.

2. Theory and Literature Review

This chapter aims to give the necessary background and theory of this study and it also aids in the explanation of some of the observed results in Chapter 4. This chapter is divided into two sections, the first being the general theory behind the photoluminescent properties of phosphor materials. This includes detailed discussions of the absorption of radiation, excitation, emission of radiation and emission lifetime processes. The theory and mechanism for the thermal quenching process is also explained and lastly the different thermographic techniques are discussed together with possible applications. The second section discusses the mechanism behind the photoluminescence process specifically for the La_2O_2S:Eu(III) phosphor material. The luminescent, structural and chemical properties of the host material are discussed with the spectral properties of the activator ion explained separately. Lastly the thermographic properties of the La_2O_2S:Eu(III) phosphor material are discussed. The theoretical values and results of the different properties of the La_2O_2S:Eu(III) phosphor material that was obtained from literature, are given throughout this section.

2.1 Phosphor materials

A phosphor material is a synthetic substance that displays the characteristic of luminescence. Luminescence is the name of the process where energy is absorbed by a material which is then followed by the subsequent emission of light [5]. Phosphors are usually composed of a relatively small amount of activator ions that is distributed inside a transparent microcrystalline matrix that is also referred to as the host. Usually only the host is considered as a medium for the activator and the activator is regarded as the centre of luminescence [6]. In this study, a rare-earth ion is used as an activator, where these ions replace some of the ions of the host lattice. Rare-earth ions act as centres of luminescence because of the $4f$ electrons in their inner shell that have electronic energy levels that can possibly induce excitation and/or luminescence processes in the visible region. Luminescence is divided into two parts, namely the processes of absorption of excitation energy and the process of the emission of photons. There are different types of luminescence that are defined by the excitation source used. Some examples of the different types of luminescence, together with their source of excitation, include [7]:

Bioluminescence	-	Luminescence that is generated by a living organism
Chemiluminescence	-	Chemical reaction induced luminescence
Electroluminescence	-	Electrical current induced luminescence
Cathodeluminescence	-	Electron beam induced luminescence
Photoluminescence	-	Photon induced luminescence
Thermoluminescence	-	Heat induced luminescence

This study is concentrated mainly on photoluminescence. Photoluminescence in phosphors is the result of a process where a sample is excited by the electromagnetic radiation which causes electrons to move from a lower energy state to a higher energy state. After some time, the electrons return to the lower energy state which can result in an emission of photons which are observed as light [8].

2.1.1 Absorption of radiation

When a phosphor material is irradiated with electromagnetic radiation there is a possibility that transmission, reflection and/or absorption can occur. In this study absorption is mainly of interest because it causes electronic or lattice transitions in phosphor materials, by electrons that are excited from lower to higher energy states. The intensity of the absorption is determined by the absorption coefficient $\alpha(hv)$ that is described by:

$$\alpha(hv) = A\sum p_{if}n_i n_f \qquad \textbf{\textit{2.1}}$$

where A is related to the mass of the electrons, p_{if} is the transition probability between the ground and excited states, n_i is the number density of electronic states in the ground state that are occupied by electrons and n_f the number density of electronic states in the excited state that are not occupied by electrons.

Direct allowed transitions

Figure 2.1 shows an example of a material of which the minimum energy between the top of the valence band and the bottom of the conduction band have the same momentum k. In this special case, the electrons in the valence band with energy E_i, are excited directly to the conduction band with energy E_f.

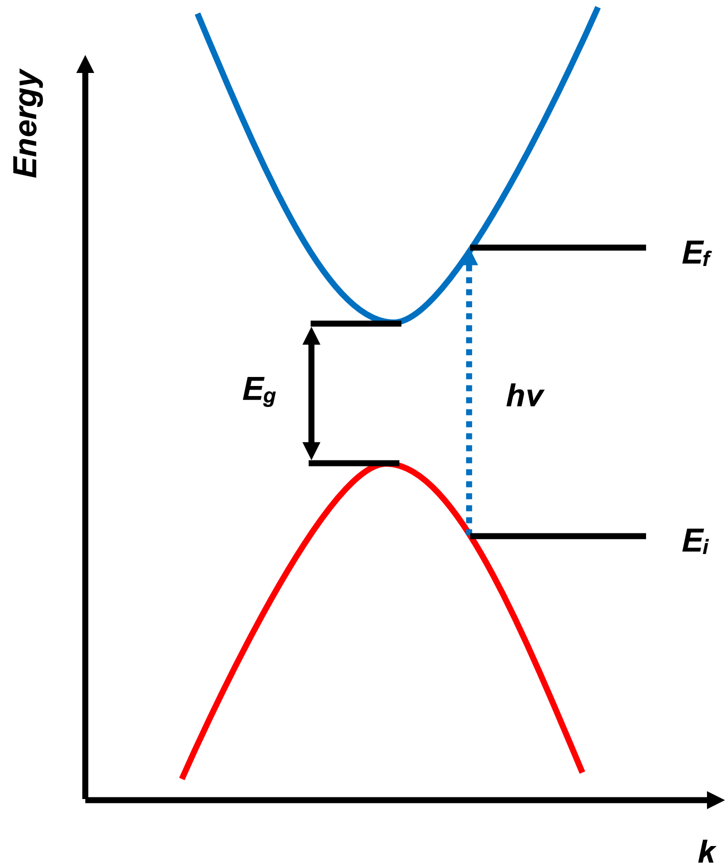

Figure 2.1: *Absorption due to a direct transition.*

In this case the magnitude of the absorption is determined by the absorption coefficient that is described by:

$$\alpha(hv) = A\left(hv - E_g\right)^{1/2} \qquad \textbf{2.2}$$

where E_g is the band gap, h is Planck´s constant, v the frequency of the absorbed electromagnetic radiation and A is related to the effective masses of the electrons and holes which is described by Equation 2.3.

$$A = \left[\frac{e^2}{nch^2m_e^*}\right](2m_r)^{3/2} \qquad \textbf{2.3}$$

In this equation e represents the charge of an electron, c the speed of light, m_e^* the effective mass of the charge carriers and m_r the reduced mass of the charge carriers. It is important to note that n is dependent on the nature of the transition as explained in the following sections [6]. For direct allowed transition $n = 1/2$. [9]. The band gap of a material can be determined experimentally due to the fact that the absorption coefficient increases from the edge of the band gap.

Direct forbidden transitions

In some materials, the transition at $k = 0$ is forbidden by a selection rule which results in $n = 3/2$ and the absorption coefficient to be described by Equation 2.4 [9].

$$\alpha(hv) = A\left(hv - E_g\right)^{3/2} \qquad \mathbf{2.4}$$

Indirect transitions

Figure 2.2 shows an example of a material where both the energy and momentum of the electrons are changed in the excitation process. This is due to the minimum band gap being between two states with different momentum k values. In this case, an electron is excited by a photon that provides the necessary energy E_g for the transition and is then assisted by a phonon that provides the necessary momentum E_p. This is known as an indirect band gap. Due to the higher-order stochastic process, the transition probability decreases for materials with indirect band gaps. For this type of transition $n = 2$ and the absorption coefficient is given by:

$$\alpha(hv) = A\left(hv - E_g + E_p\right)^2 \left(\exp\left(\frac{E_p}{kT}\right) - 1\right)^{-1} \qquad \mathbf{2.5}$$

where k Boltzmann´s constant and T the temperature of the material [6].

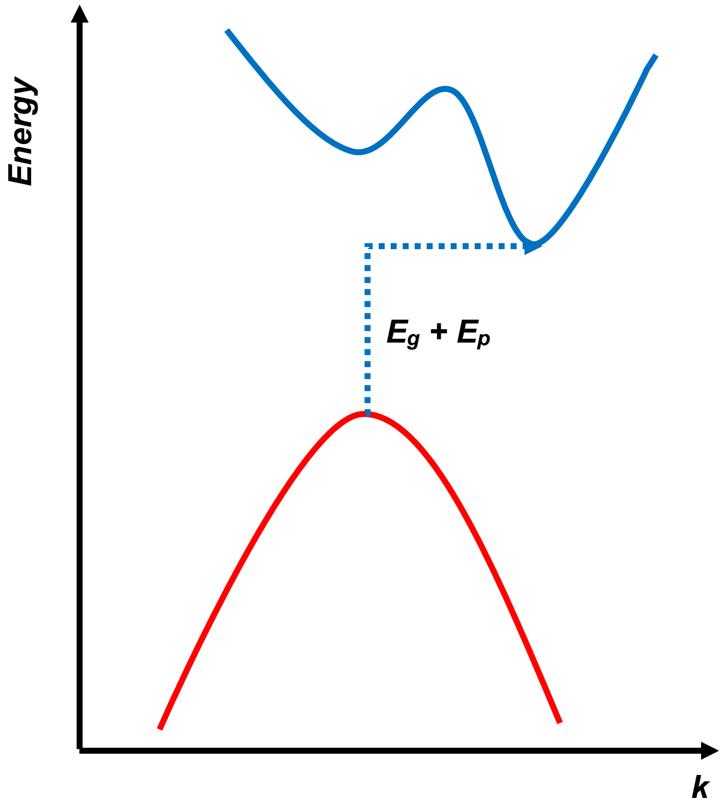

Figure 2.2: *Absorption due to an indirect transition.*

2.1.2 Emission of radiation

An excited electron can return to its ground state by either releasing energy in the form of the emission of electromagnetic radiation and/or thermal energy that is dissipated by lattice vibrations. Luminescence is observed when the excited electron releases energy in the form of electromagnetic radiation. The intensity of this light emission R is expressed by the following equation.

$$R = A\sum p_{ul} n_u n_l \qquad \textbf{2.6}$$

In Equation 2.6, p_{ul} is the transition probability between the excited and ground states, n_u is the number density of electronic states in the ground state that are occupied by electrons and n_i is the number density of electronic states in the ground state that are not occupied by electrons. From this equation, there can be seen that emission has similarities with absorption that is described by Equation 2.1. Equation 2.6 is written as follows:

$$R = A(hv - E_g + E_p)^{1/2}\exp\left(-\frac{hv - E_g}{kT}\right) \qquad \textbf{2.7}$$

from where it is observed that at a given temperature emission mostly occurs near the conduction band minimum where the band gap E_g is at its smallest. Photon emission from higher energy states is improbable because it requires the absorption of thermal phonons. In the case of an indirect transitions, where the conduction band minimum and valence band maximum have different momentum values, the photon emission is accompanied by the emission of a phonon [6].

2.1.3 Lifetime of luminescence

Luminescence in phosphors is categorised into two main groups according to the length of time the luminescence persists. The length of time that distinguishes the two groups, is not clearly defined, but usually an after-glow in materials, persisting for longer than 100 milliseconds and therefore visible to the human eye, is called phosphorescence [6]. Phosphorescence is a form of luminescence where all the electrons do not immediately emit a photon after excitation. This delay in the relaxation process is due to the excitation of the electrons to a higher energy state that can cause a change in the spin state of a centre or trap in a quasi-stable state that in return causes quantum mechanically forbidden transitions to occur [10]. Fluorescence on the other hand is a form of luminescence where light is emitted during excitation in which the emission decay is less than 100 ms after termination of the excitation source. This luminescence occurs due to an orbital electron of a luminescence centre that relaxes to the ground state as an allowed transition [10]. Luminescence intensity $I(t)$ of the decay process after the termination of the excitation source at time t for a single process is represented by

$$I(t) = I_0 \exp\left(-t/\tau\right) \qquad \textbf{2.8}$$

where I_o is the luminescence intensity of the process at $t = 0$ and τ is the emissions decay constant that is defined as the elapsed time for the luminescence intensity to decrease by a factor e^{-1} of the luminescence intensity of the process at $t = 0$. After mathematical manipulation, this expression can also be written as follows [11].

$$\ln\big(I(t)\big) = -\frac{t}{\tau} + \ln I_0 \qquad \textbf{\textit{2.9}}$$

Luminescence decay can also occur through multiple different processes simultaneously. These processes have different probabilities of occurring and therefore they occur at different rates. In the case of N number of process the luminescence decay is represented as the sum of individual processes [12].

$$I(t) = \sum_{i=1}^{N} \left[I_0(\tau_i) \left(\exp \frac{-t}{\tau_i} \right) \right] \qquad \textbf{\textit{2.10}}$$

The fraction of the fluorescence intensity for the different emitters that is being governed by the different processes f, are determined by the values obtained in the fit of Equation 2.10 by utilising Equation 2.11 [12].

$$f_i = \frac{I_0(\tau_i)\, \tau_i}{\sum I_0(\tau_i)\, \tau_i} \times 100\% \qquad \textbf{\textit{2.11}}$$

The average emission decay constant of the different processes $\langle \tau \rangle$ is calculated by the following equation [13].

$$\langle \tau \rangle = \frac{\sum I_0(\tau_i)\, {\tau_i}^2}{\sum I_0(\tau_i)\, \tau_i} \qquad \textbf{\textit{2.12}}$$

To solve Equation 2.10 and determine the emission decay constants of the different process, special software is used as explained in the Experimental Techniques and Methodology chapter.

2.1.4 Configurational coordinate model

The configurational coordinate model is used to describe optical properties together with the effect of lattice vibrations on a localised centre. For simplicity, this model only focusses on one luminescent ion and the nearest lattice site and ignores the effect of the distant ions. This allows the large number of actual lattice vibrational modes to be approximated by a combination of specific coordinates which are called the configurational coordinates. An example of such a model is shown in Figure 2.3. The horizontal axis represents the configurational coordinate which is the measure of the ion′s and electron′s positions in the lattice and the vertical axis serves as a measure of energy. The diagram shows the different states as parabolas which are called potential curves. This model explains the optical properties of a centre with the aid of these potential curves where they represent the total energy of the centre as a function of the configurational coordinate, for both the ground and excited state. The total energy in this case is the sum of the ion and electron energy. This model can aid in the explanation of several aspects, which include [6]:

- Stokes´ law, which states that in most cases the energy of absorption is higher than the energy of emission and the difference is known as the Stokes´ shift.
- The widths of the emission and absorption bands and how they are influenced by temperature.
- Thermal quenching of luminescence which will be discussed in the next section.

In Figure 2.3 the optical absorption A → B and optical emission C → D pathways are indicated by the vertical broken arrows. It is noted that the nucleus of the emitting ion stays roughly at the same nuclear configuration during these optical processes. This is described by the Born-Oppenheimer approximation, which states that electron transitions take place at a faster rate than the nucleus can respond, because of the fact that the atomic nucleus is much heavier than the electron [14]. Assuming the bonding force between the nearest neighbour ion and the luminescence centre is expressed by Hooke´s law and the deviation of the ions from the equilibrium position is taken as the configurational coordinate that is called Q, then the total energy of the ground state U_g and the excited state U_e is described by Equation 2.13 and Equation 2.14 respectively.

$$U_g = K_g \frac{Q^2}{2} \qquad \textbf{2.13}$$

$$U_e = K_e \frac{(Q - Q_0)^2}{2} + U_0 \qquad \textbf{\textit{2.14}}$$

In these equations K_g and K_e are the chemical bond´s force constants, Q_0 the interatomic distance from the equilibrium position of the ground state and U_0 the total energy when $Q=Q_0$. This shift in the equilibrium positions between the ground and excited states as shown in Figure 2.3, is the origin of Stokes´ shift and is caused by the configuration coordinate of the system being different between the ground and excited states.

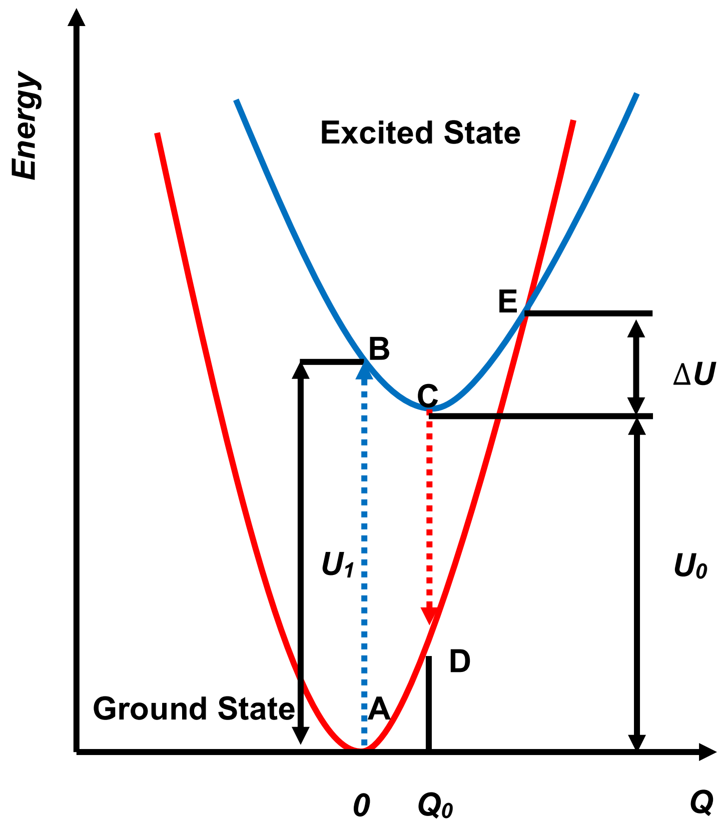

Figure 2.3: *Schematic of a configurational coordinate model.*

The optical absorption process occurs from the equilibrium point of the ground state at point A to point B in the excited state as seen in Figure 2.3. From this point, the average rate for the electron in the excited state to lose its energy in the form of lattice vibrations is about 10^{13} s^{-1} while the average rate for light emission to occur is about 10^{9} s^{-1}. Therefore, an electron at point B is most likely to relax non-radiatively to the excited states´ equilibrium position at point

C. A photon is emitted in the radiative process from point C to D and lastly the electron relaxes non-radiatively from point D to A which then completes the cycle [6]. At temperatures above 0 K the electron oscillates around the equilibrium position along the configurational curve. These oscillations are responsible for the spectral width of the absorption and emission transitions. When the temperature is sufficiently high there is a possibility for the excited electron to lose its energy exclusively in the form of lattice vibrations. This effect is known as thermal quenching and is explained in the next section.

2.1.5 Thermal quenching

When two configurational coordinate curves intersect each other such as in Figure 2.3 there is a possibility for the electrons in the excited states, aided by the thermal energy ΔU, to cross the intersection point E. Once the electron reaches this point it can move to the ground state by releasing energy non-radiatively through the dissipation of heat through the lattice [15]. When this occurs less electrons in the excited states release energy radiatively and the intensity of the luminescence decrease. This phenomenon is known as thermal quenching. Assume the number of excited luminescence centres per unit volume is represented by n^* and the radiative and non-radiative transition rates are represented by W_R and W_{NR} respectively, then the rate equation for n^* is given by:

$$\frac{dn^*}{dt} = -(W_R + W_{NR})n^* \qquad \textbf{2.15}$$

which has the following solution.

$$n^*(t) = n_0^* \exp[-(W_R + W_{NR})t] \qquad \textbf{2.16}$$

In this equation n_0^* is the number of excited luminescence centres per unit volume at $t = 0$ when excitation is terminated and t the time elapsed after the termination of the excitation. Since the intensity of emission is proportional to the number of excited luminescence centres per unit volume, it follows from Equation 2.8 and Equation 2.16 that:

$$\tau = (W_R + W_{NR})^{-1} \qquad \textbf{2.17}$$

The luminescence efficiency η is defined as the fraction of electrons that undergo radiative transitions compared to the total number of electrons that undergo radiative or non-radiative transitions, as shown by Equation 2.18 [6].

$$\eta = \frac{W_R}{W_R + W_{NR}} \qquad \textbf{\textit{2.18}}$$

The non-radiative transition probability is mostly ruled by thermal quenching processes like the emission of energy into lattice vibrations but can also be affected by resonant energy transfers between optical centres that is known as concentration quenching. Thermal relaxation can be explained with the aid of Figure 2.3 where the centre is thermally activated from the point of the lowest energy of the excited state at point C, to the crossing point where the electronic states of the ground and excited states are intermixed at point E. Lastly the electrons are thermally released from the crossing point to the ground state at point A. The necessary energy ΔU is required to excite the centre from the lowest energy of the excited state to the crossing point. This is often referred to as the thermal activation energy. Therefore, the non-radiative transition probability of a centre through thermal activation is expressed as follows.

$$W_{NR} = s \exp\left(\frac{-\Delta U}{kT}\right) \qquad \textbf{\textit{2.19}}$$

In this equation k represents Boltzmann´s constant and T is the temperature. As Equation 2.19 suggest this type of non-radiative transition is strongly temperature dependent. The term s is the product of transition probability between the ground state and excited state and the frequency at which the excited state attempts to reach the intersection point. That is why s is referred to as the frequency factor. This quantity is only relatively weakly dependent on temperature and can therefore be treated as a constant. It typically has a value in the order of 10^{13} s^{-1}. By substituting the non-radiative transition probability of Equation 2.18 with Equation 2.19, the luminescence efficiency is expressed as follows.

$$\eta = \left[1 + \frac{s}{W_R} \exp\left(\frac{-\Delta U}{kT}\right)\right]^{-1} \qquad \textbf{\textit{2.20}}$$

Generally, emission efficiency and lifetime decrease with an increase in temperature as Equation 2.20 and Equation 2.17 suggests. This phenomenon is known as thermal quenching [6]. Thermal quenching can also occur when the configurational coordinate model takes the form as can be seen in Figure 2.12 where the parabolas from the same configuration is crossed by a third parabola from a different configuration [15]. This extra parabola is often referred to as the charge transfer state and is associated with the host lattice. According to theory a phosphor´s configurational coordinate model has a charge transfer state present when there is a difference between the equilibrium positions of the ground and excited states of the host lattice and activator ion. This is usually the case when the host lattice cation radius is larger than the activator ion radius of the phosphor material [16]. This thermal quenching effect of some phosphor materials can be utilised as a thermographic technique as explained in the next section.

2.1.6 Thermographic techniques

Phosphor materials are classified as thermographic if their emission and/or absorption changes as a function of temperature. There are several ways the temperature dependence of phosphor materials are manifested in their emission and/or absorption of light. To characterise the luminescence temperature dependence of the phosphor materials the following properties are measured: emission intensity, emission rise and decay time, emission line shift and width changes and absorption spectral features [2]. A short summary of each of the techniques used to measure these properties is given below together with the method used for possible temperature sensing.

Fluorescence intensity and fluorescence intensity ratio technique

When a light source excites a phosphor material an equilibrium between excitation and relaxation is reached which results in a steady emission intensity that is emitted by the phosphor material. A change in temperature of the material can influence the emission intensity that is observed, as illustrated by an example in Figure 2.4. This effect could be due to a variety of mechanisms including thermal quenching, thermalisation and multiphonon relaxation. These mechanisms can be solely responsible for the observed effect or a variety of mechanisms could be at work. By calibrating the fluorescence intensity response of the material as a function of temperature, temperature measurements can be made by observing the emission intensity and comparing it with the calibration data [1].

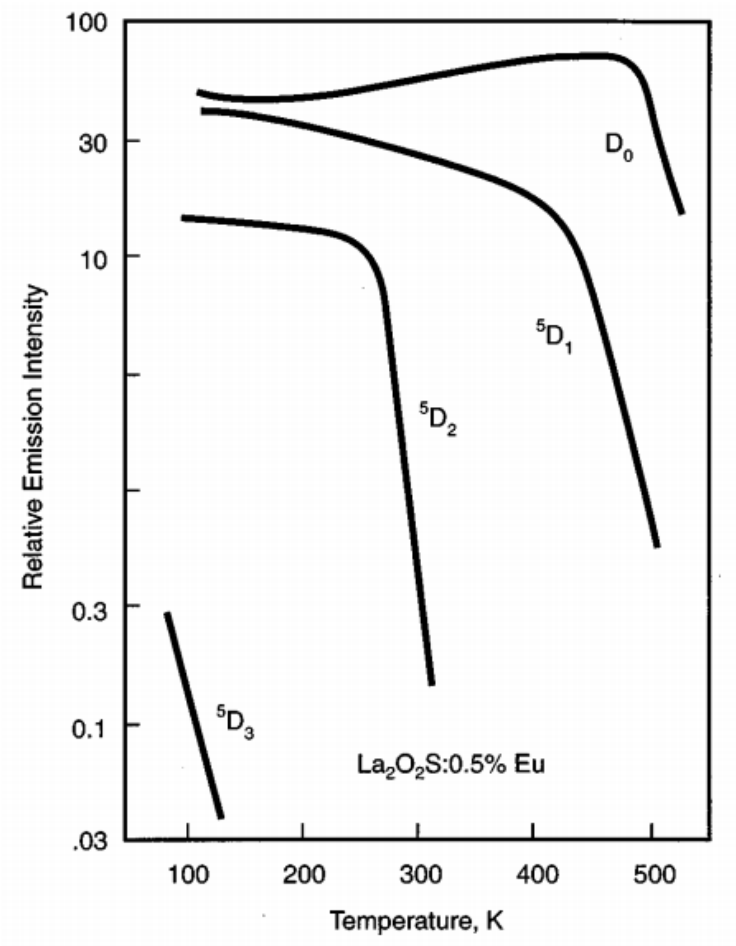

Figure 2.4: *Emission intensity as a function of temperature for the different excited states of La_2O_2S:Eu(III)* ***[2]***.

The fluorescence intensity based approach generally requires the simplest instrumentation and is therefore relatively affordable to implement. However, since the absolute intensity of emission is also a function of other variables, difficulty arises in maintaining the intensity calibration. These variables include, excitation source instabilities, non-homogenous illumination of material, detector sensitivity, distance and angle of detector, etcetera. [1]. A better approach is the fluorescence intensity ratio (FIR) technique that eliminates most of these variables. The FIR technique uses the intensity ratio between two or more fluorescence emission lines at different wavelengths of a phosphor material to determine calibration data. The relative intensity change between the emission lines can be analysed and with the use of the calibration data the unknown temperature can be determined. Phosphor materials that are good candidates for thermographic phosphors therefore must exhibit multiple emission response, with some emission lines being less or more sensitive to a change in temperature [1].

Fluorescence lifetime technique

When a phosphor is excited by a pulsed source, the resulting fluorescence is observed as the fluorescence intensity rises and decays as a function of time. This is known as the rise and decay lifetime of the fluorescence. The decay lifetime of some phosphor material can change as a function of temperature due to a change in the non-radiative transition probability as illustrated by Equation 2.17. Therefore, these materials is useful for thermometry. Figure 2.5 illustrates an example of a change in decay times of different emission peaks, as a function of temperature.

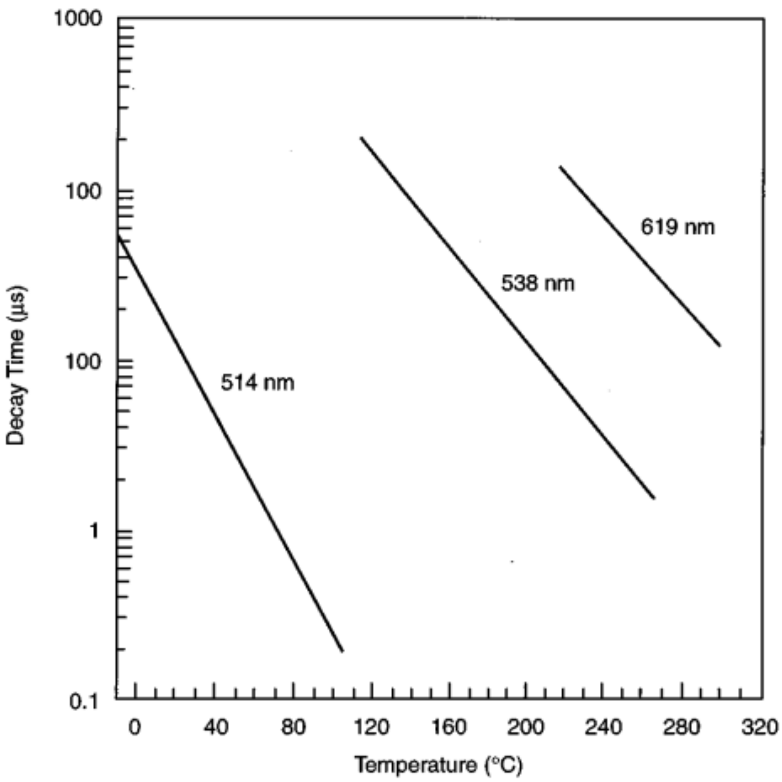

Figure 2.5: *Fluorescence decay time as a function of temperature of different emission peaks of La_2O_2S:Eu(III)* ***[2]***.

The fluorescence lifetime approach does not suffer the same disadvantages as the intensity based approach because rise and decay rates can be measured in terms of time and therefore offers less uncertainty since this quantity can generally be determined with greater accuracy than optical intensities. However, to measure the fluorescence intensity rise and decay, a fast analog-to-digital converter is needed, which is expensive [2].

Fluorescence line shift and line width technique

Each fluorescence emission line of a phosphor is characterised by a wavelength for which the intensity is a maximum. Emission line shifts may occur with a change in temperature as shown in an example in Figure 2.6. This can occur due to a shift of the coordination of the activator ion or due to the expanding of the host lattice at high temperatures [2].

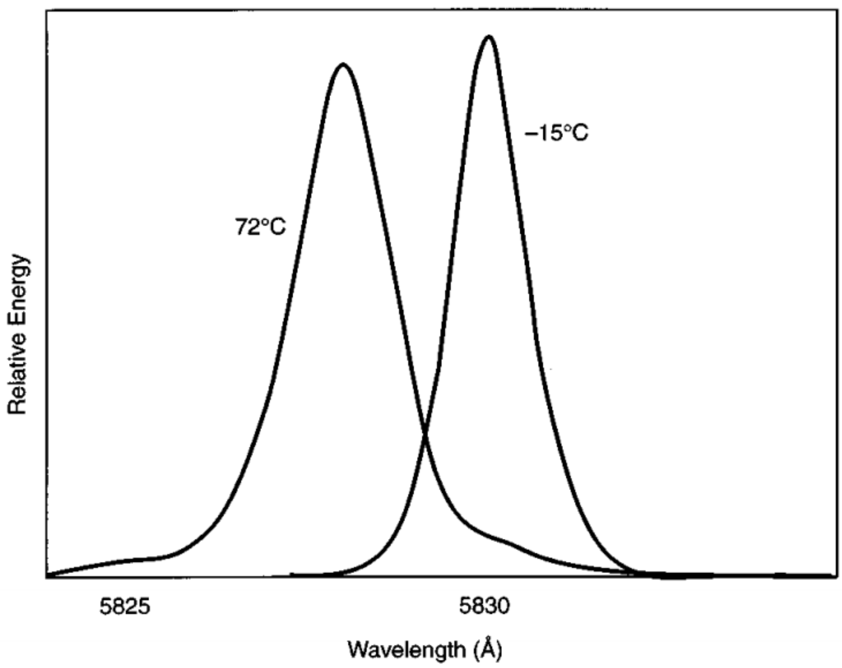

Figure 2.6: *Line position and line width of Y_2O_2S:Eu(III) at different temperatures* ***[2]***.

Each emission line also has a finite width, which is often designated as the full width at half maximum (FWHM) which usually decreases with a decrease in temperature. This is due to the lattice thermal agitation that reduces with a decrease in temperature and causes the sharpening in the emission lines, as illustrated in Figure 2.6. Line shift and line width changes as a function of temperature are usually small and therefore not often used in fluorescence thermometry as compared to the intensity and lifetime techniques [2].

Absorption and excitation band shift technique

Absorption of excitation energy is usually studied by measuring the amount of light transmitted or reflected from a material as a function of wavelength. However, absorption features can also be studied by measuring the emission intensity at certain wavelengths, as a function of excitation wavelength. Most phosphors have a broad band absorption in the ultraviolet to blue side of the spectrum due to absorption of these wavelengths by the host lattice. Usually sharp absorption features in the visible to near infrared range are also present which can be due to atomic transitions in the dopant ion. These sharp features can be temperature dependent, but the broad ultraviolet absorption band usually show a more remarkable temperature dependence, as shown in Figure 2.7. This change in the absorption as a function of temperature can be due to the change in the position of the charge transfer band that can be affected by temperature [2]. Therefore optical thermometry can be employed by measurning these absorption features of certain materials.

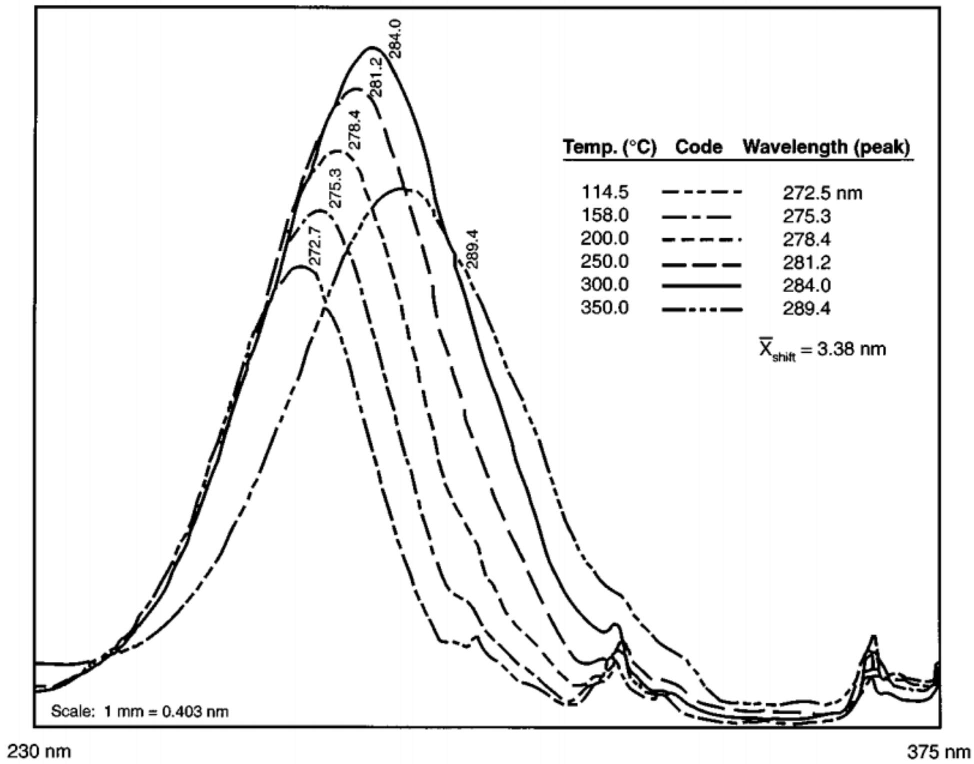

Figure 2.7: *Excitation spectra as a function of temperature of Y_2O_3:Eu(III)* ***[2].***

2.1.7 Applications

The measurement of temperature plays an important role in experimental science, engineering and medicine. Because of the accelerating nature of technology in these areas there is an increasing demand for knowledge about the temperature of components, systems or specimens. Phosphor thermometry is especially useful for the remote measurement of temperatures of moving surfaces, where conventional temperature sensing techniques such as thermocouples and thermistors fail. This is achieved by coating the surface of interest with an appropriate phosphor material, exciting the surface with a light source and optically measuring one or multiple of the optical properties as mentioned in the previous section. By using this measurement data and comparing it to pre-calibrated data, the temperature of the surface in question is determined. The range of temperatures that the combination of these types of phosphor materials are capable of measuring, is currently from cryogenic temperatures to about 2000 °C. These materials also could provide high sensitivity of about 0.05 °C and stability in harsh environments [2].

2.2 Lanthanum oxysulphide doped with europium(III)

Literature indicate that La_2O_2S:Eu(III) powder material is a well-tested thermographic phosphor [2] [3] [4]. Under ultraviolet excitation this phosphor fluoresces brightly in the visible range. The absorption by the host material is broadband while its emission of the Eu(III) ion consist of several sharp lines which is characteristic of the rare-earth dopants. This emission is proven to be temperature dependent due to mainly the thermal quenching effect, as will be explained at the end of this section. This section is divided into three main parts. The first part solely discusses the optical, structural and chemical properties associated with the host material. The second part discusses the spectral characteristics associated with the activator ion while the last part discusses the thermographic properties of the phosphor material as a whole.

2.2.1 Lanthanum oxysulphide host material

Optical properties

La_2O_2S is known for its good light absorption efficiency and wide band gap between the conduction band (indicated with the blue block) and valence band (indicated with the red block) as shown in Figure 2.8. According to literature La_2O_2S has an indirect band gap because the conduction band´s minimum (indicated with the blue arrow) is shifted with respect to the valence band´s maximum (indicated with the red arrow). Note that the energies in Figure 2.8 are normalised with respect to the top of the valence band. A previous density functional theory study indicated that for a transition to be possible for this indirect band gap material, a phonon with a minimum energy of E_p=1.44 eV together with a photon with an energy of E_g=2.91 eV, is required [17]. The indirect optical band gap can be estimated from the absorption edge of the diffused reflectance spectra by using the widely used Tauc plot. The diffused reflectance spectra is obtained by the process explained in the Experimental Techniques and Methodology chapter. The Tauc plot for indirect transitions is done by using Equation 2.23, which is derived from Equation 2.5 by removing the terms associated with the phonon energy E_p.

$$(h\nu F(R))^{1/2} = A(h\nu - E_g) \qquad \textbf{2.21}$$

$F(R)$ is the Kubelka-Munk function which is proportional to the absorption coefficient which is obtained from the diffused reflectance spectrum [18]. The diffused reflectance R is related to the Kubelka-Munk function by the following relation.

$$F(R) = \frac{(1-R)^2}{2R} \qquad \textbf{\textit{2.22}}$$

By plotting $(h\nu F(R))^{1/2}$ against $h\nu$ and drawing the tangent line to the point of inflection of the linear part of the resulting curve, the value of the optical band gap is estimated. As seen in Figure 2.8, the valance band consists of 9 bands that are located between -3.5 and 0 eV. These bands have O 2p character with mixing of the La 5d and S p3 orbitals. The conduction band however consists of several different bands at different energy levels, however Figure 2.8 only shows a small portion of these bands. The lowest energy band has mainly La 4f and La 5d character and is located between 4 to 5.5 eV. Located at 5.5 to 13.5 eV is the conduction bands resulting from La 5d with some mixing form the S 3d and O 2p orbitals [17].

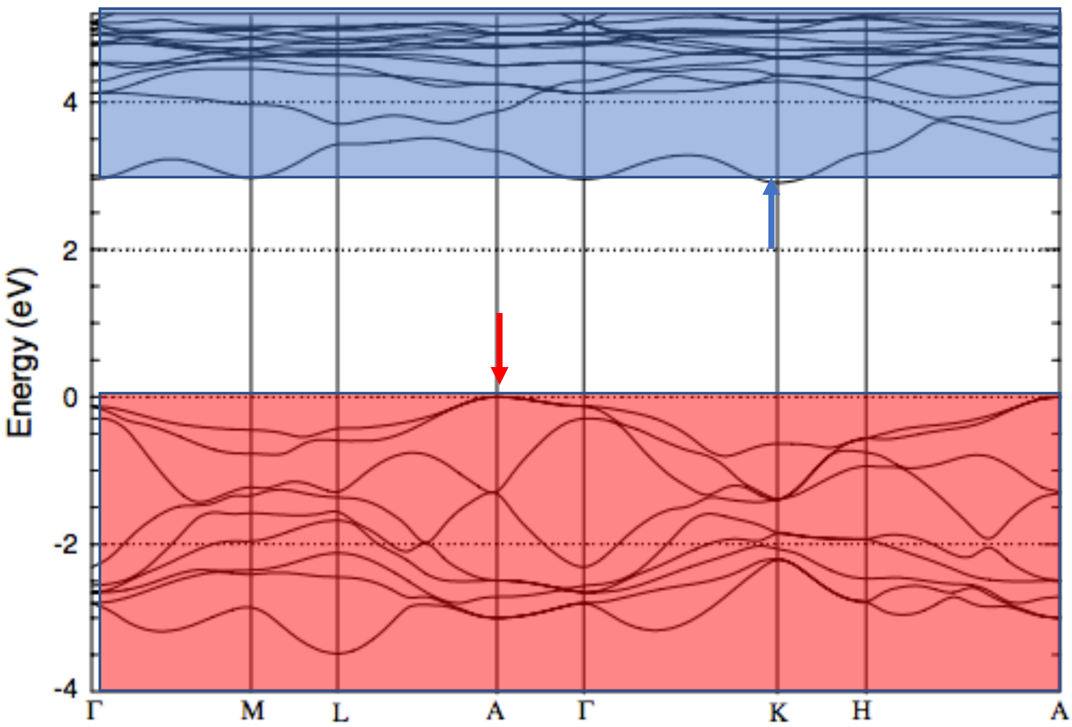

Figure 2.8: *Band structure of La_2O_2S* ***[17]***.

Structural properties

The structure of La_2O_2S is closely related to the structure of lanthanum oxide (La_2O_3). However, the structure of La_2O_2S differs from the structure of La_2O_3 in the fact that a sulphur(II) (S(II)) ion occupies one of the three possible O(II) sites. The crystal structure of La_2O_2S is shown in Figure 2.9 (a). As shown in Figure 2.9 (b) it adopts a trigonal structure that consist of a La_2O_2 parallelogram basic plane. In Figure 2.9 (c) the periodic stacking of the La_2O_2 basic layer can be seen. These layers are separated by hexagonal structure S(II) atomic layers.

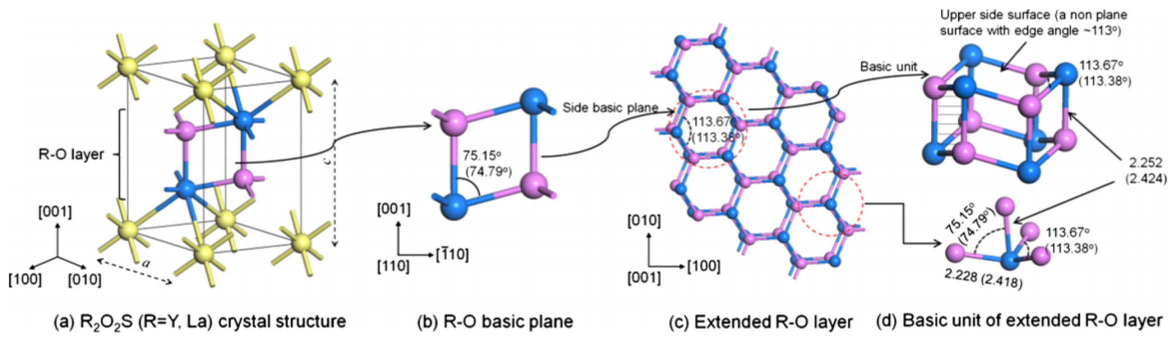

Figure 2.9: *Schematic diagrams of La_2O_2S crystal structure (Blue – La(III), Pink – O(II) and Yellow – S(II)). Bond angles and lengths outside parenthesis are for Y_2O_2S while the values inside parenthesis are those of La_2O_2S* ***[19]***.

As shown in Figure 2.9 (d) the La_2O_2 basic layer form a distorted hexagonal prism. It can also be seen that this layer is formed by tetrahedral structures where La(III) ions are coordinated to one axial and three equatorial O(II) ions. Literature suggests that the two positions of the La(III) ions are equivalent as seen in Figure 2.9 (a) [19]. The average theoretical calculated distance between the different atoms in this structure is shown in Table 2.1.

Table 2.1: *Distances between atoms in La_2O_2S* ***[17] [19]***.

Bonds	**Distance (Å)**
La(III) - O(II)	2.42
La(III) - S(II)	2.99
O(II) - S(II)	3.42

Although the structure of La_2O_2S is a distorted hexagonal prism (γ=113.38°, α=75.15°), the lattice parameters a and c (labelled in Figure 2.9 (a)) can be estimated by use of Equation 2.23 for hexagonal crystal structures (γ=120°, α=90°).

$$\frac{1}{{d_{hkl}}^2} = \frac{4}{3}\left(\frac{h^2 + hk + k^2}{a^2}\right) + \frac{l^2}{c^2} \qquad \textbf{\textit{2.23}}$$

In this equation d_{hkl} represents the inter-planar distance of lattice planes and is obtained by experimental techniques as explained in the Experimental Techniques and Methodology chapter, whilst h, k and l are the Miller indexes for the corresponding Bragg plane. The standard values for the lattice parameters of La_2O_2S is a = 4.05 Å and c = 6.94 Å.

Chemical properties

La_2O_2S is known to react spontaneously with water vapour in the atmosphere at room temperature that causes the formation of lanthanum hydroxide ($La(OH)_3$) on the surface of the material [20]. To totally remove these hydroxide groups the powder can be annealed while in a nitrogen atmosphere to ensure dehydration of the material. However, to successfully analyse and quantify these La_2O_2S samples a thermo-chemical reaction chamber attached to XPS instrumentation is required, in which the samples can transferred without exposure to atmosphere [21]. When La compounds are studied with the XPS technique the La photoelectron core electron spectrum is deconvoluted into three main peaks as shown in Figure 2.10. One of these peaks corresponds with the photoemission of the final state without charge transfer to the La 4f orbital and is usually denoted as $\underline{c}4f^0$, where $\underline{c}$ represents the presence of a core hole and $4f^0$ the absence of electrons in the 4f orbital [21]. The other two peaks present correlate with the bonding and antibonding component of the final state with charge transfer from the ligand valence band to the La 4f orbital. These peaks are usually denoted as $\underline{c}4f^1\underline{L}$ to indicate the transfer of an electron from a ligand atom to the 4f orbital of the La(III) ion. To reduce the amount of peak fitting variables, the multiplet splitting and the hybridisation of both final states is disregarded [21]. Only studies involving $La(OH)_3$ and La_2O_3 could be found with reliable data as shown in Table 2.2. However, the assumption was made that the La(III) ion in La_2O_3 has a similar chemical environment than the La(III) ion in La_2O_2S due to the electronegativity of O(II) and S(II) being similar [22].

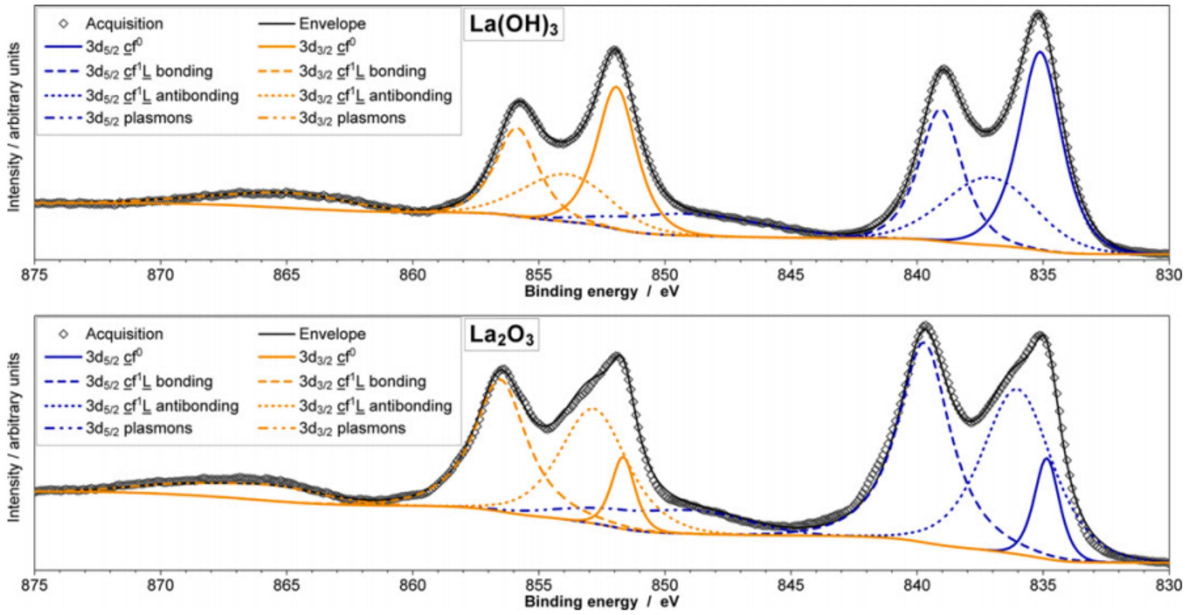

Figure 2.10: *La 3d region for La(OH)$_3$ and La$_2$O$_3$ with peak fitting components* ***[21]****.*

Table 2.2: *Peak positions and relative intensities of different components of the La 3d$_{5/2}$ peak* ***[21]****.*

Component	**La(OH)$_3$**		**La$_2$O$_3$**	
	Peak Position (eV)	**Atomic percent (%)**	**Peak Position (eV)**	**Atomic percent (%)**
La 3d$_{5/2}$ c4f^0	835.1	43	834.9	10
La 3d$_{5/2}$ c4f^{1}L antibonding	836.6	57	835.3	90
La 3d$_{5/2}$ c4f^{1}L bonding	838.6		839	

When comparing the positions and intensities of the different components of the deconvoluted La 3d$_{5/2}$ peak of La(OH)$_3$ and La$_2$O$_3$ compounds, it can be seen that the peak separation between the bonding and antibonding satellites and the relative intensity of the satellites to the main peak increase from the hydroxide to the oxide compound. This is attributed to a smaller separation in energy and stronger hybridisation, between the valence band and the 4f^1 orbital of the final state of La$_2$O$_3$ compared to La(OH)$_3$.

When studied with the XPS technique the observed O 1s photoelectron peak can have more than one component. This is due to the O(II) ions that are bonded to different atoms, including that of contaminants. Literature also show that O(II) defects are energetically favourable over a broad range of environmental conditions. Table 2.3 shows the chemical bond and different peak positions that is generally used for deconvolution of the O 1s photoelectron peak of the La_2O_3 host material [21].

Table 2.3: *General peak positions of different components of the O 1s peak* ***[22]***.

Chemical Bonds	**Peak Position (eV)**
La_2O_3	530.0
Defects O(II)/ Hydroxide	531.4
CO_2/ CO_3/ Chemisorbed CO_2	532.4
H_2O	533.2
Physisorbed CO_2	534.5

Literature indicates that the main peak position of the O 1s peak is 531.4 eV for $La(OH)_3$ and 530.5 eV for La_2O_3. The reason for difference in peak position is attributed to the O(II) in $La(OH)_3$ and La_2O_3 occupying two different positions in the crystal structure of the compound. The O(II) in $La(OH)_3$ has six-coordinated atoms which causes a higher photoelectron binding energy than that of the O(II) with four-coordinated atoms in La_2O_3 [21]. Precise comparison between various XPS studies is difficult because of differences in x-ray radiation, spectral analyser settings, charge correction and data deconvolution. These factors can cause differences in the observed results that are not related to the material. Therefore, it is important the acquisitioned spectra be deconvoluted with peak fitting components where some variables are controlled by constraints. For this study, there was mainly focussed on the relative changes in the spectra, as explained in the Results and Discussion chapter.

2.2.2 Europium(III) activator ion

The trivalent Eu(III) activator ion has an intense luminescence in the red spectral region when excited with ultraviolet irradiation. This is observed for both Eu(III) ions doped in crystalline host matrices and Eu(III) complexes with ligands. Luminescence in this ion´s complexes can be achieved by photo-, cathode-, chemi-, electroluminescence, etc. [23]. Transitions from the ground state directly to the lower excited state of the activator ion are optically forbidden, therefore when under excitation the matrices and ligands absorb the excitation energy and subsequently transfer the energy to the higher energy levels of the activator ion from where the excited levels are populated [15]. Eu(III) ions have narrow transitions that cause sharp emission peaks in the luminescence spectra which is a characteristic of this rare-earth dopant. The local environment of this ion, like the point group symmetry, can be probed by studying the fine structure and relative intensities of the transitions in the luminescence spectra [23]. The Eu(III) ion has 60 electrons, 54 of which are in a shell like the Xenon atom and 6 of which are in the 4f shell, which is shielded from the environment by the closed $5s^2$ and $5p^6$ outer shells. These 6 electrons in the 4f shell can be arranged in 3003 ways in the seven 4f orbitals, therefore the total degeneracy of the Eu(III) ion´s electronic configuration is 3003, as calculated by Equation 2.24:

$$\binom{14}{n} = \frac{14!}{n!\,(14-n)!} \qquad \textbf{\textit{2.24}}$$

where n is the number of electrons in the 4f shell. Each electronic arrangement that is unique is called a microstate. The degeneracy of the $4f^6$ configuration is lifted by several perturbations that acts on the Eu(III) ion as shown in Figure 2.11. These include electron repulsion, spin-orbit coupling, crystal-field perturbation and the Zeeman effect. Electron repulsion occurs due to the electrostatic interaction between the electrons in the 4f shell and is denoted as “terms” in Figure 2.11. The spin-orbit coupling occurs due to the interaction between the magnetic fields that results from the spin magnetic field moment of the electrons and the magnetic field that is created by the movement of the electrons around the nucleus and is denoted as “levels” in Figure 2.11. The crystal-field effect is due to the interaction between the electrons of the host material and the 4f electrons of the activator ion and is denoted as sublevels in Figure 2.11. Lastly the Zeeman effect is observed only in the presence of an external magnetic field that causes further splitting of the energy levels and is not indicated in Figure 2.11 [23].

Information about the transitions between the different levels is obtained by studying the emission spectra of Eu(III) compounds. Emission spectra are obtained by fixing the wavelength of the excitation source while scanning the detection wavelength of the spectrometer as explained in detail in the Experimental Techniques and Methodology chapter. Most of the intense photoluminescence observed in Eu(III) compounds are from the transitions from the $^5D_0$ excited state to one of the sublevels of the ^7F_j ground states [23]. Transitions from the higher excited states, like the $^5D_1$, $^5D_2$ and $^5D_3$ states, are not that common. However, in some Eu(III) complexes, especially those with an inorganic host lattice, emission can originate also from the $^5D_1$, $^5D_2$ and $^5D_3$ excited levels. The emission spectra of Eu(III) compounds, tend to be complex due to the number of transitions that occur to different states. Discrimination between the emission from higher excited states and the $^5D_0$ state is however possible using decay time luminescence measurements. This is due to the fact that the decay time of the emission from the higher excited states are much shorter than that of the lower $^5D_0$ state [23].

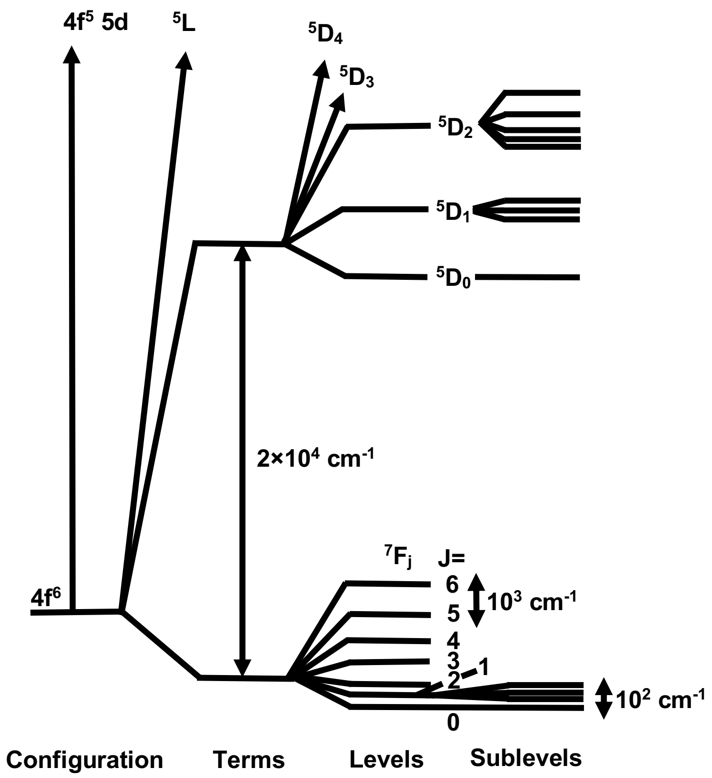

Figure 2.11: *Partial energy diagram of the Eu(III) ion.*

2.2.3 Thermographic properties

As mentioned before La_2O_2S:Eu(III) is a good and well-tested thermographic phosphor. The main reason for this is because of its luminescence properties that change undistortedly with temperature. This is due to the fact that emission of photons occurs through electronic transitions within the 4f shell that is partially filled and is contained within the outermost 5s and 5d shells [23]. This outermost shell is important because it shields the emitting 4f shell from most of the effects of the La_2O_2S host material that tend to influence the emission. However, there still exist some interactions between the La_2O_2S host and the states of the Eu(III) activator ion, which render this phosphor´s emission to be temperature-sensitive [23]. The coordinate model is shown in Figure 2.12 for the ground state (^7F_J (J=0, 1, 2, 3, 4, 5, 6)) and some of the excited states (^5D_J (J=0, 1, 2)) of the 4f levels of the Eu(III) ion. Also present in Figure 2.12 is the charge transfer states originating from the S(II) – Eu(III) and O(II) – Eu(III) bonds. The presence of the charge transfer states in the coordinate model of Eu(III) is due to the radius of Eu(III) ion being smaller than the radius of the La(III) ion it replaces. As seen in the structure of the host material shown in Figure 2.9, the La(III) ion is bonded to seven atoms, therefore the coordination number is of La(III) ion is VII. According to literature the La(III) VII ion has an effective ionic radius of 1.10 Å while the Eu(III) VII ion has a smaller effective ionic radius of 1.01 Å [24].

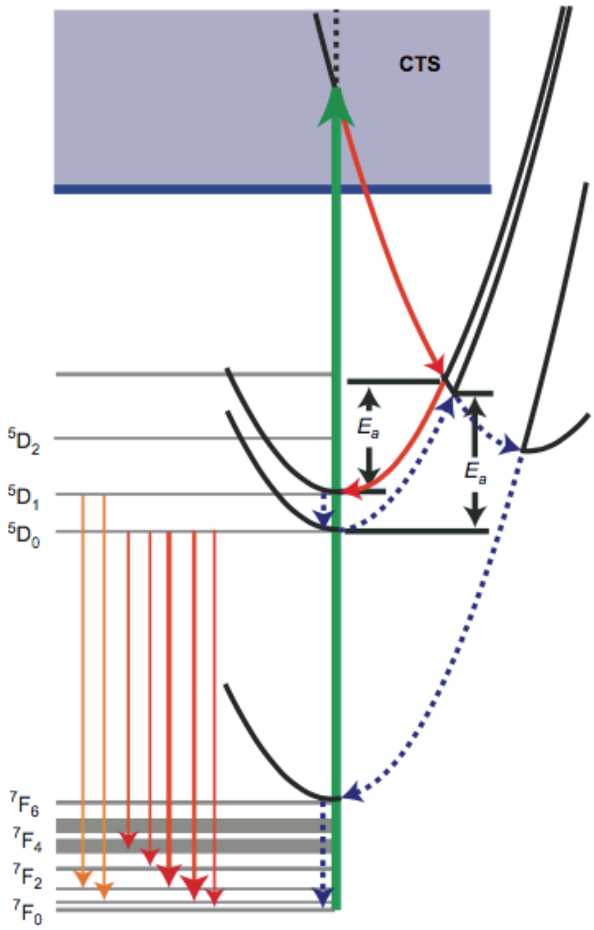

Figure 2.12: *Coordinate model for the thermal quenching of La_2O_2S:Eu(III)* ***[59].***

Due to the presence of the charge transfer state, there is another pathway for the electrons in the excited states to move to the ground state. However, for this to be possible these electrons need to be aided by thermal energy to achieve the required activation energy E_a to cross the intersection point between the excited state´s and charge transfer state´s potential curves. Once the electrons reach this point they move to the ground state by releasing their energy non-radiatively through the dissipation of heat through the lattice. This process is referred to as thermal quenching and the change in the observed luminescence efficiency is described by Equation 2.20. However, to measure this effect the intensity of the emission must be related to the efficiency by utilising Equation 2.18 as shown by the following relation.

$$\eta = \frac{I_m}{I_m + (I_0 - I_m)} \qquad \textbf{\textit{2.25}}$$

In Equation 2.25, $\mathrm{I_m}$ represents the emission intensity measured for a transition at a given temperature and $\mathrm{I_0}$ represents the initial emission intensity at the onset of thermal quenching for that specific transition. By substituting Equation 2.25 in Equation 2.20 the emission intensity as a function of temperature is represented by Equation 2.26 [3].

$$I_m = \frac{I_0}{1 + G\exp\left(\frac{-E_a}{kT}\right)} \qquad \textbf{\textit{2.26}}$$

In this equation G is a pre-exponential constant that is related to the frequency at which these cross-over events occur. Equation 2.20 indicates that G is the ratio between the frequency factor and the non-radiative transition probability. Equation 2.26 and be rewritten as follows.

$$\ln\left(\frac{I_0}{I_m} - 1\right) = -\frac{E_a}{kT} + \ln(G) \qquad \textbf{\textit{2.27}}$$

It is clear from Figure 2.12 that the required activation energy decreases the higher the excited states. The activation energy for excited state and pre-exponential constant determined for the La_2O_2S:Eu(III) phosphor material in a previous study, is shown in Table 2.4. These values together with Equitation 2.26 could be used to obtain a graphical representation of the expected relative emission intensity as a function of temperature for the different excited states as shown in Figure 2.13.

Table 2.4: *Activation energy, pre-exponential constant and thermal quenching onset temperature measured in a previous study **[3]**.*

J	E_j (eV)	G (s^{-1})	T_{onset} (°C)
0	0.78	3.2×10^7	175
1	0.62	3.2×10^7	83
2	0.37	3.2×10^7	-60
3	0.14	3.2×10^7	-188

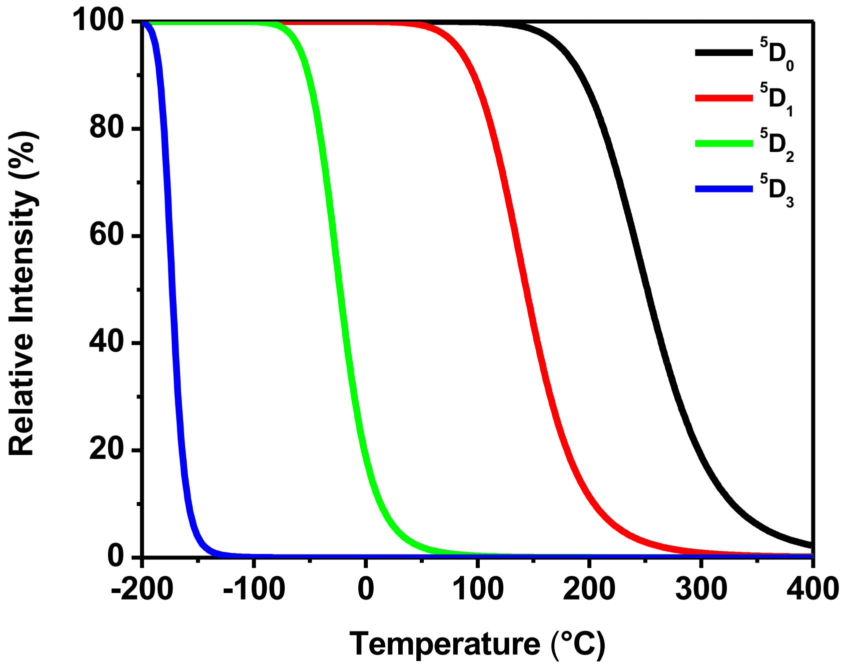

Figure 2.13: *Graphical representation of the relative emission intensity of La_2O_2S:Eu(III).*

As expected the emission from the different states decreases sequentially with an increase in temperature, if thermal quenching is the dominant mechanism at work. For the different individual states the thermal quenching effect is small at low temperatures and the emission stay constant until the exponential term of Equation 2.26 increases sufficiently. When the Boltzmann relation prevails for each state, the number of Eu(III) ions of which electrons can reach the intersection point increases exponentially with an increase in temperature. The temperature T_{onset} at which the emission individual excited state decreases to 95% of its initial intensity is generally considered as the onset temperature for thermal quenching and therefore the emission of the ^5D_j states is only considered temperature sensitive while the following relation is true.

$$T_{onset} > -\frac{E_a}{k \ln\left(\frac{0.053}{G}\right)} \qquad \textbf{2.28}$$

By using the activation energy and pre-exponential constants determined for La_2O_2S:Eu(III) in a previous study together with Equation 2.28 the onset temperature was calculated for each excited state as shown in Table 2.4. From this it is observed that the higher excited states become temperature dependent at a lower temperature, while the lower excited states become temperature sensitive at higher temperatures. Therefore, by using the FIR technique, the changing emission intensity from one of the higher temperature sensitive states can serve as a possible temperature indicator, while the emission from one of the lower temperature insensitive states can serve as an emission intensity reference.

3. Experimental Techniques and Methodology

In this study the optical, structural and chemical properties of commercially available La_2O_2S:Eu(III) (SKL63/F-R1) phosphor material were researched. This material is produced by Phosphor Technology Ltd. To obtain a better understanding of the absorption mechanism of the phosphor the band gap and charge transfer bands were studied by utilising the Perkin Elmer Lambda 950 UV-VIS spectrometer and the Varian Cary Eclipse fluorescence spectrophotometer. The different electron transitions were also identified by the measurement of the luminescence lifetime, by utilising the Varian Cary Eclipse fluorescence spectrophotometer. The PL system in the Physics Department at the University of the Free State was modified to allow the measurement of the emission spectra of phosphor materials at different temperatures. This system was then used to study the emission of the La_2O_2S:Eu(III) phosphor material from 510 to 720 nm in the temperature range from 30 °C to 330 °C. The luminescent stability of this material was also tested by utilising this modified PL system, which was done by measuring the emission intensity of the different transitions every 30 min for a time period of 480 min while the material was kept at a constant temperature of 400 °C.

The structural and chemical stability of the La_2O_2S:Eu(III) phosphor material were also tested by utilising the XRD, XPS and luminescence lifetime techniques. These tests were done by annealing the phosphor material to 400 °C for 0, 30, 60, 120 and 240 min by using the custom-built temperature controller unit. Afterwards the change of the structure, strain and crystallite sizes of these different samples were determined by using the XRD technique. The change in the chemical state of the La(III) ions was determined and the relative amount of defect O(II) for the different samples were determined by utilising the XPS and luminescence lifetime techniques. The various experimental parameters and procedures are given throughout this section while the working, enhancements, calibrations and programming of the different components are explained.

3.1 Photoluminescence spectroscopy

The PL system in the Physics Department at the University of the Free State, capable of only measuring fluorescence spectra of phosphor materials at room temperature, was modified to also be used at higher temperature measurements. Figure 3.1 shows a basic layout of the PL system before modifications. At the top left corner is the helium-cadmium laser. The laser beam is filtered with a filter to produce a 325 nm laser beam that is used as excitation source. The laser beam is pulsed with an optical chopper. The pulsed laser beam excites the phosphor material and the emitted light is focused towards a spectroscope by a convex lens. The spectroscope uses a diffraction grating to diffract the emitted light into several beams of different wavelengths traveling in different directions, which are reflected by a mirror as seen in Figure 3.1. Depending on the grating′s position a certain wavelength of light can enter the photomultiplier tube (PMT) for detection. This spectroscope and PMT system can measure spectra from 350 to 800 nm. The PMT converts the light intensity into an electrical signal which is supplied to a lock-in amplifier. The lock-in amplifier uses this signal together with the clock frequency from the chopper frequency control to implement phase-sensitive detection that reduces background noise. A computer program uses this low noise signal together with the grating position to obtain an emission spectrum.

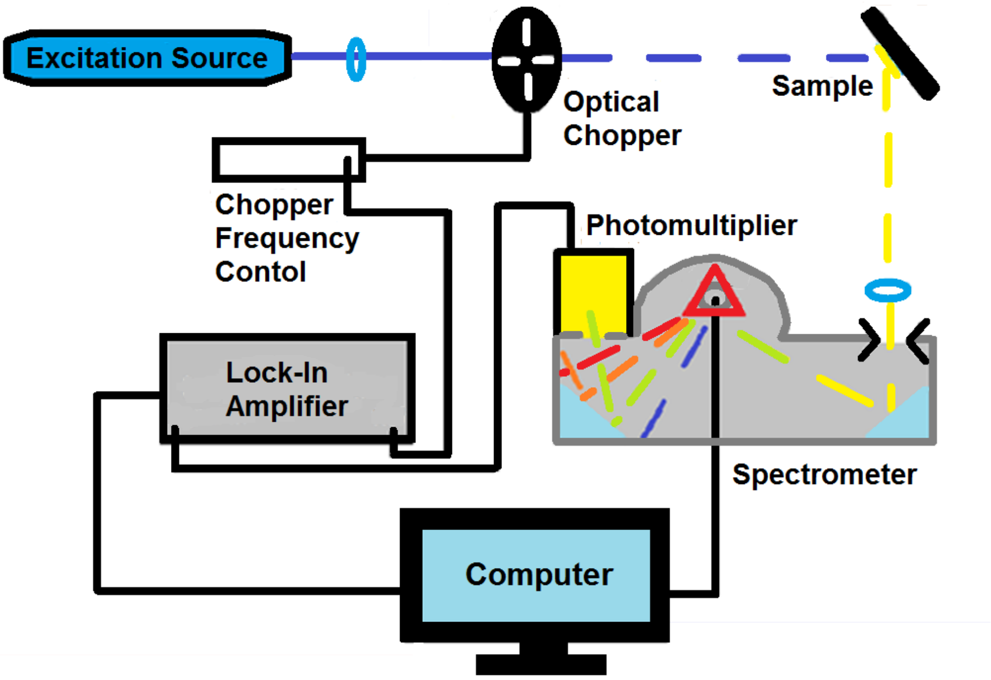

Figure 3.1: *Layout of PL system before modifications.*

To measure the emission spectra of phosphor materials at different temperatures modifications and enhancements were made to the PL system as shown in Figure 3.2. These modifications include the addition of a power meter to monitor the laser´s intensity and a temperature controller unit to measure and control the temperature of the phosphor material while measuring the emission spectra. For this study multiple apparatus were designed, developed, calibrated as well as a computer program written that allowed measurement and control over this system. The programming language that was chosen is Microsoft´s Visual Basic. The main user-interface is shown in Figure 3.3. This section focusses on the different components of this system and the modifications, calibrations and programming that were made.

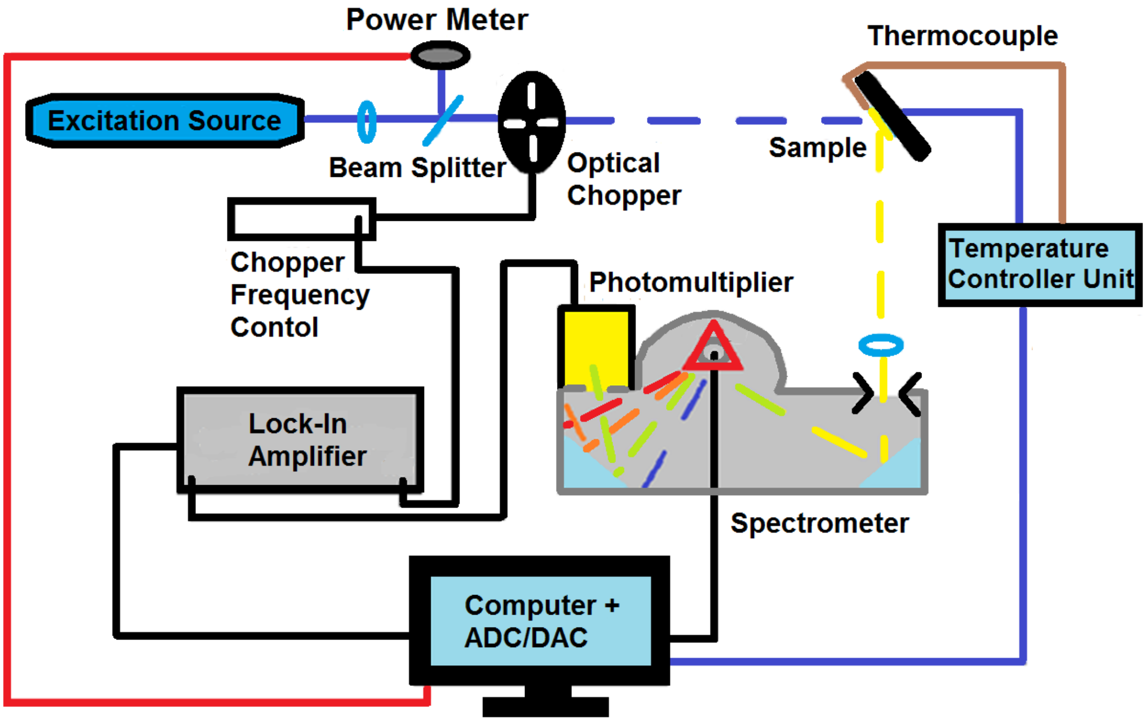

Figure 3.2: *Layout PL system after modifications.*

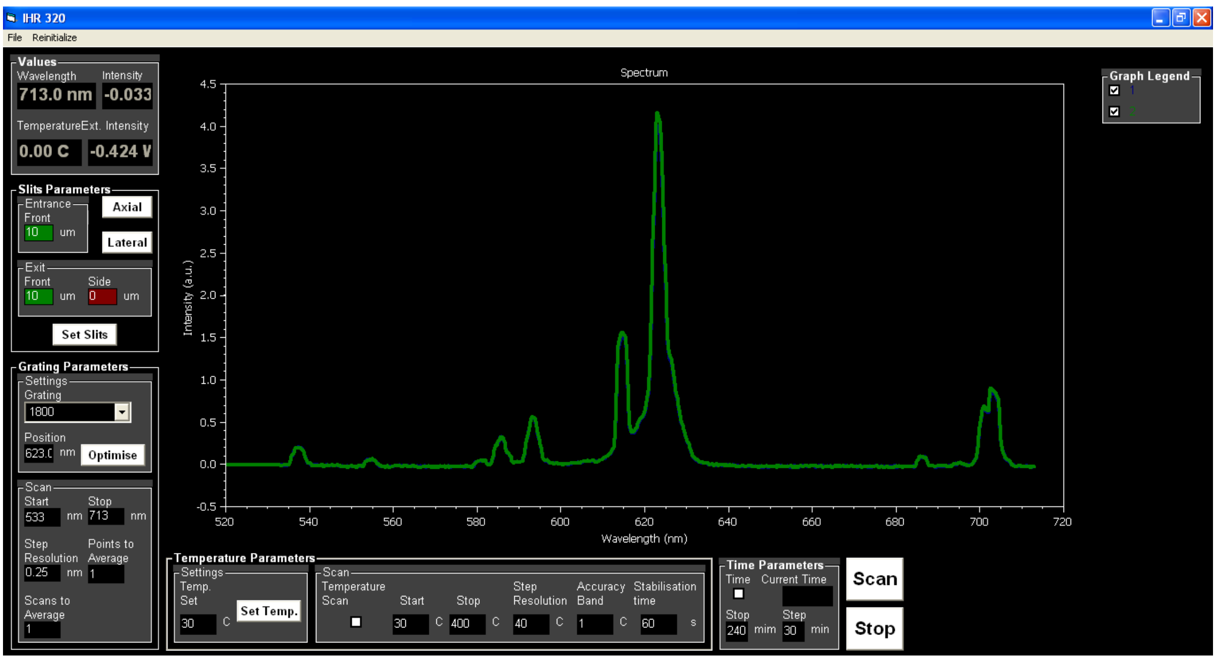

Figure 3.3: *Screen shot of main user interface.*

3.1.1 Excitation source

As stated in the Theory and Literature Review chapter, this dissertation focusses on the photoluminescence of phosphor materials. photoluminescence is the result of a process where emission is observed from a sample that is stimulated by electromagnetic radiation. In this system, the electromagnetic radiation is supplied by a helium-cadmium laser. The intensity of the laser beam can vary over time and therefore to monitor the excitation source´s intensity while emission spectra is acquisitioned, a reference detector was added and calibrated as explained in this section.

Hardware

The excitation source used in this system is a Kimmon KOHA CO., LTD. Helium-Cadmium Laser. This is a continuous wave high quality source for ultraviolet (325.0 nm) and violet (441.6 nm) radiation [25]. This type of laser is part of a class of gas lasers that uses helium in conjunction with a metal, in this case cadmium, to achieve lasing [26]. At room temperature, the cadmium is a solid and for lasing to be possible the metal is evaporated from a reservoir by a heated filament cathode that is carefully controlled to maintain the correct metal vapour pressure. This vapour is then distributed uniformly throughout the laser bore by the process of electrophoresis [25]. Helium is also added as needed to maintain the correct helium to cadmium pressure ratio. The helium is needed to sustain the electrical discharge and then to excite the cadmium vapour which release energy by emitting ultraviolet and violet radiation [26].

There are several conditions that can influence the stability of the laser and as a result the radiation output can vary over time. In an effort to ensure a constant radiation output, temperature and pressure sensors monitor the temperature and pressure parameters and feedback loops control the power sequencing logic to ultimately maintain a constant helium and cadmium pressure. However, in this laser there is no radiation monitor that can regulate the radiation output by varying the tube current [26]. Also, over longer time scales the radiation output of the laser can decrease due to a decrease in the amount of cadmium and/or helium [25].

This laser produces two main radiation emissions at 325 and 441.6 nm respectively, as shown in Appendix A [27]. To eliminate the 441.6 nm emission from the radiation output, a filter with high absorption at 440 nm and close to zero absorption between 320 and 340 nm was placed in front of the radiation opening [28]. This filter allows the 325 nm emission to pass through, which is used as excitation source. To implement phase-sensitive detection, a Stanford Research Systems Model SR 540 Optical Chopper is used to pulse the excitation source as shown in Figure 3.1 and Figure 3.2. The optical chopper produces an electrical clock signal that is equivalent to pulses of the excitation that is supplied to the lock-in amplifier. Throughout experimentation the optical chopper was set to pulse the excitation at a frequency of 120 Hz.

To measure and monitor the laser´s radiation output, a Coherent, FieldMaxII, SN: 0072K09R, Laser Power and Energy Meter with thermopile was used. This radiation meter system was used to determine the power of a selected wavelength of continuous ultraviolet radiation. The meter also provides an analog output of 0-5V that is proportional to the power reading displayed on the meter [29]. An Edmund Optics, Ultraviolet Plate Beam Splitter with a wavelength range of 250 to 450 nm was installed as shown in Figure 3.2 [30]. This allows one to monitor the radiation output of the laser power during experiments while providing excitation to the sample. Calibrations were needed for this setup as explained in the next section.

Calibrations

It was necessary to calibrate the analog voltage output of the Laser Power and Energy Meter to the power value displayed on the meter. This was done by connecting the analog output of the meter to an analog-to-digital converter and illuminating the thermophile with a Rofin, Model 6006, intensity variable light source. The resulting voltage measured by the analog-to-digital converter and power reading on the display, were recorded in 0.1 mW increments while the intensity of the light source was varied. This relationship is represented by a linear fit as shown in Figure 3.4 which function was incorporated into the programming to allow the recording of the power of the excitation source as a function of time.

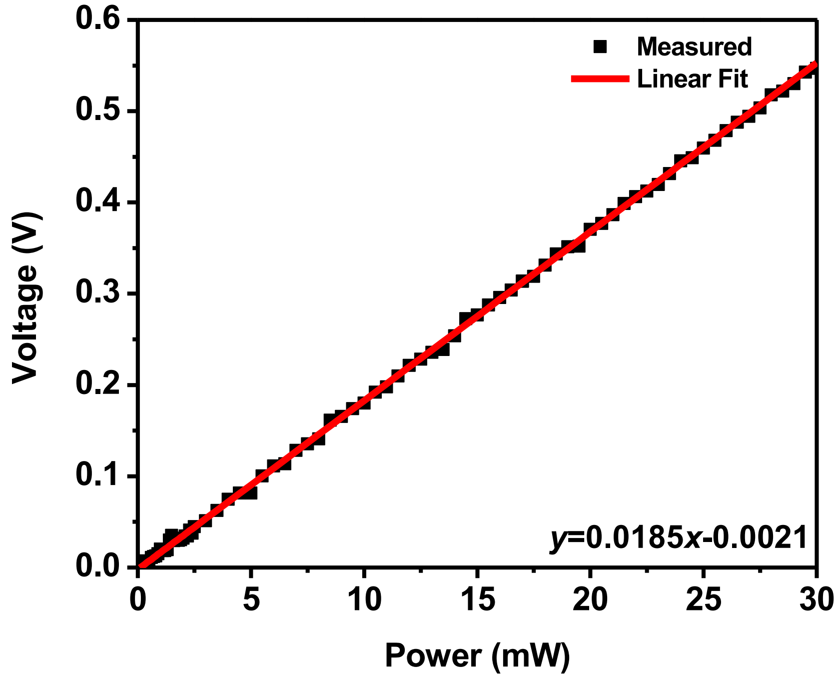

Figure 3.4: *Analog output calibrations of the simulated Laser Power.*

The calibrated power meter was used to determine the power of the different beams of the excitation setup as seen in Figure 3.5. The radiation output of the laser beam was measured as 29.8 mW. As shown in Appendix A the original radiation output was measured by the manufacturer to be 42.6 mW, which is an indication of a decrease in the cadmium and/or helium supply. It was also determined that the filter that eliminates the 441.6 nm emission reduces the beam power to 15.5 mW mainly due to absorption. The calibrated power meter was used to determine that the ultraviolet plate beam splitter reflected 86% and transmitted 13% of the 325 nm laser radiation as indicated in Figure 3.5. The 1% laser radiation that is unaccounted for is ascribed to the absorption from the material of the ultraviolet plate beam splitter.

By using an in-house programmed computer program the power of the laser was recorded over time from start-up. As illustrated in Figure 3.6 the laser´s power fluctuated at start-up and a stable beam was obtained at about 900 seconds after start-up. Experimental measurements were therefore only taken after waiting at least 15 minutes after start-up. However, the laser can also fluctuate after the start-up period as seen at 6000 seconds in Figure 3.6. It is therefore necessary to monitor the intensity throughout experimentation to justify the comparison of the intensity of different emission spectra and the different regions within the spectra.

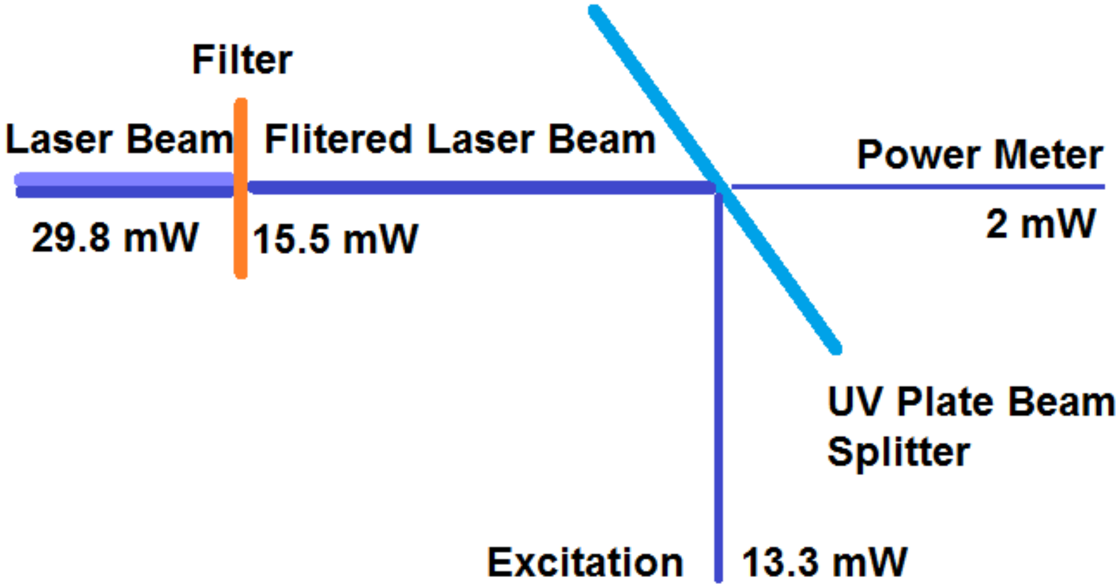

Figure 3.5: *Laser excitation path layout.*

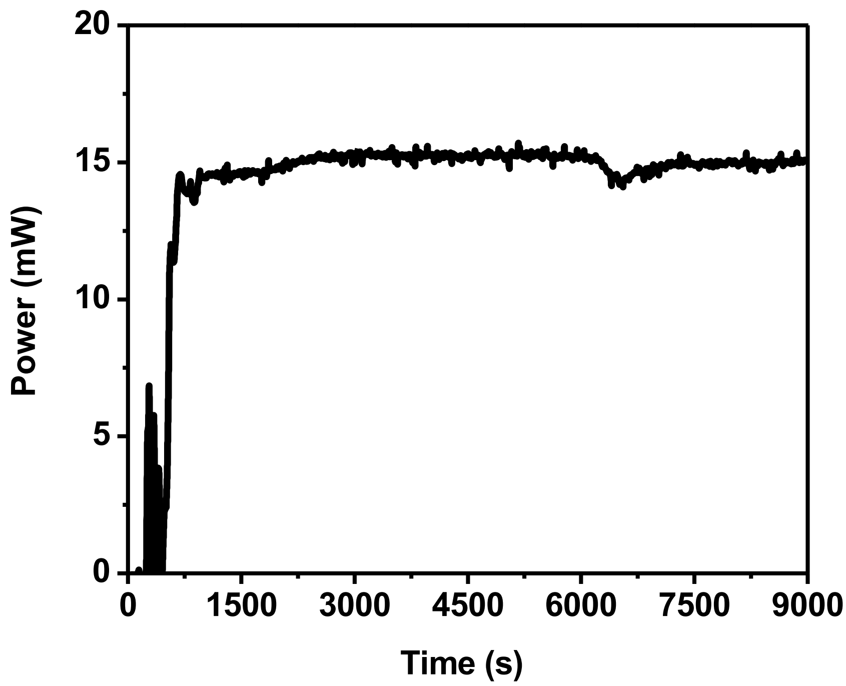

Figure 3.6: *Laser's intensity after start-up.*

Programming

The calibration and parameters obtained from Figure 3.4 and Figure 3.5 were used to calculate Equation 3.1. This equation was used in the programming to determine the $Power$ of the excitation by monitoring the $Voltage$ of the analog output of the power meter that was placed in front of the transmitted beam as seen in Figure 3.5. This allows the monitoring of fluctuations of the excitation source while emission spectra are obtained.

$$Power = Voltage \times 359\,mW/V + 0.76\,mW \qquad \textbf{3.1}$$

Figure 3.7 shows an example of a plot of the intensity of the laser as a function of the resulting emission spectra´s wavelength. From this it was calculated that the laser´s intensity has an average value of 14 mW and a standard deviation of 1 mW, during an emission spectrum scan. Figure 3.7 shows that this measurement system has a relative low signal-to-noise ratio compared to that of measuring the laser´s power directly as shown in Figure 3.6. This is understandable since only 13% of total excitation radiation is monitored in this setup.

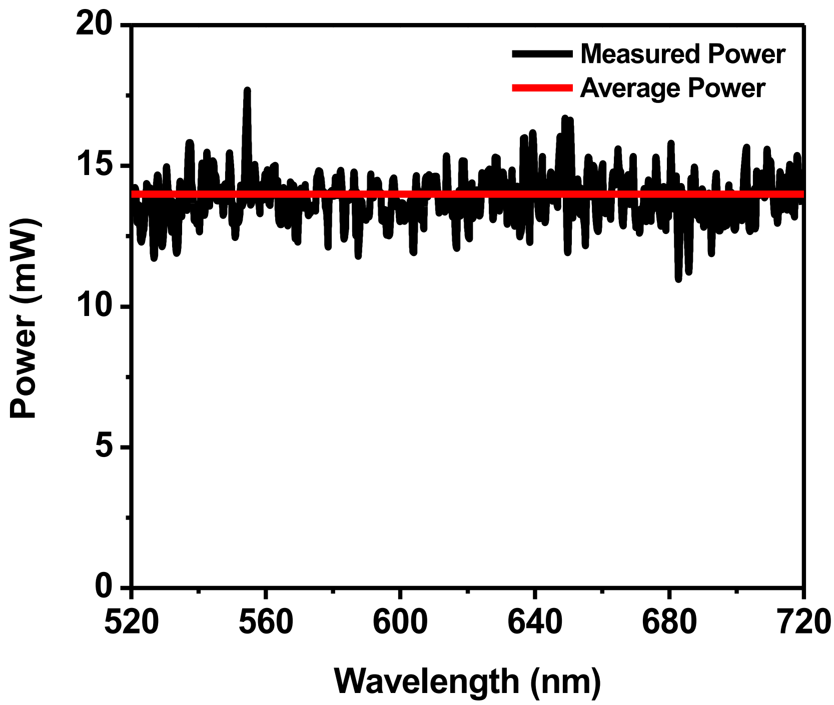

Figure 3.7: *Laser power fluctuations during measurements.*

3.1.2 Spectroscope

In this system, a spectrometer is used to transmit a selectable narrow band of wavelengths of light from a wider range of wavelengths from the sample, to the detector for analysis. This is achieved by use of a series of slits, mirrors and a diffraction grating as seen in Figure 3.8. The diffraction grating disperses multi-wavelength light into its constituent wavelengths, by reflecting each wavelength at a different angle. Dispersion of incident light occurs due to the periodic structure of the grating that causes wave front division and interference to occur. By analysing the intensity of the dispersed light at different angles to the diffraction grating, a wavelength spectrum is obtained [31]. Full control of the spectroscope used in this study was achieved by the development of custom-made acquisition software as discussed in this section.

Hardware

The Horiba Jobin Yvon iHR320 Fully Automated Imaging Spectrometer (SN: 0531-2509) is a triple grating spectrometer with a 320 mm focal length and entrance aperture ratio of f/4.1 [32]. Figure 3.8 shows a detailed schematic of the light path and internal construction of this spectrometer. The radiation emitted from the sample material enters at the manually controlled front entrance shutter. The light then passes through a computer controlled front entrance slit which width is controlled as explained in the next programming section. The slit height was kept fixed throughout measurements. The light is then reflected from the Collimating Mirror towards a Diffraction Grating Turret.

In the turret two diffraction gratings, one with 1800 lines per mm (SN: 441180) and the other with 950 lines per mm (SN: 441181), are placed and are selected by using the computer program. In this study, only the 1800 lines per mm was used, because it has a high relative efficiency in the visible region as seen in Appendix A. The relative efficiency of the 1800 lines per mm diffraction grating as a percentage, changes as a function of wavelength for unpolarised light. The dispersed light is reflected from the diffraction grating towards the focusing mirror, which in return reflects the spectral light towards the computer controlled front exit slit and manually controlled front exit shutter and finally enters the detector for detection.

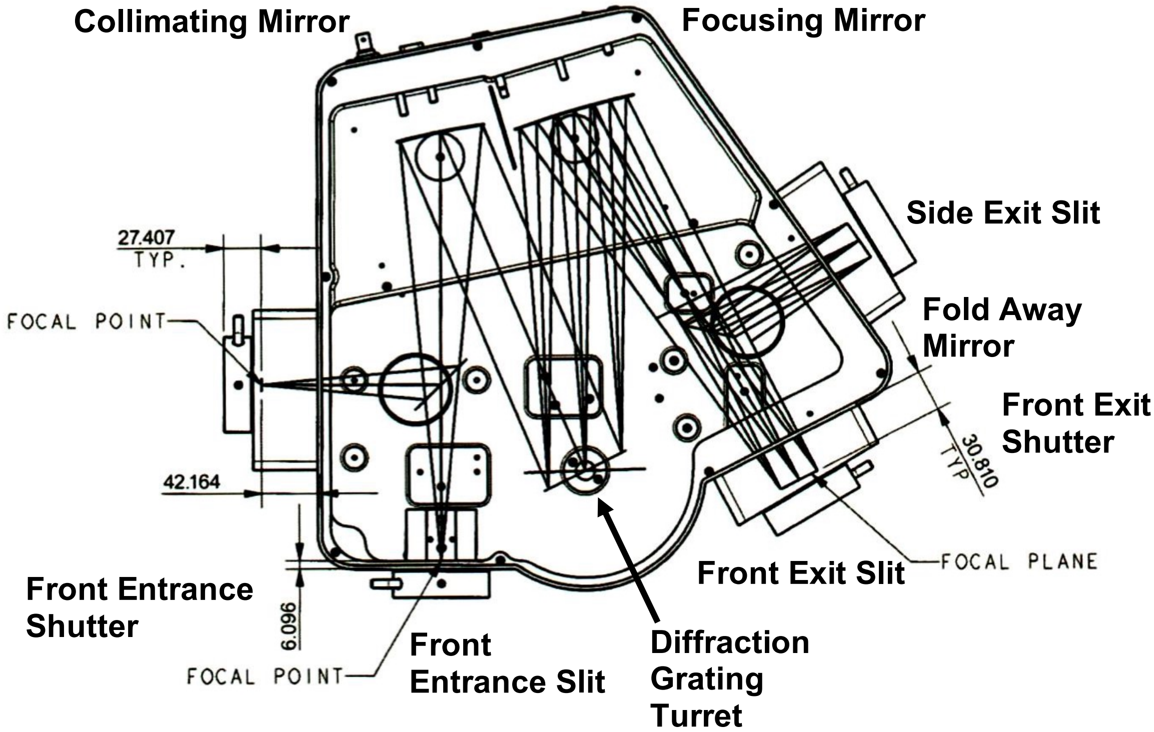

Figure 3.8: *Schematic of Horiba iHR320 spectrometer **[32]**.*

As shown in Figure 3.8, the turret rotates around the z-axis by use of a high precision stepper drive that is computer controlled. As the turret turns, different spectral components with different wavelengths of the emitted light is reflected into the PMT detector for detection. The light in its different spectral components can also be reflected, by the use of a computer-controlled fold away mirror through the side exit slit, towards an infrared detector. $Spectral\ Band\ Pass$ is a quantity that describes the wavelength ranges that is analysed and is indirectly proportional to spectral resolution. $Linear\ Dispersion$ is defined as the extent to which the spectra interval is spread out across the spectrometer´s focal field. For Entrance and Exit $Slits\ Width$ above 50 µm the spectral band pass is described by Equation 3.2.

$$Spectral\ Band\ Pass = Linear\ Dispersion \times\ Slits\ Width \qquad \textbf{3.2}$$

From Equation 3.2, it is important to understand that the spectral resolution is indirectly proportional to the $Slits\ Width$, while the light throughput is directly proportional to the $Slits\ Width$ [33]. Therefore, in order to maximize the spectral resolution and to increase the number of photons from the sample that reach the entrance slit, a convex lens is placed between the sample and the front entrance of the spectroscope which converges the light from the sample. This lens is mounted on a lens holder that has three degrees of freedom (x-, y- and z-axis) which allows for the optimisation of the light signal.

Programming

To allow communication between a computer the spectroscope the Horiba Jobin Yvon iHR320 provides a Universal Serial Bus interface that is controllable with the HORIBA Jobin Yvon´s Spectrometer Utilities program, SynerJY® data acquisition software. However, for this project there was decided to develop custom-made acquisition software to allow full control of all the installed slits and the diffraction grating turret. Full control of the system was established by the use of the SynerJY® Software Development Kit from HORIBA Jobin Yvon. This kit includes the basic functions to communicate and request information, to and from the spectroscope. To allow initialisation of the spectroscope the backend of the example program "Monochromator" was used. The complete code is included on the supplied compact disc. The programming logic that was used to control the different components of the spectroscope, is discussed in this section.

Set Slits Width, Adjust Grating and Adjust Fold Away Mirror

Figure 3.9 shows the user interface that was designed to set and display the width of the different slits of the spectroscope. The slits widths can be adjusted from 0 to 2300 µm in 2 µm increments. The flow diagram shows the logic of the algorithm used to safely adjust the slit width for the slits of the front entrance, side exit and front exit. This same algorithm logic was also used to change position of the grating in the process of requesting a wavelength or obtaining a spectrum. The complete code for these procedures is given in Appendix B. Figure 3.9 shows buttons named Axial and Lateral which is used to adjust the position of the fold away mirror. By selecting the Axial, the mirror is folded away, and the light is directed to the front exit and by selecting Lateral the mirror is folded in place to reflect the light to the side exit. In the experiment to follow the Axial option was chosen because the PMT detector is situated at the front exit. The programming used for these functions is shown in Appendix B.

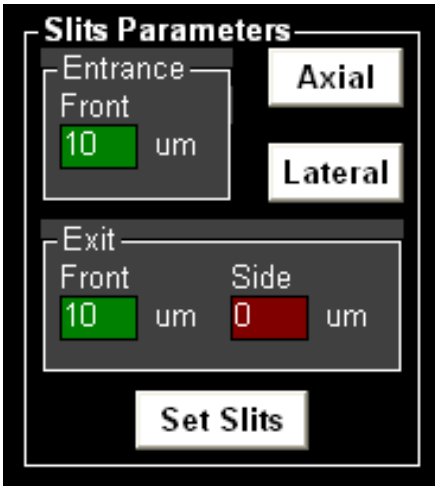

Figure 3.9: *Slits and fold away mirror user interface.*

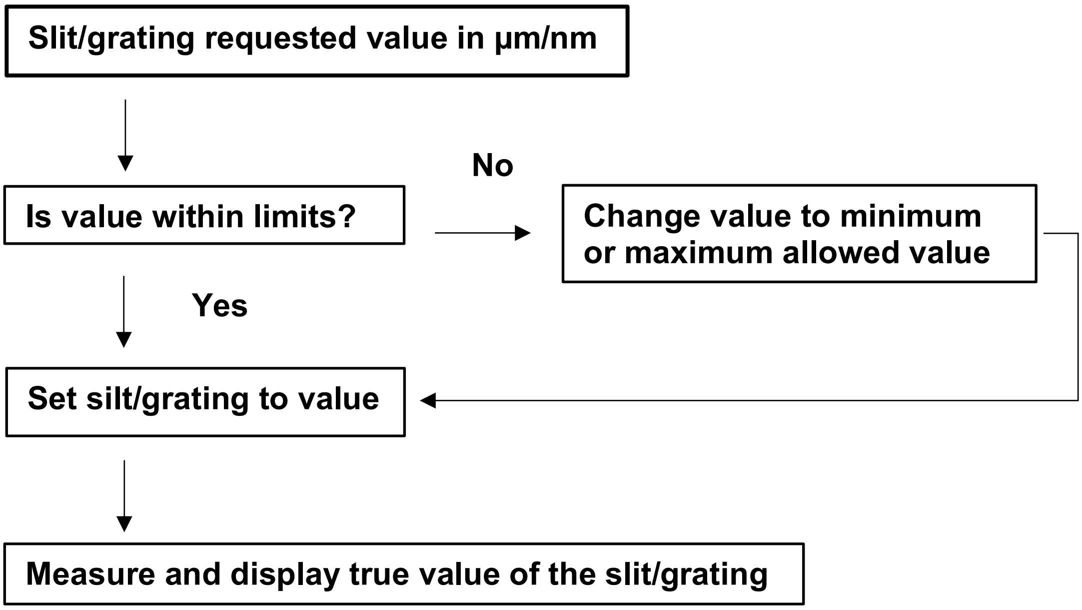

Figure 3.10: *Algorithm for adjusting slit width/grating position.*

Scan spectrum

A sub function was written to scan and record spectrums, by utilising the algorithm logic used to adjust the position of the grating. This is done by the user supplying the Start and Stop Wavelength and the Step Resolution as seen in Figure 3.11, which is then used to adjust the grating sequentially and measuring the resulting intensity. The spectrum is plotted on a graph area as seen in Figure 3.3 and the user has the option to store the data in a DAT file. To improve the quality of the measured spectrum the user has the option to take several data points per wavelength and the average of these values is displayed and stored (Points to Average). The user also has the option to take up to five individual complete scans, which will average the results and display and store the resulting average spectrum (Scans to Average).

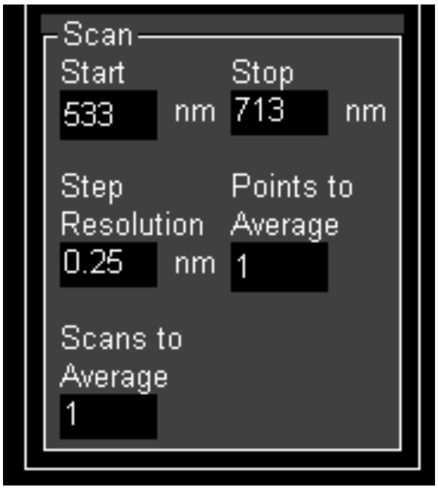

Figure 3.11: *Scan options user interface.*

Grating Settings and Optimisation

As shown in Figure 3.12 the user has the option to select between 1800 lines per mm and the 950 lines per mm diffraction gratings. The code of the sub function that is used to select one of the two diffraction gratings is shown in Appendix B. To allow the user to optimise the light signal, a sub function was written to set the wavelength to a certain value and monitor the resulting intensity, while the user adjusts the position of the convex lens, slits widths and PMT voltage to optimise the signal-to-noise ratio. Usually the strongest emission peak from the sample is used to do the optimisation of the system. The programming was done in such a fashion that it automatically fills the Position textbox with the wavelength corresponding to the maximum intensity of the previous scan.

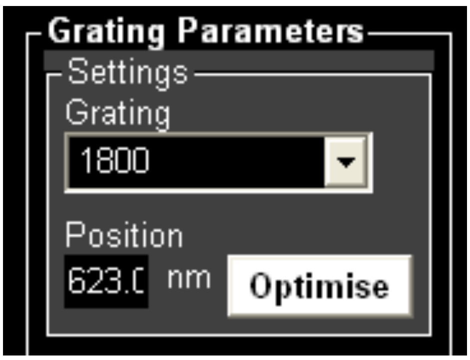

Figure 3.12: *Grating Settings and Optimisation user interface.*

Time Scan Spectrum

To allow the system to automatically scan spectrums at certain time intervals for a period of time, a sub function was written that is included in Appendix B. this sub function achieves this by utilising the information supplied by the user in the textboxes in Figure 3.13. This function is especially important to aid in the study of the optical stability of materials over long periods of time.

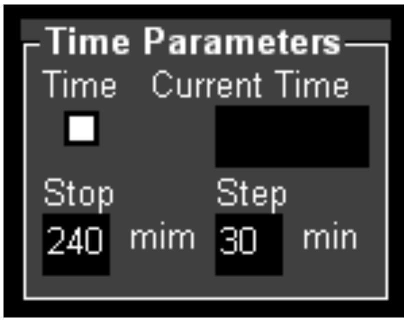

Figure 3.13 *Time Parameters user interface.*

Calibration

The wavelength calibration of the new software was verified with the previous software (HORIBA Jobin Yvon´s Spectrometer Utilities program, SynerJY® data acquisition software) by using a cadmium lamp, Philips 93107E Cd 0.9AL8, Made in Holland, CSIR 2825135 with power supply, 11178 UOVS. This lamp produces sharp well-defined emission peaks as seen in Figure 3.14. This calibration verification was done by placing the lamp in front of the front entrance of the spectroscope. The optical chopper was placed between the lamp and the entrance to allow detection by using the lock-in amplifier. The emission spectrum was then obtained by using the previous and new software as seen in Figure 3.14. There is a good correlation between the peak wavelengths measured with the new software and previous software. However, the relative intensities of the same peaks of the different spectra do not agree. This can be attributed to beating of frequencies of the observed emission that occurs due to the emission of the cadmium lamp that is oscillating at 50 Hz while the optical chopper pulses the emission at 120 Hz. This causes a gradual increase and decrease in the observed light intensity over time which causes the measured intensities of the same peaks to vary.

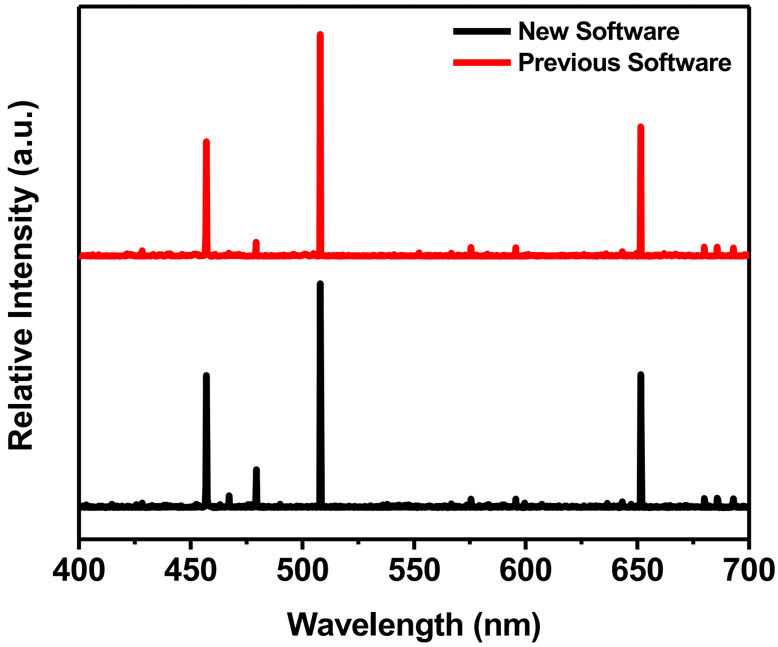

Figure 3.14: *Wavelength calibration using a cadmium lamp.*

3.1.3 Detector

Most PL systems use PMTs for detection of radiation. A PMT is regarded as a light to current converter where the current is proportional to the input light intensity. PMTs are especially useful in low level light detection conditions, because they offer a good signal-to-noise ratio over a wide spectral range and a fast response time. In this section, the focus was on the internal working of these detectors and some aspects to keep in mind when obtaining intensity data from these detectors.

Hardware

The PMT used in this system is a Hammamatsu Photomultiplier Tube R943-02. To achieve light to current conversion and amplification, the PMT consists of a photocathode and a series of dynodes respectively, as seen in Figure 3.16. The photocathode in this PMT is a thin film of gallium-arsenide (caesium) on the inside of a window. Incident visible photons cause the ejection of electrons from this surface due to the photoelectric effect. The photoelectron generation efficiency of these photocathodes is dependent on the wavelength of the incident photons. This is evident in both the quantum efficiency and cathode radiant sensitivity of the PMT as shown in Figure 3.15. This spectral response also depends on both the transparent material used for input window and the type of material used for the thin film photocathode [34]. The Hammamatsu Photomultiplier Tube R943-02 has a wide visible spectral response of 160 nm to 930 nm as seen in Figure 3.15 [35].

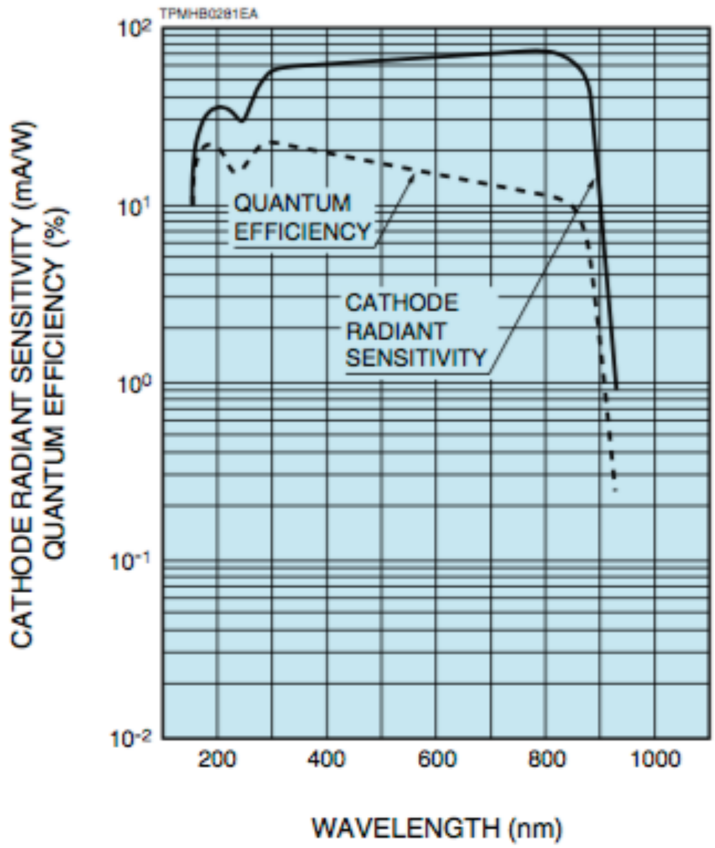

Figure 3.15: *Spectral response of the Hammamatsu Photomultiplier Tube R943-02* ***[35]****.*

To achieve amplification of the photoelectron signal, the gallium-arsenide (caesium) photocathode is held at negative potential of -1500 V, while dynodes are held at negative voltages that decrease along the dynode chain. Ejected photoelectrons are accelerated towards the first dynode which upon collision with the dynode causes 5 to 20 additional electrons to be ejected as shown in Figure 3.16. The number of electrons ejected is proportional to the potential difference. This process continues through the dynode chain which causes a current pulse at the anode. The size of this pulse or the gain is proportional to the overall voltage applied between the cathode and anode of the PMT.

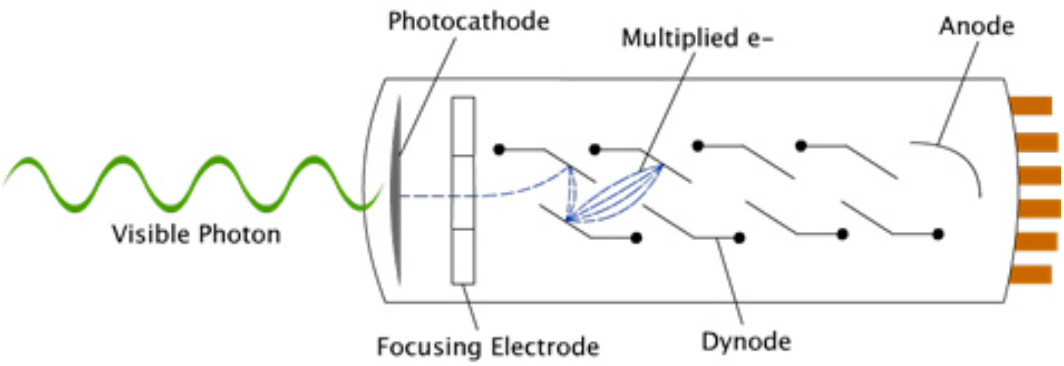

Figure 3.16: *PMT's internal construction* ***[66]***.

For quantitative measurements, a linear response between light intensity and anode current is important. Therefore, constant amplification is achieved by careful control of the high voltage. It is important that this voltage be ripple-free and stable for long periods of time, because as seen in Figure 3.17, a small change in the cathode to anode voltage causes a significant change in gain.

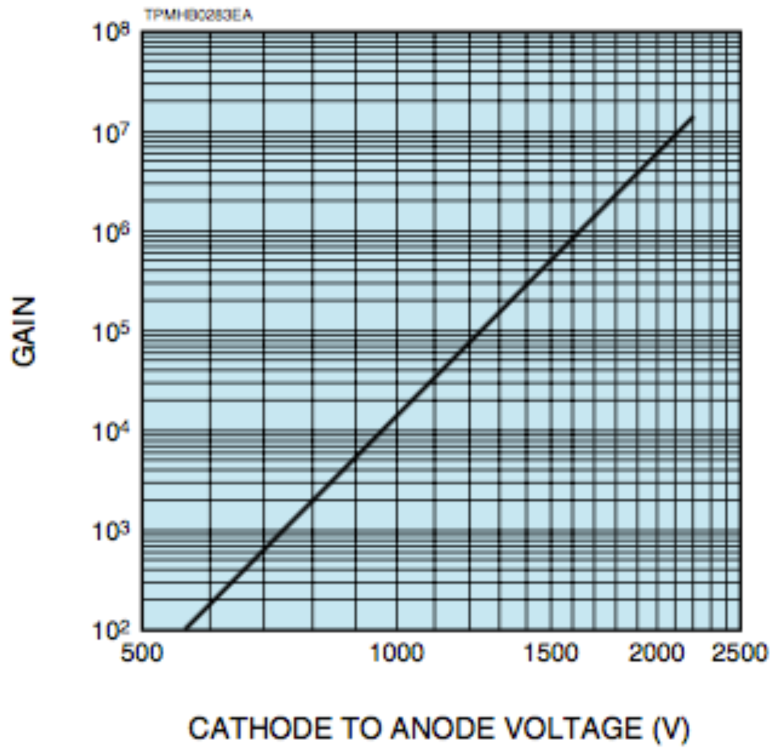

Figure 3.17: *Gain as a function of PMT voltage for the Hammamatsu Photomultiplier Tube R943-02* ***[35]***.

In this system, the PMT is used in analog mode where pulses are averaged. The advantage of this mode is that the gain can be adjusted by changing the cathode to anode voltage of the PMT. This allows for a wider range of signal levels to be detected and also for higher precision of the measurement, due to a higher signal-to-noise ratio. A nonlinear response between light intensity and anode current can result under high intensity illumination. Under this circumstance, the electrical potential between photocathode and first dynode decreases due to the limited current-carrying capacity of the PMT, which in return causes a decrease in the gain. Excessive light can also cause a large amount of current that can damage the photocathode which causes a loss in gain and the dark count to increase.

To prevent excessive light from entering the detector an algorithm was implemented in the programming to shut the slits if the intensity exceeds a certain value as explained in the programming section. To prevent damage caused by scattered light resulting from the excitation source, a filter was placed in front of the spectroscope´s entrance. This filter has an absorbance of 3.14 and 2.05 at 320 nm and 330 nm, respectively. It also has a near zero absorbance from 380 nm to 750 nm [28]. This prevents the 325 nm scattered excitation radiation from entering the PMT, while visible emitted light is transmitted for detection.

In an effort to improve the signal-to noise ratio, the detector is cooled to -30 °C by a C10372 High Performance Thermoelectric Cooler that uses a Peltier element. The heat from the Peltier element is transported by circulated water that allows cooling by utilising the atmosphere in the laboratory. The cooling reduces the thermal electrons emitted from the photocathode of the PMT and therefore reduces the dark counts as seen in Figure 3.18. The thermoelectric cooler is also constructed with electrostatic and magnetic shielding that reduces the effects that external noise on the PMT and in return enhances the signal-to-noise ratio [36]. For this study, the response time of this PMT is not important, however this PMT could possibly be used for life-time measurements, since the transit time is in the nanosecond range, as indicated in Appendix A.

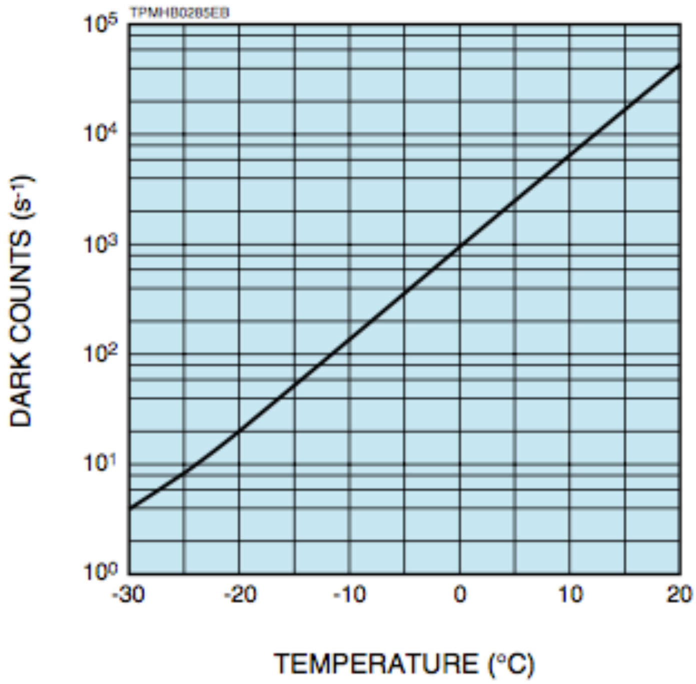

Figure 3.18: *Noise as a function of temperature of the Hammamatsu Photomultiplier Tube R943-02* ***[35]****.*

Programming

To prevent damage of the PMT detector due to light saturation, an algorithm was implemented in the Scan Spectrum and Optimisation functions that monitors the light intensity measured by the lock-in amplifier. If the voltage output by the lock-in amplifier exceeds 2.5 V the slits value is automatically changed to zero and the diffraction grating is moved to the position of the Start Wavelength, in an effort to prevent excessive light from entering and damaging the PMT detector.

3.1.4 Lock-in amplifier

Lock-in amplifiers are used to accurately amplify and measure small voltage signals, even if these small signals are obscured by large noise sources. The Stanford Research Systems, Model SR830 DSP Lock-In Amplifier, achieves a high signal-to-noise ratio by using a technique called phase-sensitive detection that singles out the component of the signal at a specific reference frequency and phase. Noise signals at other frequencies are rejected and do not affect the measurement. Figure 3.19 shows the output signal from the PMT detector while measuring the light signal of a luminescent material.

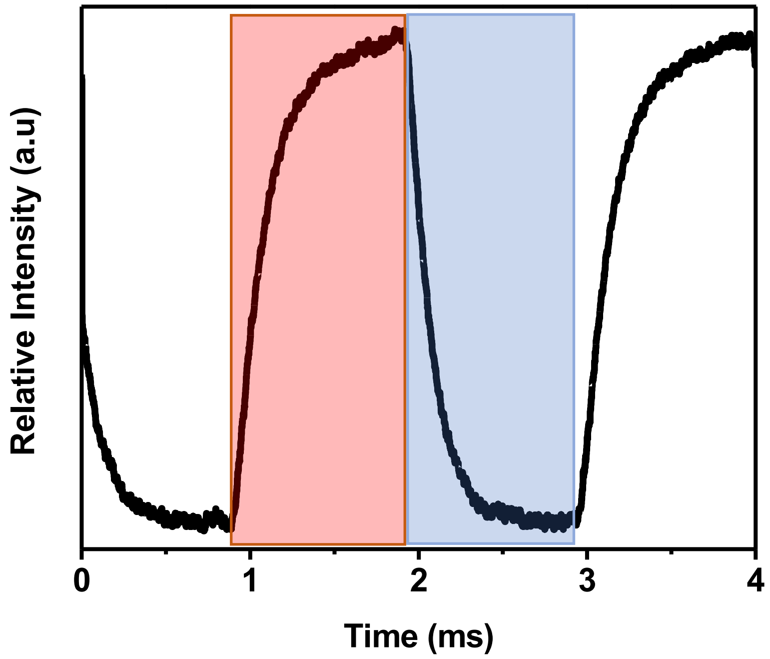

Figure 3.19: *Measured PMT output signal.*

The part of the signal in the red block, represents the emission of the phosphor material as it is being excited with the pulsed excitation source and the part of the signal in the blue block, represents the decay of the phosphor material´s emission as it is no longer irradiated by the excitation source. Fourier´s theorem states that any signal can be represented as a sum of an infinite set of sine waves of different amplitudes, frequencies and phases [37]. Therefore, one of the components of the output signal in Figure 3.19 is a sine wave, as shown in Figure 3.20, which is mathematically described by Equation 3.3:

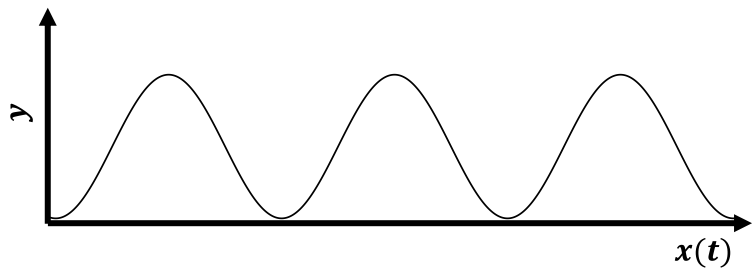

Figure 3.20: *Sine wave signal.*

$$y = V_{sig} \sin \left(\omega_r t + \theta_{sig}\right) \quad \textbf{\textit{3.3}}$$

where V_{sig} is the amplitude of the signal, ω_r is the frequency of the signal and θ_{sig} is the phase difference between signal and reference signal. For phase-sensitive detection to be possible a reference signal is required. In this case the excitation source is pulsed at a fixed frequency by an optical chopper. As seen in Figure 3.21, the Chopper Frequency Control provides an external clock reference signal in the form of square wave with a frequency that is equivalent to that of the pulsed excitation source. This square wave signal is then supplied to the lock-in amplifier that produces a synchronous sine wave, as seen in Figure 3.21, that can be represented by Equation 3.4:

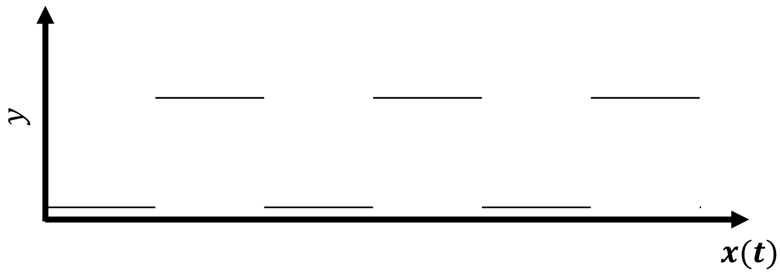

Figure 3.21: *External clock reference signal.*

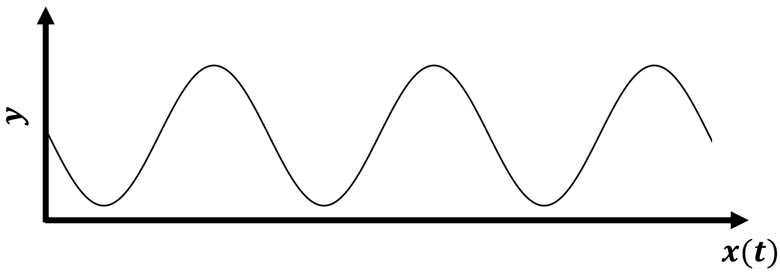

Figure 3.22: *Sine wave reference signal.*

$$y = V_L sin\ (\omega_L t + \theta_{ref}) \qquad \textbf{3.4}$$

where V_L is the amplitude of the reference signal, ω_L is the frequency of the reference signal and θ_{ref} is the phase difference between the reference signal and the signal. To establish the phase-sensitive detection signal V_{PSD}, the lock-in amplifier multiplies the signal and reference signal as seen in Equation 3.5.

$$V_{PSD} = V_L V_{sig} sin\ (\omega_r t + \theta_{sig}) sin\ (\omega_L t + \theta_{ref}) \qquad \textbf{3.5}$$

By using the product identity for multiplying two sine-waves the following expression is obtained.

$$V_{PSD} = \frac{1}{2} V_L V_{sig} \, cos([\omega_r - \omega_L]t + \theta_{sig} - \theta_{ref}) - \frac{1}{2} V_L V_{sig} \, cos([\omega_r + \omega_L]t + \theta_{sig} + \theta_{ref}) \qquad \textbf{3.6}$$

The phase-sensitive detector has an output that has two alternating signal components of which one is the difference and the other the sum of the frequencies ω_r and ω_L. When this output is passed through an alternating current and low pass filter, the alternating current signals and noises are removed. However, in the case where ω_r is equal to ω_L Equation 3.6 reduces to:

$$V_{PSD} = \frac{1}{2} V_L V_{sig} \, cos(\theta_{sig} - \theta_{ref}) \qquad \textbf{3.7}$$

which is a direct current signal which is proportional to the signal. The lock-in amplifier therefore only allow the detection of signals and noise with a frequency that is equal to that of the of the reference signal. Noise signals at frequencies far from the reference are removed by a low pass filter while noise signals at frequencies close to the reference are removed by the phase-sensitive detector. For this to be possible it is necessary that the reference frequency and the signal frequency are the same and that the signal and reference are phase-locked, otherwise V_{PSD} will not be a direct current signal. This is ensured by adding a second phase-sensitive detector, where the signal is multiplied with the reference signal shifted by 90° as shown in Equation 3.8.

$$V_{PSD2} = \frac{1}{2} V_L V_{sig} \, sin(\theta_{sig} - \theta_{ref}) \qquad \textbf{3.8}$$

Equation 3.3 is known as the in-phase component X and Equation 3.8 as the quadrature component Y. By calculating the magnitude R of the signal vector, the phase dependency is removed and the signal amplitude is obtained which is independent from the phase difference between the signal and the reference signal.

$$R = (X^2 + Y^2)^{1/2} = V_{sig} \qquad \textbf{3.9}$$

V_{sig} is a direct current voltage that is proportional to the light intensity detected and can be configured to the front panel output of the lock-in amplifier. This output is updated at a rate of 512 Hz and has a full scale of 10 V [38]. However, to protect the PMT detector from damage due excessive light the output is limited to 2.5 V. This voltage was supplied to the analog-to-digital converter as explained in the next section.

3.1.5 Analog-to-digital/digital-to-analog converter

A USB-30D16-BNC MicroDAQ was used for this study as an interface between the PL system and a computer. This analog-to-digital converter is a multi-functional data acquisition input device with a 16-bit resolution and a configurable sampling rate of up to 1 MHz. The input voltage that can be measured by this device is in the range of ±5 V. This specific device can also be configured as a digital-to-analog converter to output voltages with a 16-bit resolution in the range of ±10 V. Fast communication was established between the MicroDAQ and computer with use of a Universal Serial Bus cable. To allow the read and write of voltages with the MicroDAQ the necessary EDR Enhanced Software Development Kit and program modules for Visual Basic 6 was installed on a computer [39].

Figure 3.23: *MicroDAQ USB-30D16-BNC* ***[39]****.*

Hardware

This MicroDAQ has eight BNC input ports and 4 output ports in the form of a 9-pin D-type connector. The different apparatus was connected by BNC connectors and a 9-pin D-subminiature connector to the input and output ports of the MicroDAQ as listed in Table 3.1. Also given in Table 3.1 is the input and output ranges that is required from the MicroDAQ for each apparatus. It is important to keep in mind that the maximum read and write resolution possible with this analog-to-digital/digital-to-analog converter is 0.15 and 0.3 mV respectively.

Table 3.1: *Apparatus connected to MicroDAQ USB-30D16-BNC.*

Apparatus, port connected to MicroDAQ	**MicroDAQ´s channel number**	**MircoDAQ´s input or output ranges (V)**
Lock-In Amplifier, front panel signal voltage output channel 1	Input Channel 0	0-2.5
Temperature Controller Unit, signal voltage output	Input Channel 1	0-5
Temperature Controller Unit, LM35 Temperature Sensor voltage output	Input Channel 2	0-5
Laser Intensity Meter, signal voltage output	Input Channel 3	0-0.55
Temperature Controller Unit, signal voltage input	Output Channel 0	0-4.2
Temperature Controller Unit, relay switch control	Output Channel 1	0-5

Calibrations

The MicroDAQ was used in the calibrations of the temperature controller unit and Laser Intensity Meter by use of a custom program. The absolute signal from the lock-in amplifier was not calibrated because only the relative intensity values are of importance for this study.

The intensity is therefore labelled as Relative Intensity and the unit label arbitrary unit (a.u.) is used. Figure 3.24 shows the noise from the lock-in amplifier that is read by the analog-to-digital converter. This noise is not random noise and has the form of a sine wave with a frequency of 50 Hz. This noise was caused by the alternating current from the mains grid that also oscillates at 50 Hz. This noise is present on all the input apparatus and can influence the signal that is measured. In an effort to remove this effect the analog-to-digital converter was configured to take voltage measurements at a frequency of 50 kHz. After each 1011 readings, the average value is taken that represents the true value without the 50 Hz noise [40]. Voltage spikes from the PMT occur occasionally during the measurement, as seen at around 0.02 seconds in Figure 3.24. These spikes are usually represented by one data point and it could be problematic to distinguish it from a true measurement. However, due to the large number of data points measured the effect of these spikes can be ignored.

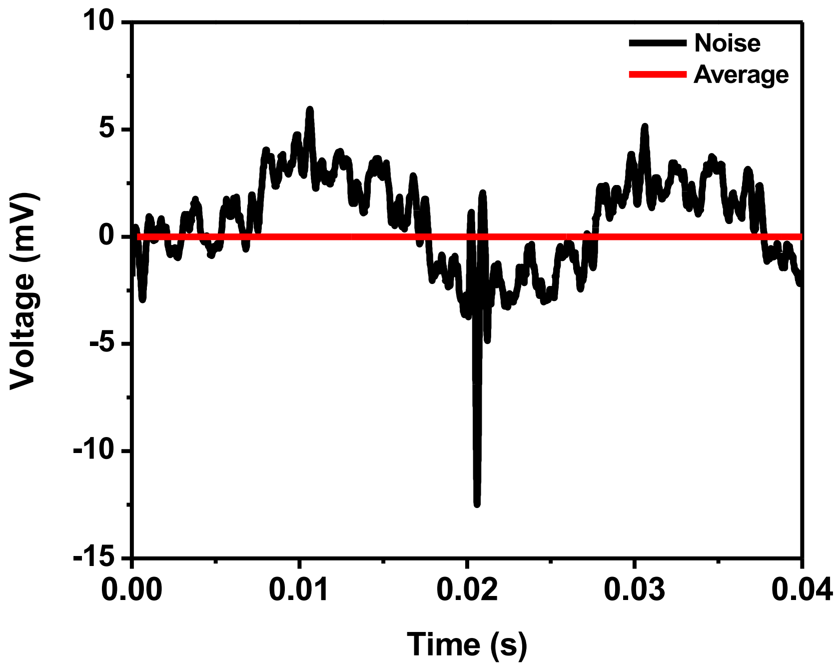

Figure 3.24: *Lock-in amplifier's noise output.*

Programming

The MicroDAQ needs to be initialised each time the program is loaded. In this procedure, the MicroDAQ is setup to measure the 4 input channels at 200 kHz as shown in Appendix B. Due to the fact the channels are measured sequentially, each channel is measured at a rate of 50 kHz. During measurement of a spectrum the readings from the input channels are requested and the MicroDAQ starts the collection of the data which is stored in an array on the on-board memory of the MircoDAQ [40]. This is done until a total of 4044 data points has been collected. The data is then transferred from the MicroDAQ to the computer where the data for each input channel is sorted into their own array. Lastly the average for each array is calculated. These averages represent the values read from the apparatus and it then used in calibration functions to calculate the physical quantity it represents. The programming code for this procedure is shown in Appendix B.

3.1.6 Temperature controller

To control and measure the temperature of the phosphor material under investigation, a temperature controller unit, XYZ stage, sample heater and sample holder were designed and developed as shown in Figure 3.25, in collaboration with the Electronics and Instrumentation Divisions at the University of the Free State. The necessary hardware development, calibrations and programming that were done for this apparatus is discussed in this section.

Figure 3.25: *Temperature controller unit, XYZ stage, sample heater and sample holder.*

Hardware

To allow heating and excitation of the material analysed, a copper (Cu) sample holder was designed and developed. This custom-made sample holder was designed to be placed inside a heating element. Figure 3.26 shows the sample holder´s design and a photo of the final product. The sample holder consists of a Cu cylinder with a 2 mm hole in the centre, in which the sample could be loaded. It also contains a 1 mm hole off centre, in which a thermocouple junction could be inserted to measure the temperature of the sample. The sample´s hole is small in an effort to ensure that the sample is in thermal equilibrium with the holder and that the laser beam with a diameter of 0.91 mm only excites the sample material.

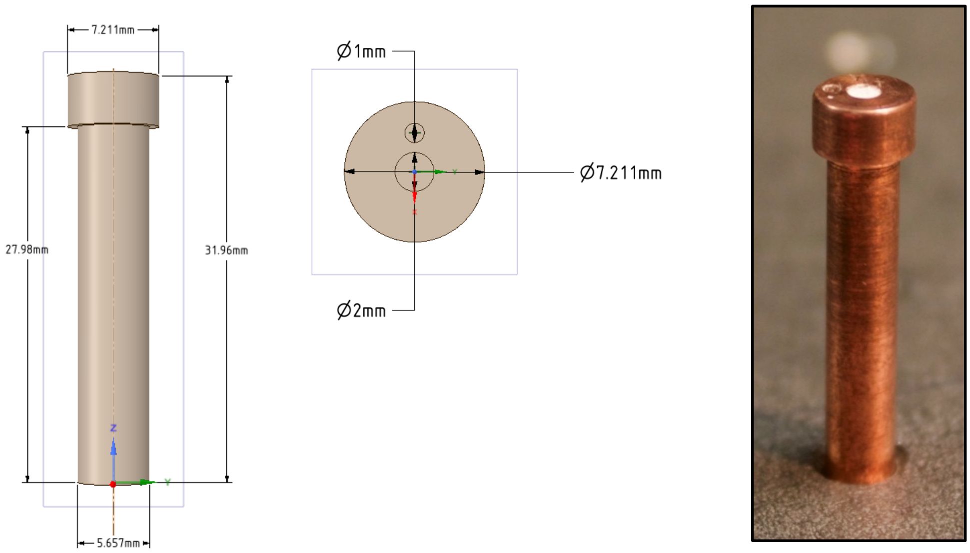

Figure 3.26: *Sample holder´s design and final product.*

The heating element was connected to the temperature controller unit which supplied voltage and current to achieve controlled heating. A nickel-chromium/nickel-aluminium (K-type) thermocouple junction was partially encapsulated in the Cu sample holder near the sample itself. This provides a thermoelectric voltage that is proportional to the temperature of the sample holder. The sample temperature together with the desired temperature was used by an on-board proportional-integral-derivative (PID) controller logic to control the current to the heating element that ultimately controls and regulates the temperature of the sample. The relationship between the temperature and the thermoelectric voltage k is expressed by the following equation:

$$Thermoelectric\ Voltage = k(T_{Sample\ Temperatre} - T_{Reference\ Temperature}) \qquad \textbf{3.10}$$

where $T_{Sample\ Temperatre}$ is the temperature of the sample holder and $T_{Reference\ Temperature}$ is the temperature of the reference junction inside the temperature control unit [41]. The relationship between the temperature and the thermoelectric voltage is given by the K-Type Thermocouple Reference Table [42]. The relationship between the thermoelectric voltage and the temperature is shown in Figure 3.27. At first glance the relationship appears to be linear, however on closer inspection, it was found that a linear fit and the true relationship differ a few °C as shown in Figure 3.28.

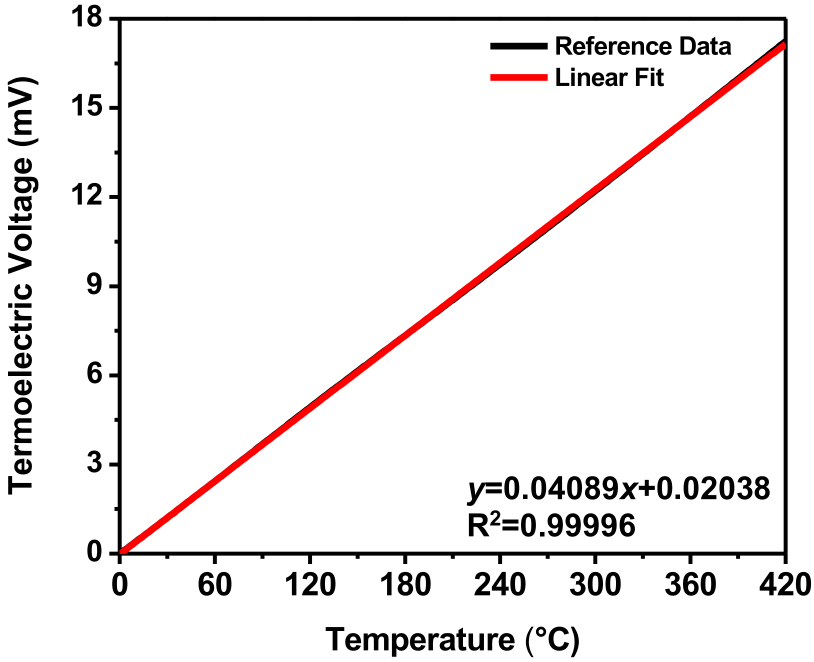

Figure 3.27: *Reference values (full range).*

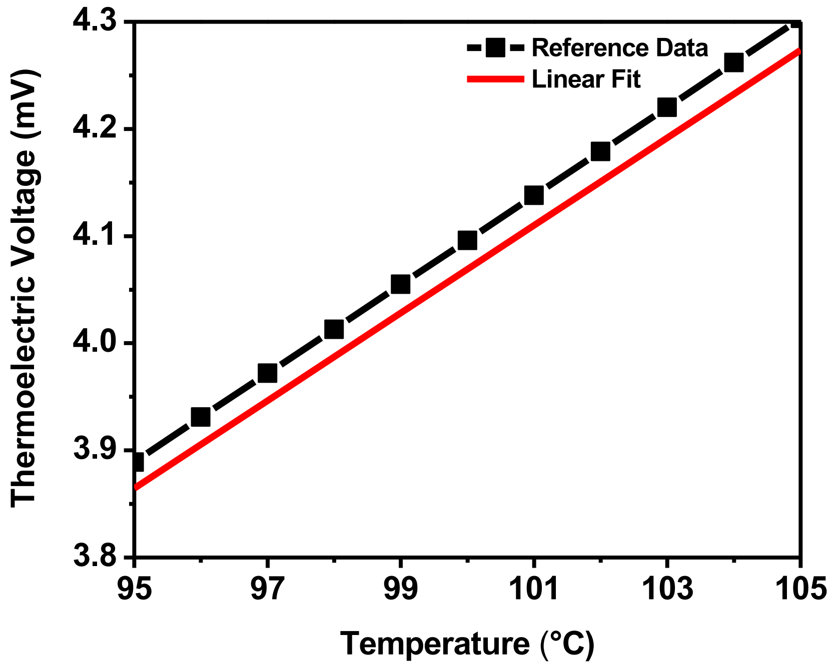

Figure 3.28: *Reference values (small range).*

The true relationship between the thermoelectric voltage and the temperature could be expressed as a complex polynomial function. However, to achieve greater accuracy it was decided to determine the temperature by measuring the amplified thermoelectric voltage and reading the corresponding temperature from the Thermocouple Reference Table. Since the reference table´s data points are in increments of 1 ºC, a linear fit between the two closest points is used to estimate the temperature. The electronics used to determine the thermoelectric voltage resulting from the sample temperature was constructed and modified as shown in Figure 3.29. As seen in Figure 3.27 the thermoelectric voltage is a small value, therefore an amplifier is used to amplify the value and it is then read by the analog-to-digital converter (ADC) which displays a voltage reading on the computer.

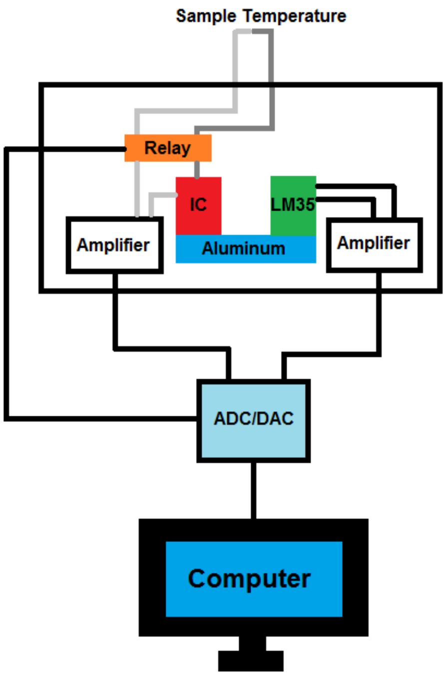

Figure 3.29: *Temperature measurement system.*

As shown in Figure 3.29, to add the effect of the reference temperature an integrated circuit (IC) measures the ambient temperature inside the temperature controller unit, which then adds the corresponding voltage value to the thermoelectric voltage which is then amplified. To determine this ambient temperature the unit was modified with an extra temperature sensor (LM35) that is in thermal equilibrium with the integrated circuit. This value is also amplified by an amplifier and the value is read by the analog-to-digital converter (ADC) which displays a voltage reading on the computer. A relay switch is also present that allows the isolation of the reference junction. This relay can be switched on by a 5 V voltage supplied from the digital-to-analog converter (DAC) that is controlled from the computer. A stand was also designed and developed that allows stable positioning in the x-, y- and z-directions of the sample holder and heating element. Figure 3.30 shows the stand´s design and a photo of the final product. This stand was bolted to the optical table to allow the sample to be as stable as possible during measurements.

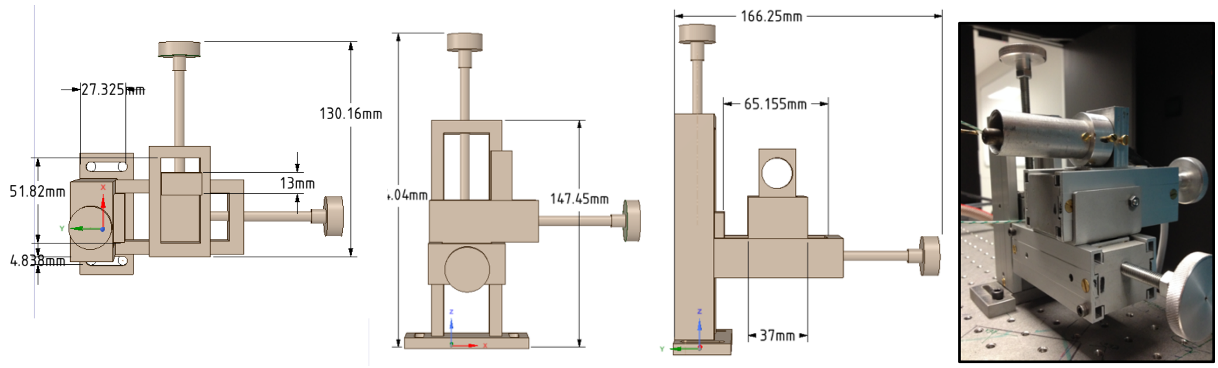

Figure 3.30: *XYZ stage´s design and final product.*

Calibrations

Temperature Read

It is clear from the previous section that calibrations were necessary for the various components of this temperature measurement system. To determine the amplification of the amplifier that amplifies the thermoelectric voltage, the thermocouple was replaced by a Direct Current Voltage Calibrator (Model 1010, Time Electronics). This was used to simulate the thermoelectric voltage while the corresponding amplified voltage was measured and recorded on the computer. This was done from 0 to 20 mV in 0.2 mV increments and as seen in Figure 3.31 the measured relationship is linear. Therefore, the amplification can be calculated by the obtained linear equation. As seen in Figure 3.32 this linear equation also provides good correlation in small ranges. Figure 3.31 shows that the y-intercept is not equal to zero. This is due to the effect of the reference junction value which is influenced by room temperature. During the calibration procedure, the room temperature was measured with a mercury thermometer to be at 20 °C on average. To ensure that the calibration is as accurate as possible, the calibration procedure was executed quickly to prevent large fluctuations in the room temperature that would influence the calibration. However, for the calibration this room temperature reading was ignored but for a measurement it is important to determine this value.

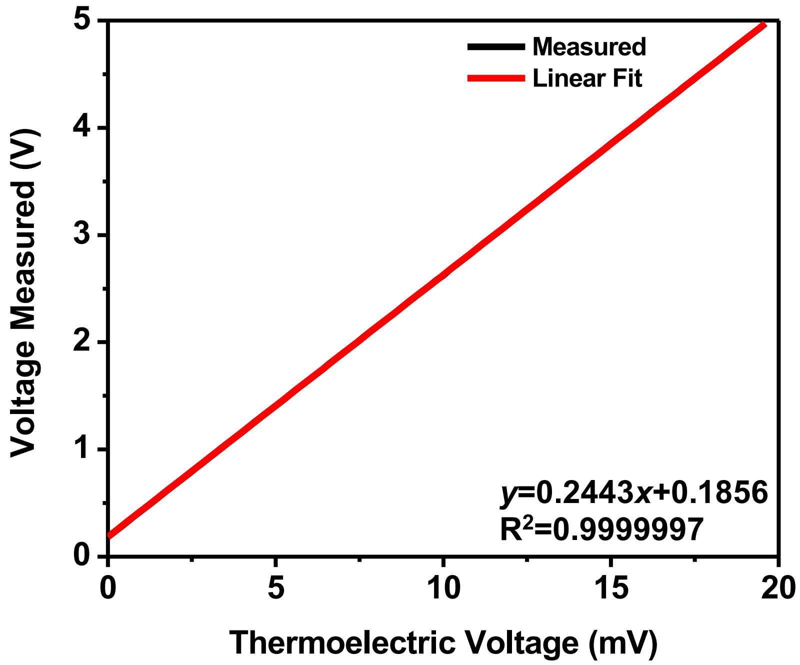

Figure 3.31: *Amplifier´s calibration (full range).*

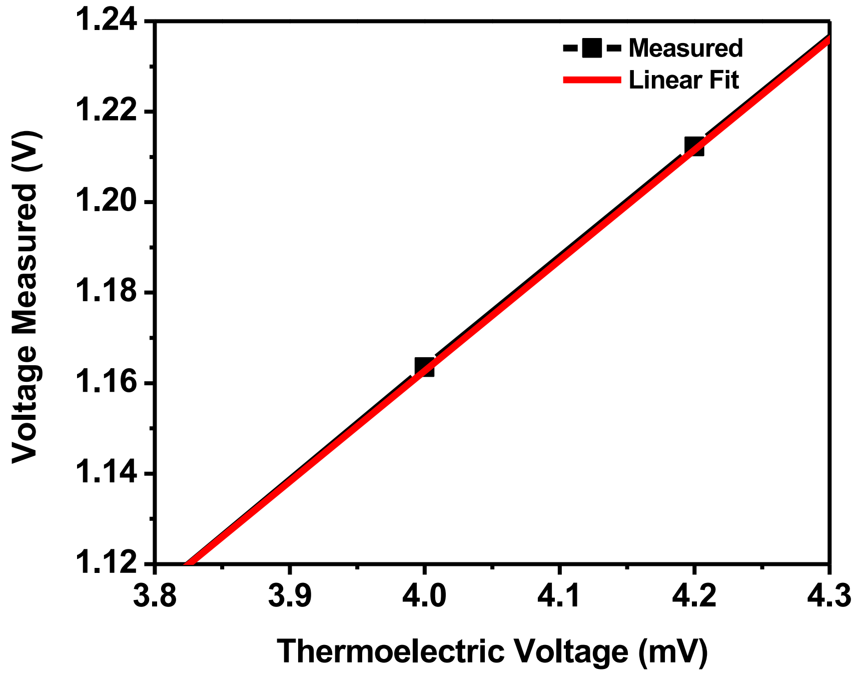

Figure 3.32: *Amplifier´s calibration (small range).*

To determine the integrated circuit´s temperature and the voltage that it adds to the thermoelectric voltage, the voltage resulting from the LM35 temperature sensor was utilised.

However, a calibration was needed in order to determine the relationship between the integrated circuit voltage and the LM35 temperature sensor voltage. To isolate the reference junction and integrated circuit from the sample temperature during the calibration process, the relay was switched on. It is important to note that the measured values in this section are voltages that were used to determine the calibration, but to make the graphs interpretable the voltages were converted to their corresponding temperature values. Figure 3.33 shows the measured temperature by the integrated circuit and LM35 temperature sensor as a function of time, with the unit being switched on at 60 seconds. There can be seen that the integrated circuit´s temperature starts higher than the LM35 temperature sensor´s temperature, but gradually falls before it steadily increases again. The LM35 temperature sensor´s temperature however gradually increased over time. This gradual increase for both the integrated circuit´s and LM35 temperature sensor´s temperatures is due to the internal temperature of the unit that increases as a result of the electronics that heat up. In Figure 3.34 the derivative of the difference between the two values squared show that the integrated circuit and LM35 temperature sensor stabilise to one another at about 600 seconds after start-up. It was therefore imperative to wait at least 10 minutes after start-up before temperatures readings were taken.

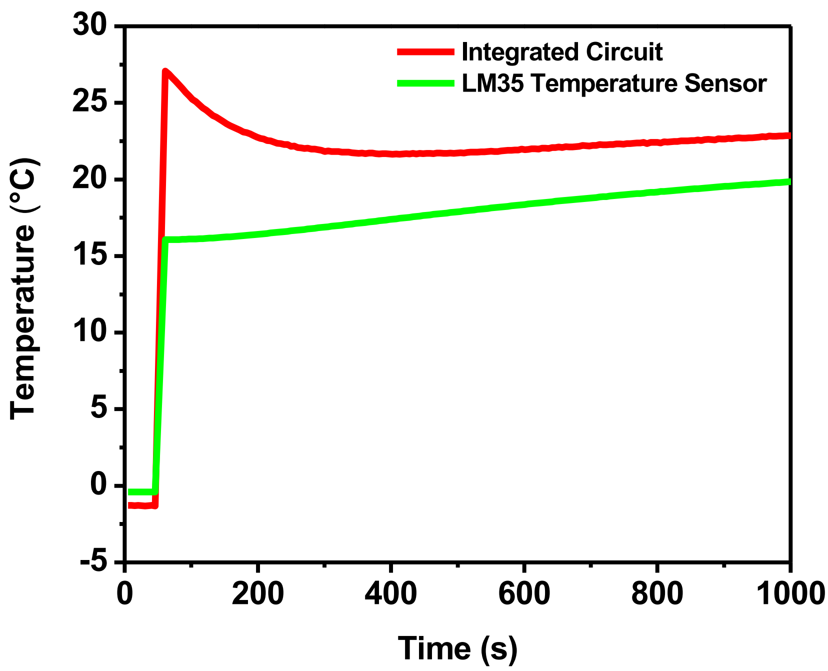

Figure 3.33: *Integrated circuit´s and LM35 temperature sensor´s readings after start-up.*

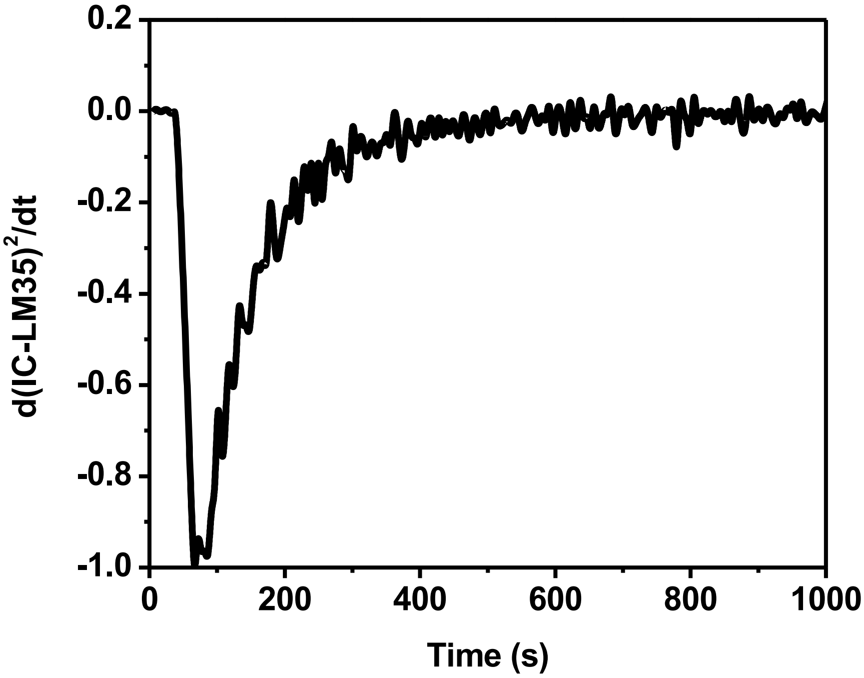

Figure 3.34: *Determination of stabilisation period.*

To perform the calibration between the integrated circuit´s and the LM35 temperature sensor´s voltages the unit was given an hour to stabilise. To simulate variation in room temperature the environment of the integrated circuit and LM35 temperature sensor was heated using a heat source. Heating was ceased and the voltages of the integrated circuit and LM35 temperature sensor was recorded as it cooled down to room temperature. This was done using the custom programmed computer program to record data points in order to plot Figure 3.35. As shown in Figure 3.36 only a portion of the data collected, with which a reasonable room temperature can be represented, was used for the calibration. The calibration between the two temperatures is shown in Figure 3.37. As seen, the relationship between these values can be represented by a linear fit. The calibration values that were obtained were incorporated into the computer program that ultimately allows the determination of the sample temperature.

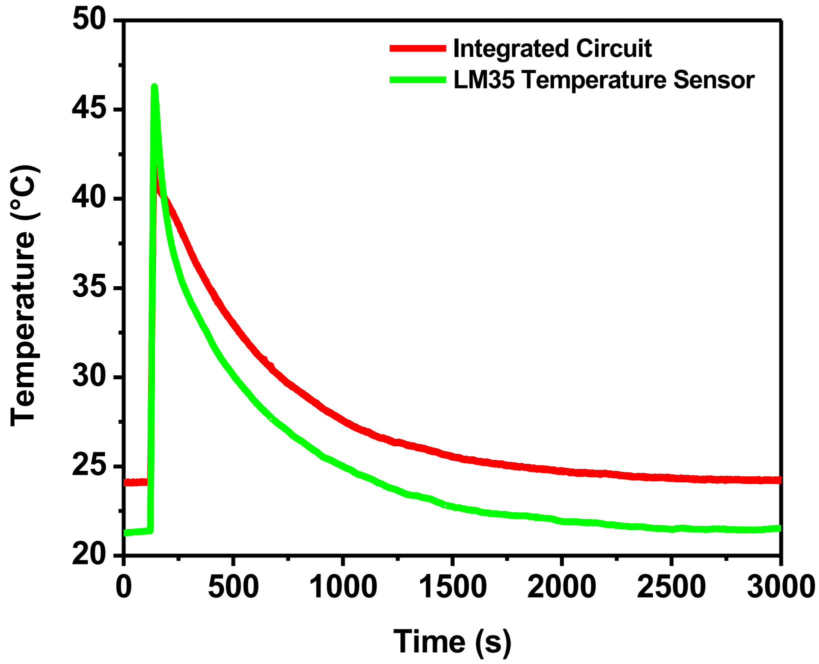

Figure 3.35: *Integrated circuit and LM35 temperature sensor temperature readings after heating.*

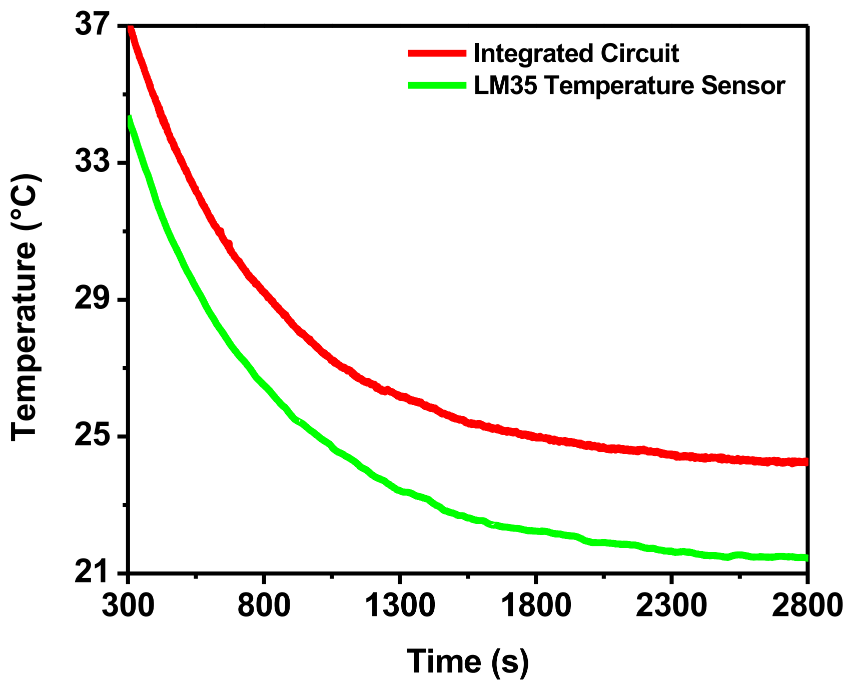

Figure 3.36: *Portion of data used to determine calibration.*

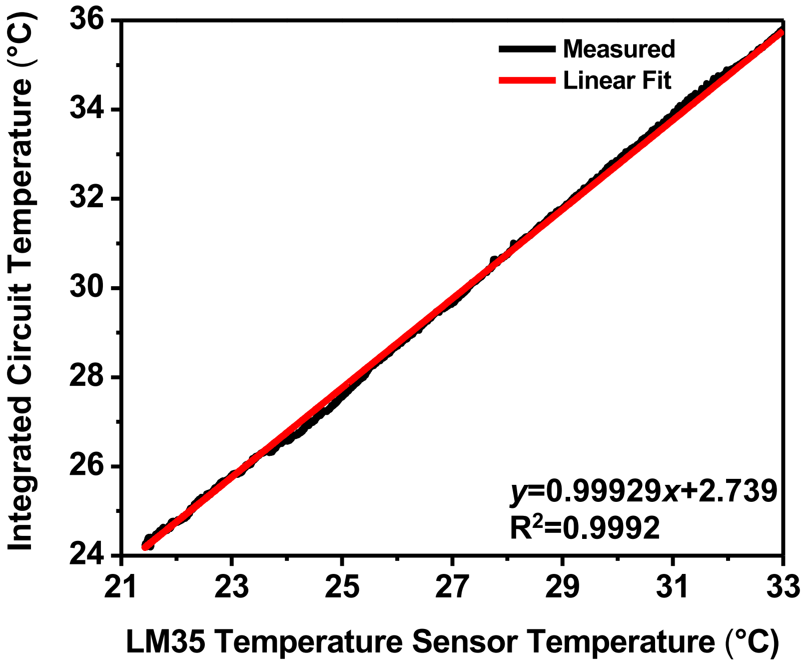

Figure 3.37*: Calibration between the temperature readings of the integrated circuit and LM35 temperature sensor.*

Temperature Set

By supplying the temperature controller unit with a voltage input between 0 to 4.2 V, the temperature of the sample is adjusted from room temperature to 420 °C. This voltage was supplied by the digital-to-analog converter that is controlled by the computer. The calibration between the desired temperature and the voltage supplied was refined and is shown in Equation 3.11. This calibration was incorporated into the programming.

$$Voltage = Temperature \times 0.01029\, V/℃ - 0.035\, V \qquad \textbf{\textit{3.11}}$$

By using this calibration, an estimated one to one relationship between the desired temperature (Temperature Set) and the measured temperature (Average Temperature Read) could be achieved as shown in Figure 3.38. Figure 3.38 shows that the relationship between the Temperature Set and the Average Temperature Read is linear, however Figure 3.39 shows that there is deviation from this linear relationship on smaller temperature ranges. Due to several environmental factors the influence this calibration and because of the large temperature range it encapsulates, programming was used to refine the process to achieve correlation between the desired temperature and the measured temperature, as will be discussed in the programming section.

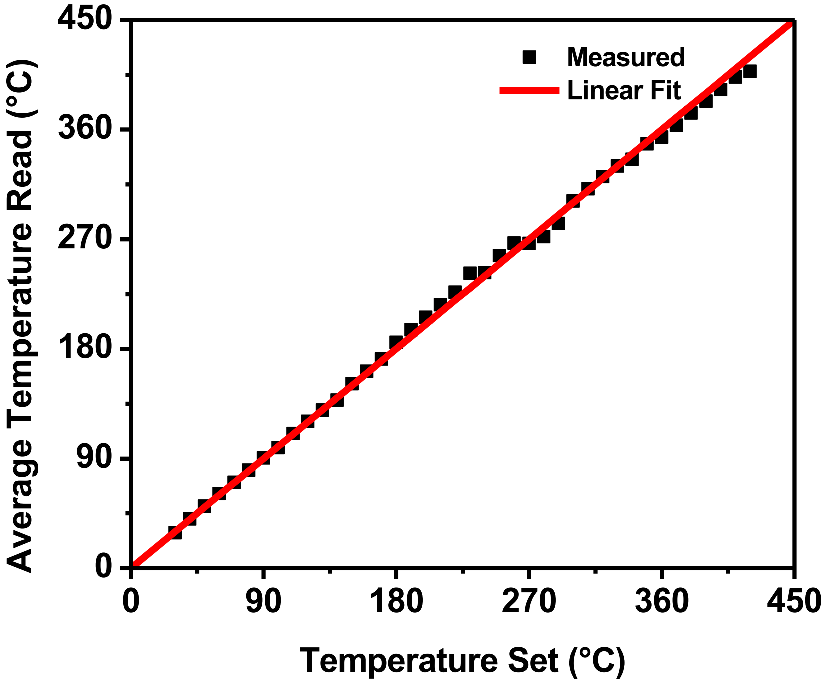

Figure 3.38: *Relation between desired temperature and measured temperature (full range).*

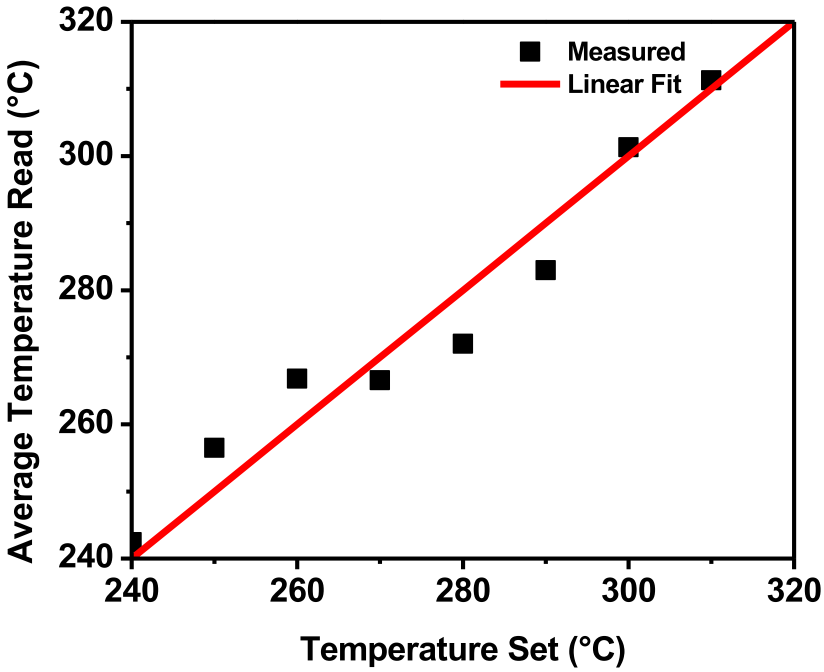

Figure 3.39:*Relation between desired temperature and measured temperature (small range).*

Programming

Temperature Read

The K-Type Thermocouple Reference Table, containing Temperature and corresponding Thermoelectric Voltage, was loaded in an array at the start-up of the program [42]. The following algorithm shown in the flow diagram was used to determine the sample temperature and the Reference Temperature by using the voltage values measured by the analog-to-digital converter.

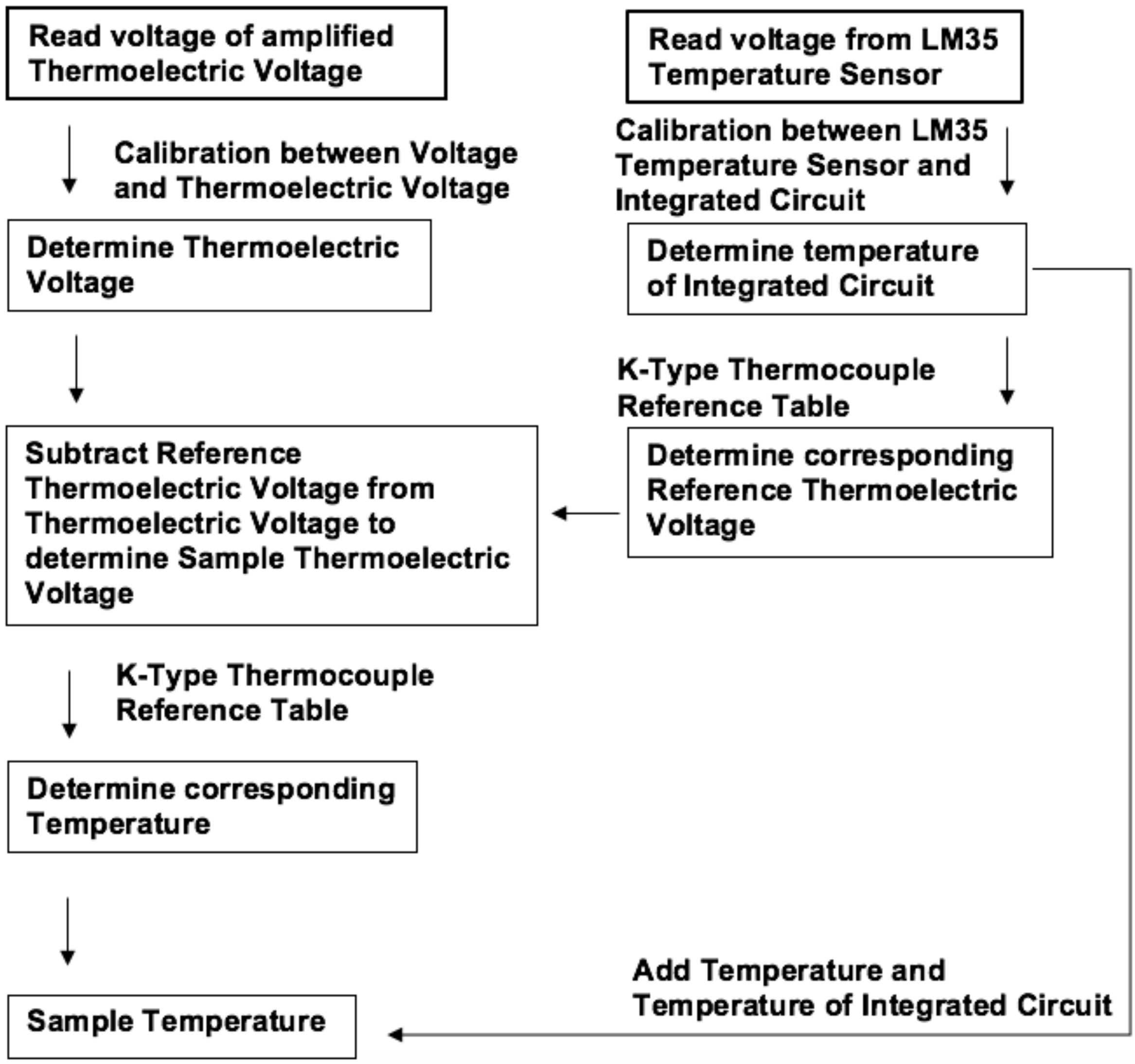

Figure 3.40: *Algorithm to determine the sample temperature and the Reference Temperature.*

After this procedure, the sample temperature and temperature of the integrated circuit was displayed and recorded. This is done for each wavelength data point and allow the monitoring of the temperature while a scan is taken as shown in an example shown in Figure 3.41. This example indicates that the fluctuations in the temperature is small throughout the emission scan with an average temperature of 98.8 °C and a standard deviation of 0.1 °C. This is a valuable tool because it allows for the justification of the direct comparison of different emission spectra and the different wavelength regions of the emission spectra. These temperature values can be averaged, and the emission spectrum can be labelled with its corresponding average temperature. For more details regarding the programming see Appendix B or the supplied compact disc.

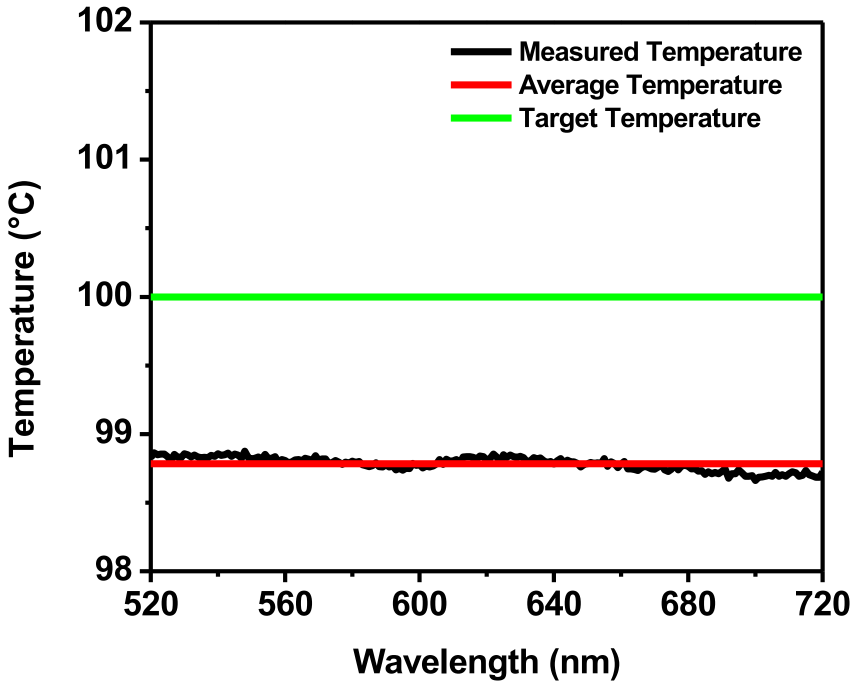

Figure 3.41: *Temperature fluctuations during emission scan.*

Temperature Write

As seen in Figure 3.42 the user could either use the program to select a single temperature at which a spectrum must be obtained (Temp. Set) or a temperature scan can be done, where spectrums are automatically measured at a series of specific temperatures (Temperature Scan). Figure 3.41 indicates that the Target Temperature was 100 °C while the Average Temperature throughout the scan was determined as 98.8 °C. This deviation is attributed to several environmental factors. Figure 3.41 also show that the temperature steadily decreases throughout the scan, which is attributed to thermal instability throughout the sample and sample holder while the measurements were obtained.

Figure 3.42: *User interface of temperature parameters.*

In an effort to address these problems, the program was designed with the intelligence to adjust the temperature to the Target Temperature and to monitor fluctuations in the temperature to ensure that the spectrum is measured when thermal equilibrium throughout the sample and sample holder is achieved. In this case, thermal equilibrium is regarded as being achieved when the temperature fluctuates within a user defined range (Accuracy Band) for a user defined time interval (Stabilisation Time). This was achieved by incorporating an algorithm as explained in the following flow diagram. For more details about the programming sight Appendix B or the supplied compact disc.

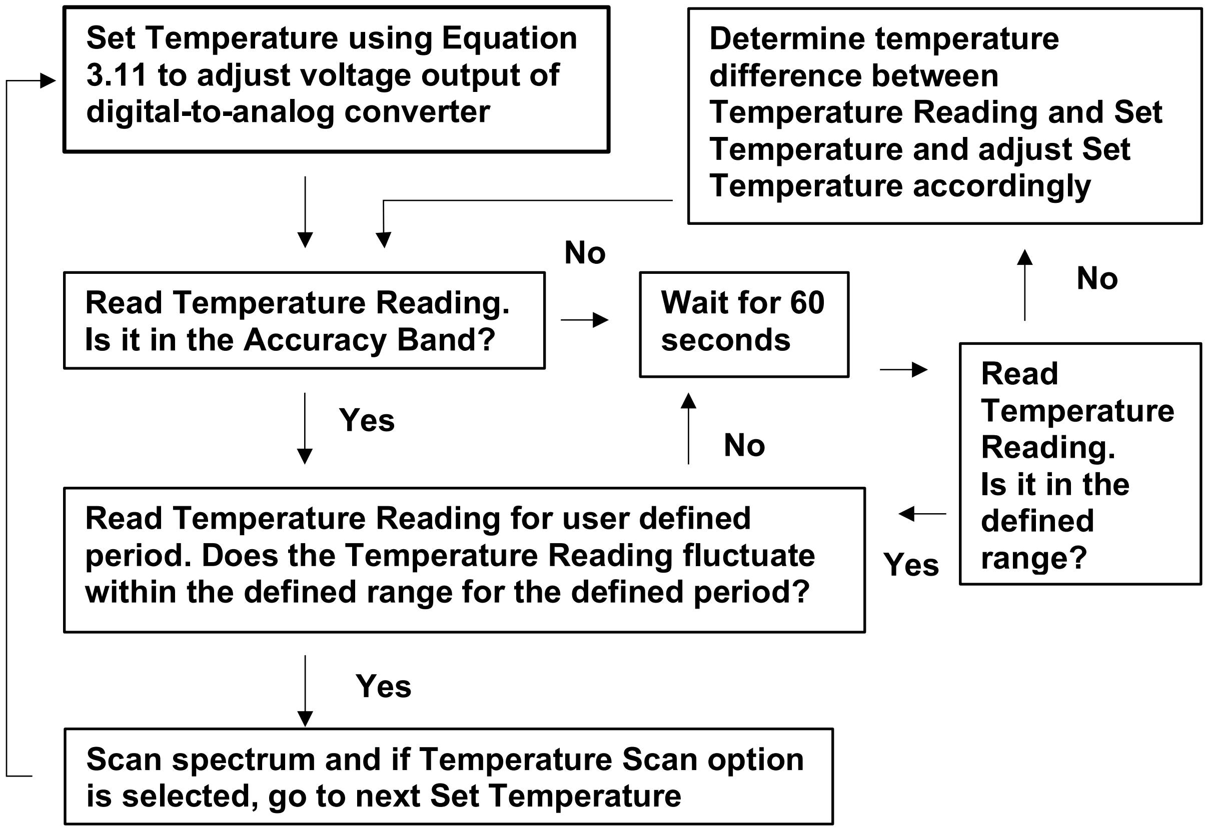

Figure 3.43: *Algorithm to correlate Set Temperature and Temperature Reading.*

3.2 Fluorescence spectroscopy

In this study excitation spectra and lifetime measurements were obtained for the material under investigation with the Varian Cary Eclipse fluorescence spectrophotometer. Shown in Figure 3.44 is the internal construction of this apparatus. This system works on the same principles as the PL system as described in the previous section. However, this system uses a Xenon flash lamp as excitation source and therefore the wavelength of excitation (pictured in blue) can be adjusted from the ultraviolet to the visible region by using a diffraction grating. The wavelength of the resulting emission (pictured in orange) is measured by a spectrometer which obtain the intensity of the different wavelengths of light by using a PMT detector [43].

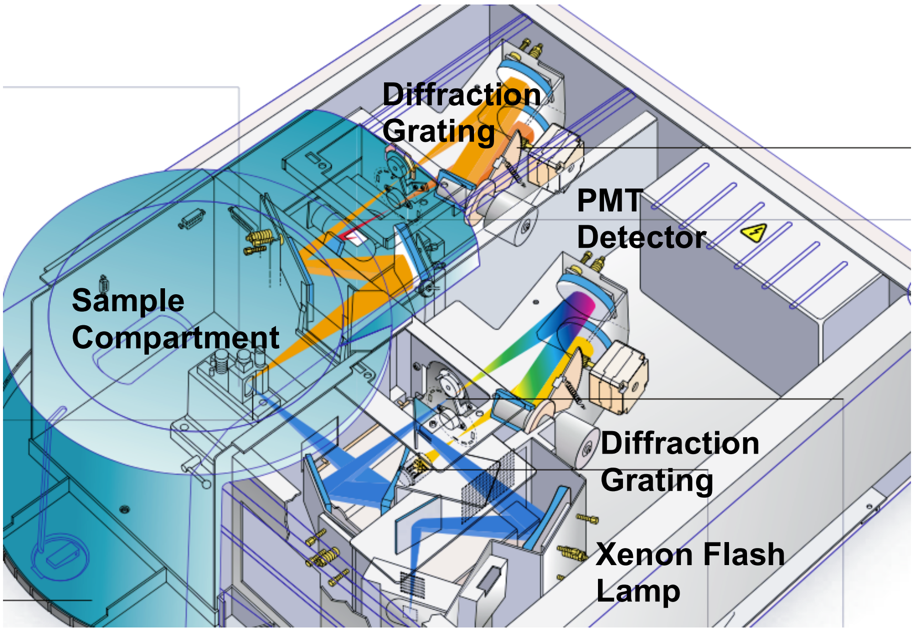

Figure 3.44: *Construction of the Varian Cary Eclipse fluorescence spectrophotometer* ***[44]***.

This system was used to measure the excitation spectra from 220 to 500 nm of the different transitions of the sample under investigation at room temperature. The excitation spectra are determined by changing the excitation wavelength and measuring the intensity of the resulting emission peaks a function of excitation wavelength. This system was also used to measure the decay profiles with an excitation of 325 nm of the different transitions of the samples under investigation at room temperature. Decay profiles were obtained by pulsing the Xenon lamp and measuring the resulting emission decay. The lifetime data was analysed by using the FAST (Advanced Analysis of Fluorescence Kinetics) program as explained in the Results and Discussion chapter.

3.3 Ultraviolet-visible spectroscopy

In this study, the Perkin Elmer Lambda 950 UV-VIS spectrometer was used to measure the optical band gap of the sample under investigation. This apparatus is used to study the transmittance or the absorption of a sample but due to the solid nature of the sample it was setup in such a manner to obtain the diffused reflectance spectrum. This was done by scanning radiation from ultraviolet to visible light onto the sample and a reference sample and then measuring the resulting relative change in the amount of light reflected from both surfaces. In this system, Barium Sulfate is used as a standard reference sample because of its high reflectivity over a wide wavelength region [45]. In this study, the diffused reflectance spectra of the sample under investigation were measured from 300 to 620 nm at room temperature.

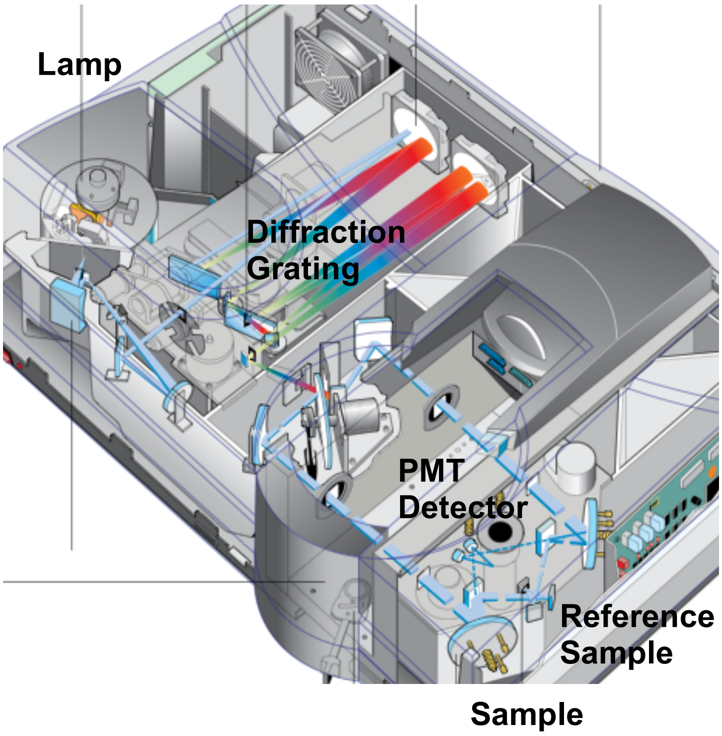

Figure 3.45: *Construction of the Perkin Elmer Lambda 950 UV-VIS spectrometer* ***[46]***.

The principle of this technique is that light with a long wavelength will probably be reflected from the sample, while light with a sufficient short wavelength will have enough energy to excite valence band electrons to the conduction band. This will cause the relative intensity of the reflected light to decrease due to absorbance of the light by the material. By manipulating the obtained spectrum, the energy difference between valence and conduction of the material is determined as explained in the Results and Discussion chapter [47].

3.4 X-ray diffraction

This technique was used to study the crystal structure of the material under investigation. This technique utilises monochromatic x-rays, with a wavelength the same order of magnitude as the inter-atomic distances of the crystal under investigation, which is radiated towards the surface of the material. As seen in Figure 3.46 the lattice planes cause constructive interference to occur and this effect is studied by measuring the intensity of the diffracted x-rays as a function of the angle of diffraction.

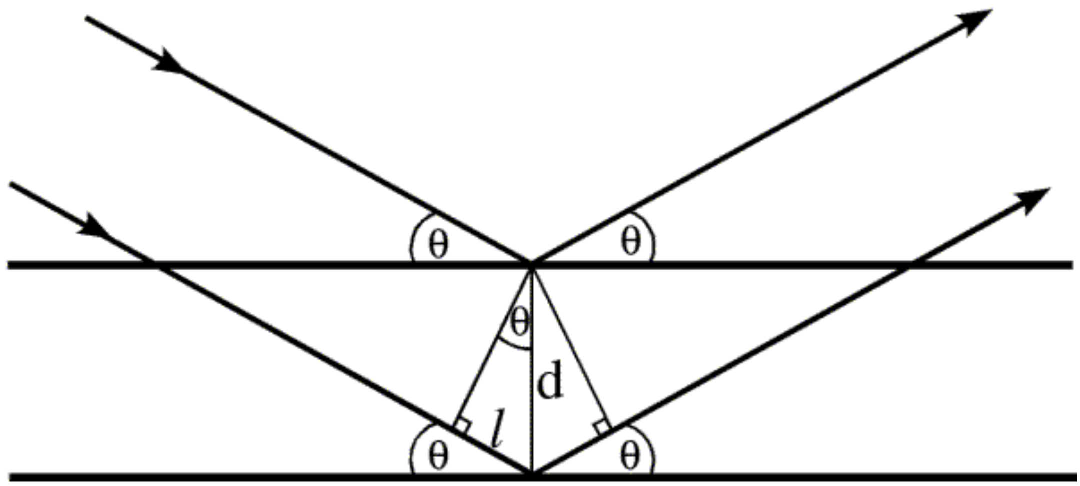

Figure 3.46: *Basic diffraction process described by Bragg's law* ***[68]***.

The angle θ at which constructive interference occur is described by Braggs Law, as shown in the following equation:

$$\sin\theta = \frac{n\lambda}{2d_{hkl}} \qquad \textbf{\textit{3.12}}$$

where n is a positive integer, λ is the wavelength of the x-rays and d_{hkl} is the inter-planar distance of the lattice planes which is given for hexagonal crystal structures by Equation 2.23. By obtaining this information the crystal structure and lattice parameters of the material was determined. By using the Williamson-Hall plot the diffraction spectrum of a material can also provide information of the strain and crystallite size of the material, as explained in a later section. This technique also gives information on crystal lattice deformations that are present along the diffraction vector [48]. In this study, the D8 Advanced AXS GmbH X-ray Diffractometer was used for the diffraction spectrum measurements.

3.4.1 Generating x-rays and the angle analyser

The x-rays used for this technique are generated inside a cathode ray tube. This is done by accelerating high energy electrons onto a Cu target which cause the excitation of the inner shell electrons of the target atoms. When these excited electrons relax, energy is released in the form of radiation of different energies as shown in the spectrum in Figure 3.47. This spectrum consists of several radiation peaks, labelled as $K\alpha$ and $K\beta$, on top of a broad background known as Bremsstrahlung. $K\alpha$ radiation consists of two peaks namely $K\alpha_1$ and $K\alpha_2$ where the former has a shorter wavelength and higher intensity compared to the later. $K\beta$ radiation and Bremsstrahlung is removed from the spectrum with the use of a nickel filter window while the $K\alpha_1$ and $K\alpha_2$ radiation is sufficiently close enough to each other that both wavelengths are used in the technique [49]. The average wavelength of $K\alpha_1$ and $K\alpha_2$ was determined as 1.5296 Å by using the method explained in the next section.

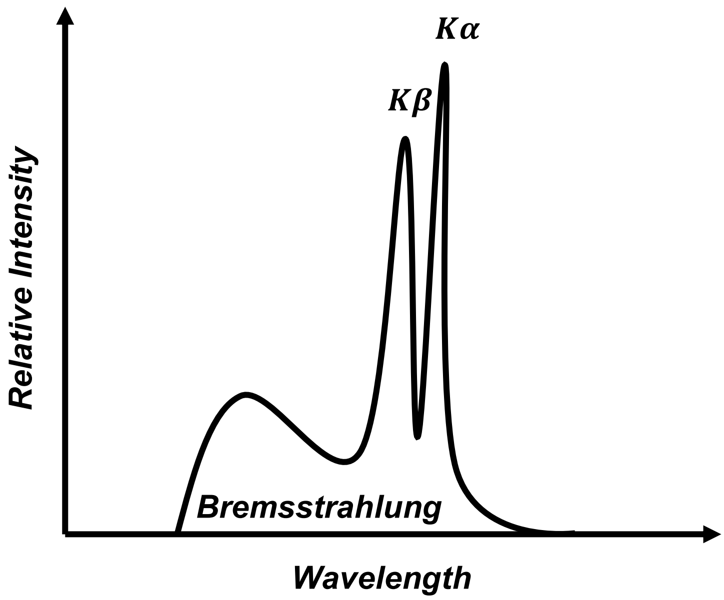

Figure 3.47: *The characteristic x-ray spectrum of a Cu target* ***[67]****.*

While the sample is radiated, the relative intensity of the diffracted x-rays is recorded as a function of angle using an x-ray detector mounted on a goniometer. As shown in Figure 3.46 the incoming and diffracted x-ray beams are both at an angle θ to the sample´s surface. Therefore, XRD spectrums indicates the angle of the recorded diffraction spectrum as 2θ [49]. For this study the XRD spectrums of the samples under investigation, were recorded from 20° to 90° in 0.02° increments.

3.4.2 X-rays wavelength determination

The wavelengths of the x-rays generated by the D8 Advanced AXS GmbH X-ray Diffractometer was determined by using a standard silicon (111) substrate. Silicon has a diamond crystal structure with a unit cell size equal to 5.4309 Å and an inter-planar distance of 3.1355 Å [50]. The two labelled peaks in Figure 3.48 are due to $K\alpha_1$ and $K\alpha_2$ radiation from the x-ray source. The positions of these two peaks were determined as noted in Table 3.2. The difference of the angles of the two peaks is 0.07° which correlates with the theoretical value of 0.07°.

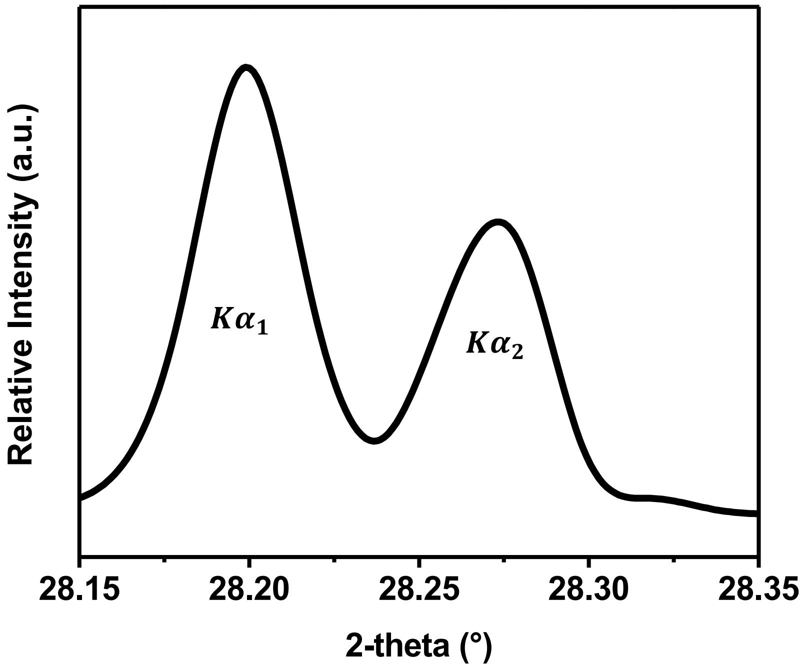

Figure 3.48: *XRD spectrum of silicon (111) substrate.*

By using the values obtained for silicon (111) and Equation 3.12 the wavelengths of $K\alpha_1$ and $K\alpha_2$ radiation were determined for this instrument as shown in Table 3.2. The average of these two values were determined as 1.5296 Å and was used in the calculations as explained in the Results and Discussion chapter. The standard average wavelength of $K\alpha_1$ and $K\alpha_2$ radiation is 1.5425 Å [51]. Compared to the determined wavelength there is an error of 0.84 %. This error could result from fluctuations in the x-ray source or due to an error in the angle analyser´s calibration.

Table 3.2: *Silicon (111) XRD peak parameters.*

Source	**Peak Position (°)**	**Peak FWHM (°)**	**Wavelength (Å)**
$K\alpha_1$	28.20	0.032	1.5277
$K\alpha_2$	28.27	0.034	1.5314
Average	28.235	0.033	1.5296

3.4.3 Strain and crystallite size determination

By using data obtained from the XRD technique, the strain and crystallite size L of the material under investigation was estimated by use of the Williamson-Hall plot, which is described by Equation 3.13.

$$\beta\cos\theta = C\epsilon\sin\theta + \frac{K\lambda}{L} \qquad \textbf{\textit{3.13}}$$

In this equation, θ is the Bragg angle of a specific peak in the XRD spectrum, C is a constant, usually with the value of 4, K represents the crystallite shape and is usually taken to be 0.89 for spherical crystals, λ is the wavelength of the x-rays and β is the FWHM of the specific peak in the XRD spectrum, after subtracting for instrumental line boarding [52]. In the conventional approximation, the width of the pure profile β is extracted from the measured width $\beta_{measured}$ by use of the instrument profile width $\beta_{intrument}$ by using the following equation.

$$\beta^2 = {\beta_{measured}}^2 - {\beta_{intrument}}^2 \qquad \textbf{\textit{3.14}}$$

The value of $\beta_{intrument}$ was determined by calculating the average of the FWHM of the $K\alpha_1$ and $K\alpha_2$ peaks of the silicon (111) XRD spectrum as seen in Figure 3.48. These values were noted in Table 3.2 and the average was used to represent the instrument profile in the calculations that is discussed in the Results and Discussion chapter.

3.5 X-ray photoelectron spectroscopy

The XPS technique is based on the principals of the photoelectric effect, where a material is irradiated with monochromatic soft x-rays which causes the ejection of core level electrons as shown in Figure 3.49. By measuring the kinetic energy of these ejected electrons, information is obtained on the elemental composition and chemical environment of the surface of the material. In this study measurements where obtained with the PHI XPS 5400 system.

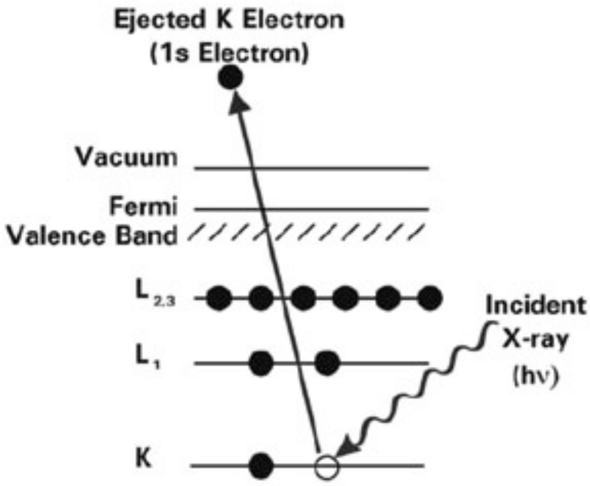

Figure 3.49: Basics of the *XPS process* ***[69]***.

The kinetic energies of the emitted photoelectrons are analysed by an electron spectrometer and the data is shown on a graph of intensity versus electron binding energy. The binding energy is determined by the following equation

$$E_B = E_{hv} - E_k - \theta_A \qquad \textbf{3.15}$$

where E_k is the kinetic energy of the electrons, E_{hv} is the energy of the monochromatic x-rays and θ_A is the spectrometer work function, which is a property of the specific analyser of the system. For the system used in this study the spectrometer work function was given as 3.8 eV [53].

3.5.1 Generating x-rays, electron energy analyser and sputtering

In this system x-rays are generated by accelerating high energy electrons onto an aluminium target. This causes the excitation of the target atoms and when the excited atoms relax energy is released in the form of x-rays as shown in Figure 3.50. These X-rays are then filtered through a thin nickel window to prevent Bremsstrahlung from reaching the sample. The energy of the x-rays generated by this system is 1486.6 eV (Aluminium K_{α}). Figure 3.50 shows the basic components of an XPS system. Most of these components are housed in a stainless-steel chamber equipped with an oil rotation pump, turbo molecular pump and an ion pump in an effort to establish ultra-high vacuum. Throughout measurements the pressure was kept in the order of 10^{-8} Torr.

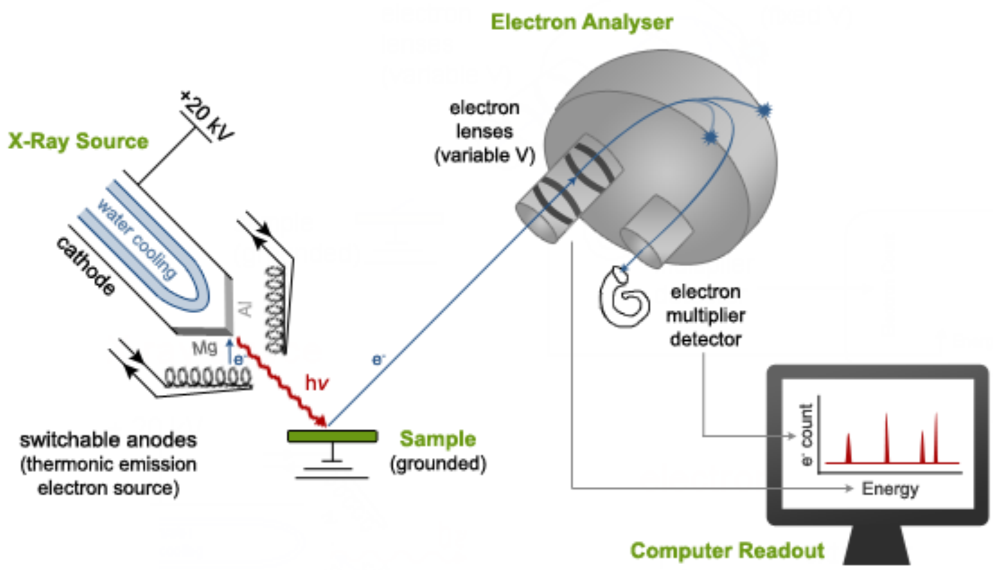

Figure 3.50: *Diagram of the components of an X-ray Photoelectron Spectrometer* ***[65]****.*

When the sample is radiated with the x-rays, electrons from the sample are excited into the vacuum. These electrons are then focused and retarded by an electron lens system with variable voltage into a concentric hemispherical analyser with a fixed angle of 45° to the surface of the sample. In order to keep the absolute resolution of the analyser fixed throughout the energy ranges, the pass energy of the PHI XPS 5400´s analyser was kept constant as 44.75 eV. The electrons that passes through the concentric hemispherical analyser is detected by an electron multiplier detector [53]. By varying the voltage of the electron lens system, electrons with different kinetic energies pass through the concentric hemispherical analyser in order to be detected. Therefore, the kinetic energy of these electrons is determined and by using Equation 3.15 the binding energies of the electrons is determined.

Ion bombardment can be used in order to remove contaminant layers from the surfaces of the samples. This process is referred to as sputtering. In the PHI XPS 5400 system an argon ion sputter gun is used for this function. In this study, in the case where contaminates were proven to be a problem, samples were sputtered for a period of 5 min before analysis. This was done by rastering a 3 kV stable ion beam over an area of 5×5 mm on the sample´s surface. Throughout this process the pressure of the argon gas was set to 10^{-4} Pa while the emission current was kept constant at 25 mA.

3.5.2 Binding energy spectrums

The binding energy of electrons is a unique parameter that is used to qualitatively identify the corresponding elements. Variations in the binding energy of an element is known as chemical shifts and can give a good indication of changes in the chemical environments of the atoms. Quantitative data can be obtained from peak areas and peak heights. The relative peak heights give an indication of the ionization probabilities of the various ionization processes. The p, d and f levels become split upon ionization leading to vacancies in the $p_{1/2}$, $p_{3/2}$, $d_{3/2}$, $d_{5/2}$, $f_{5/2}$ and $f_{7/2}$ levels. The spin-orbit splitting ratio is 1:2 for p levels, 2:3 for d levels and 3:4 for f levels. [53]. The x-rays used in the XPS technique penetrate the sample to a depth of 1 to 10 µm, however only electrons of the first 10 to 100 nm are emitted into the vacuum. The reason for the deeper electrons not escaping is because the deeper electrons have a higher probability to lose their energy through inelastic collision with atoms and defects. However, if an electron is released close to the surface it can escape from the surface with little to no energy loss and can be detected by the electron spectrometer. As seen in Figure 3.51 and Figure 3.52, data that is obtained from the XPS technique is shown as peaks that sit on a background, which rises with a step-like structure with an increase in binding energy. The step-like structure is a result of each successive photoelectron peak on the binding energy scale, adding additional scattered photoelectrons onto the background. In this study, the spectrums for the different samples were measured in 0.125 eV increments with a dwell time of 400 ms. During the deconvolution of the spectra the background was removed by using the Shirley method [54].

3.5.3 Energy scale calibration

It is customary to calibrate the energy scale before measurements. In this study, Cu and gold (Au) standards were used for this procedure. The peaks that were used in the calibration is the Cu $2p_{3/2}$ peak with a standard binding energy of 923.4 eV and the Au $4f_{7/2}$ peak with a standard binding energy of 83.8 eV [53]. Figure 3.51 and Figure 3.52 shows the measured spectrums for both standards. After deconvolution, the peak energies were determined as noted in Table 3.3. With this information, the linearity of the binding energy scale was adjusted in the data acquisitioning program of the PHI XPS 5400.

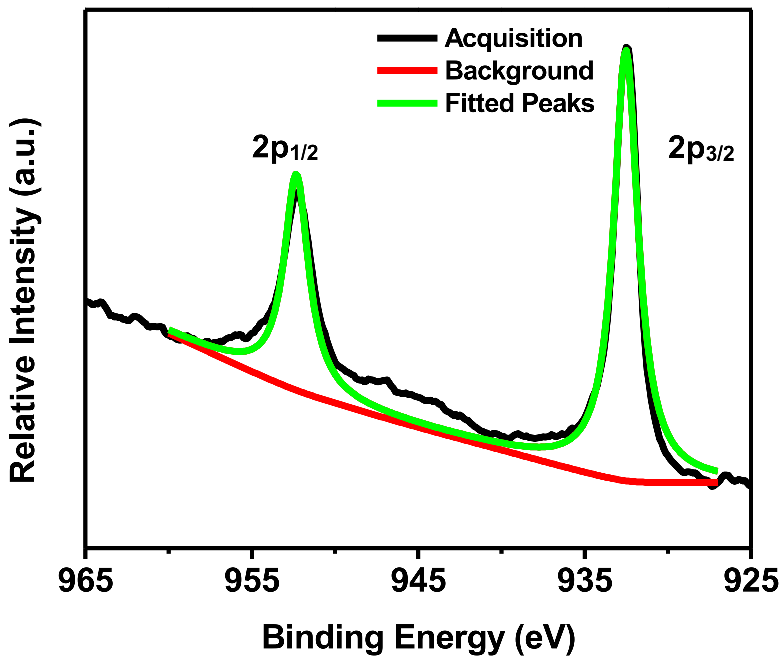

Figure 3.51: *XPS spectrum of Cu standard.*

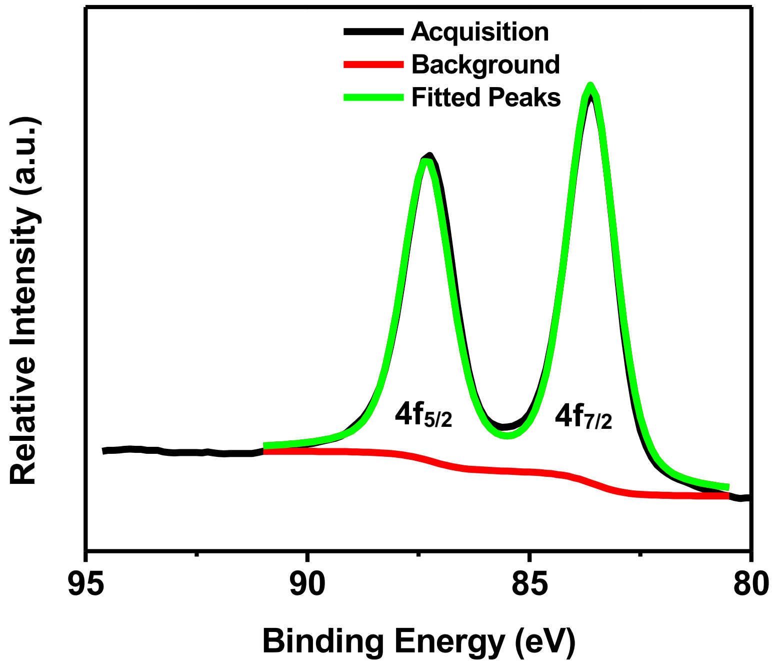

Figure 3.52: *XPS spectrum of Au standard.*

Table 3.3: *Cu and Au peak energies.*

Component	Peak Position (eV)
Cu	
$2p_{1/2}$	952.3
$2p_{3/2}$	923.5
Au	
$4f_{5/2}$	87.3
$4f_{7/2}$	83.6

3.5.4 Charge correction

If the surface of the sample is electrically insulating, then the radiation of the x-rays onto the sample surface can cause a positive charge to accumulate on the surface, due to the ejection of the electrons. This charging-effect cause an increase in the binding energy of the entire sample. Therefore, this effect causes the peaks in the binding energy spectrum to shift to higher binding energy values [55]. In an effort to compensate for this effect the carbon (C) 1s peak was measured for the sample that was not annealed. Due to different contaminant atoms and molecules bonded to the C atoms, the C 1s peak usually consists of several components and therefore deconvolution is necessary as seen in Figure 3.53. The exact energy positions of these components in respect to each other were kept constant during fitting and the FWHM was kept between 1.7 and 2.0 eV as seen in Figure 3.53. The C-C chemical bond has a known electron binding energy of 284.8 eV. The measured value however is 287.6 eV as seen in Table 3.4 [22]. This deviation is due to charging and to correct for this effect, all the measured spectrums where shifted 2.8 eV downward during the data analysis process.

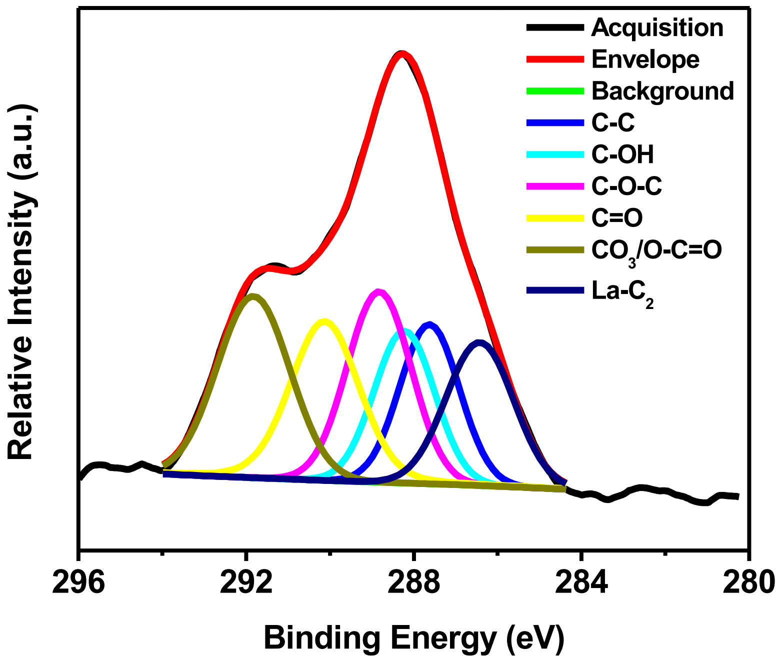

Figure 3.53: *C 1s XPS spectrum of sample that was not annealed.*

Table 3.4: *C 1s peak parameters of sample that was not annealed.*

Chemical Component	Peak Position (eV)	FWHM (eV)	Relative Area
C-C	287.6	1.7	1205
C-OH	288.2	1.7	1164
C-O-C	288.8	1.8	1543
C=O	290.1	1.9	1474
CO_3/O-C=O	291.8	2.0	1671
La-C_2	286.4	1.9	1228

4. Results and Discussion

This chapter aims to discuss the optical, structural and chemical properties of the commercial lanthanum oxysulphide doped with europium(III) (La_2O_2S:Eu(III)) phosphor material that was measured utilising the different techniques as explained in the Experimental Techniques and Methodology chapter. The data analysis that were done to determine the different physical parameters are also discussed and the results are interpreted and compared to theoretical values that were determined in previous experimental and computational studies as explained in the Theory and Literature Review chapter.

4.1 Optical properties

4.1.1 Optical band gap

The optical band gap of a material can experimentally be estimated by obtaining the diffused reflectance spectrum. The Perkin Elmer Lambda 950 UV-VIS spectrometer was used to measure the diffused reflectance spectrum of La_2O_2S:Eu(III) at room temperature and is shown in Figure 4.1.

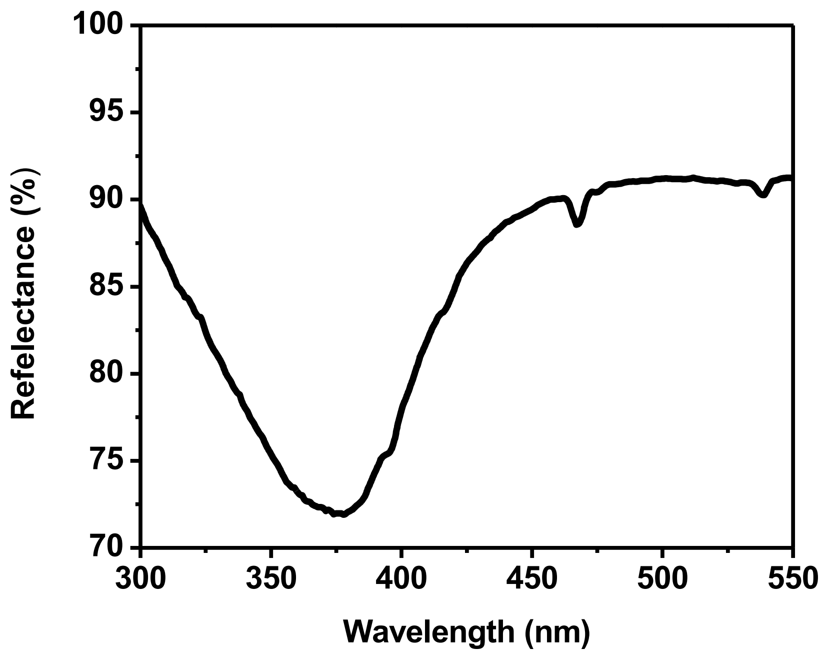

Figure 4.1: *Diffused reflectance spectrum La_2O_2S:Eu(III).*

The obtained spectrum was converted to the Tauc plot, shown in Figure 4.2, by using Equation 2.21 and Equation 2.22. The obtained spectrum was converted to the Tauc plot, shown in Figure 4.2, by using Equation 2.21 and Equation 2.22. This material has multiple absorption peaks, where the weaker and sharper absorption peaks that are observed in the lower energy region, belong to the intrinsic f-f transitions of the Eu(III) ion [56]. The stronger and broader absorption peak is due to absorption to the conduction band. The optical band gap between the valence and conduction band was determined from the absorption edge by drawing a tangent line to the point of inflection of the curve. The point of inflection is the point at maximum value of the first derivative of the curve, which was in this case determined to be at 3.11 eV. The value of the band gap was estimated at the point of intersection of this tangent line with the horizontal axis as shown in Figure 4.2.

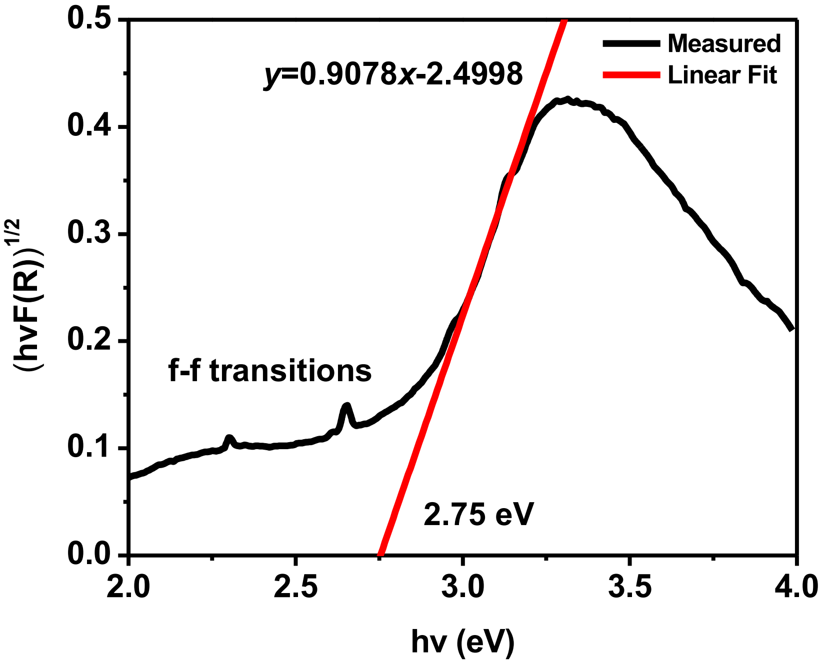

Figure 4.2: *Tauc plot to determine the optical band gap of La_2O_2S:Eu(III).*

With this method, the indirect optical band gap was estimated as 2.75 eV. This is smaller than the value literature suggests of 2.91 eV for the La_2O_2S host material [17]. A possible reason for this results from the doping of the Eu(III) ions that cause an overlapping of the wave functions of the electrons bounded to the dopants. This overlap causes the energies to form an energy band rather than discrete energy levels that leads to a decrease in the band gap [57].

4.1.2 Charge transfer bands

The charge transfer band structure of La_2O_2S:Eu(III) phosphor material was studied by measuring the excitation spectra for the different excited levels of the Eu(III) ion. This was done by utilising the Varian Cary Eclipse fluorescence spectrophotometer to monitor the intensity of the different emission peaks as a function of excitation wavelength at room temperature as shown in Figure 4.3. The broad peaks located at 275 nm and 340 nm is associated with the transitions of the O(II) → Eu(III) and S(II) → Eu(III) charge transfer bands respectively. The S(II) → Eu(III) charge transfer band is at longer wavelengths than the O(II) → Eu(III) charge transfer band due to the higher covalence of the S(II) - Eu(III) bond compared to the O(II) - Eu(III) bond. The higher covalence results from the lower electronegativity of the S(II) ion compared to that of the O(II) ion that enables an easier electron transfer to the Eu(III) ion. According to literature the electronegativity of the S(II) ion and the O(II) ion is 3.44 (Paulings) and 2.58 (Paulings) respectively [56].

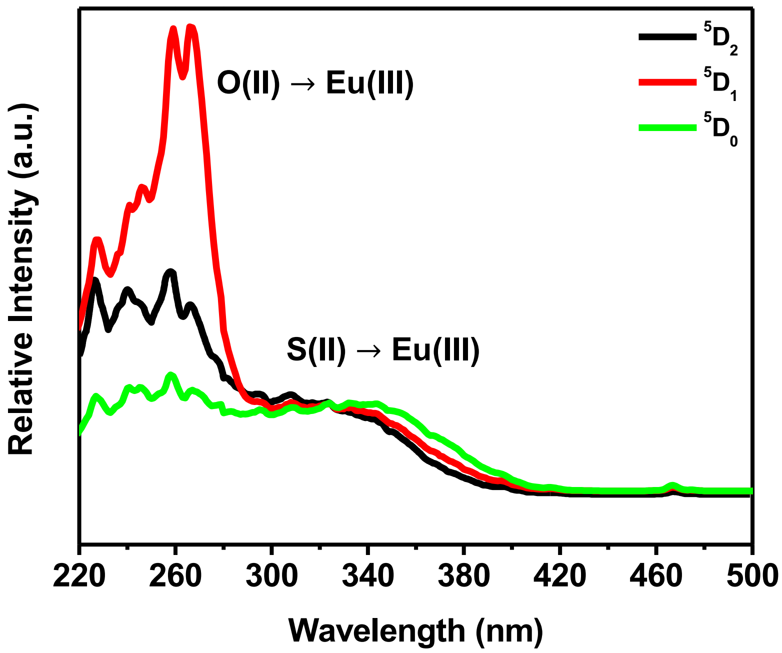

Figure 4.3: *Excitation spectra for different excited levels of La_2O_2S:Eu(III).*

From Figure 4.3 it can be determined that when using an excitation source of 325 nm, the S(II) → Eu(III) charge transfer band is responsible for the transfer of the electrons. This charge transfer band allow the excited electrons to move to the different excited states of the Eu(III) ion, from where the electrons can return to the ground state by possibly releasing their energy in the form of light that is observed as luminescence.

4.1.3 Emission of luminescence

Figure 4.4 shows the emission spectra of La_2O_2S:Eu(III) phosphor material measured at room temperature by the modified PL system. The sharp emission is due the narrow transitions from different ^5D_J excited states to the ^7F_J ground states of the Eu(III) ion as shown in Figure 2.11. Emission from the $^5D_3$ excited state was not observed, probably because emission from this state is totally thermally quenched at room temperature as predicted in Figure 2.13 [23]. Emission from the $^5D_2$ excited state was however observed at the 512 nm region, as labelled in Figure 4.4 [58]. This emission is weak, probably because emission from this state was partially quenched at room temperature. The emission lines from the $^5D_1$ state was observed at the 537, 555 and 585 nm regions as labelled in Figure 4.4 [3]. The emission from these states is still bright at room temperature as predicted by the thermal quenching model. Emission lines from the $^5D_0$ state were observed at 581, 593, 624 and 704 nm regions as labelled in Figure 4.4 [3]. The emission from these sates is still bright at room temperature as predicted.

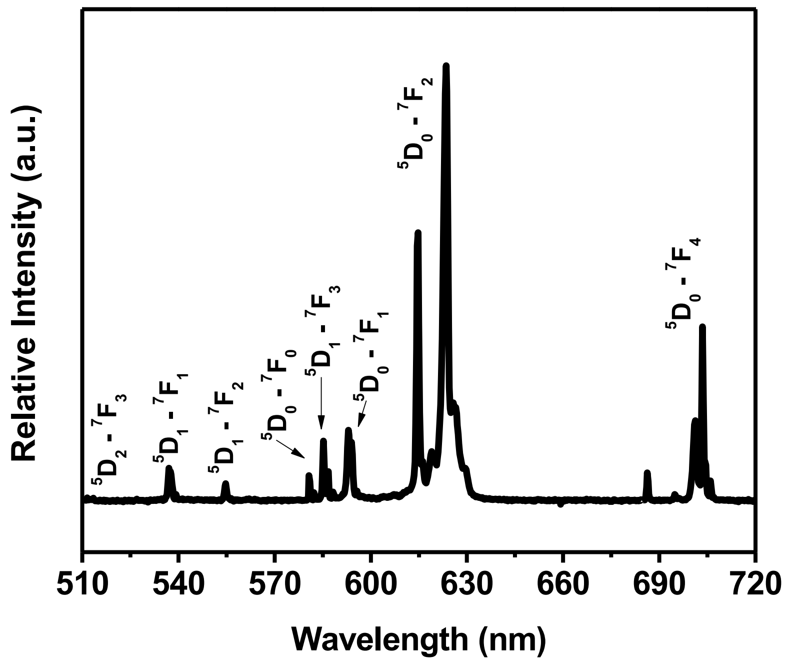

***Figure 4.4**: Emission spectra of La_2O_2S:*Eu(III) *with 325 nm excitation.*

According to the ΔJ selection rules of Judd-Oleft theory the $^5D_0 \rightarrow ^7F_0$ transition is forbidden. However, this transition is clearly observed in Figure 4.4. The reason for this can be either due to strong crystal-field perturbation that causes mixing of the different terms with the different J values, or due to mixing of the low energy charge transfer states into the wave functions of the $4f^6$ configuration [23]. The visually observed colour of this phosphor under excitation is bright vivid red which is mainly due to the strong $^5D_0 \rightarrow ^7F_2$ transition. This intense transition occurs when the Eu(III) ions replace some of the La(III) ions of the host material and therefore inherit the point symmetry of the La(III) ions in the crystal structure. According to Judd-Ofelt parity law the low site symmetry of the Eu(III) ion allows the forced electric dipole $^5D_0 \rightarrow ^7F_2$ transition to appear much stronger than the magnetic dipole $^5D_0 \rightarrow ^7F_1$ transition [23]. The $^5D_0 \rightarrow ^7F_3$ transition is not observed in the spectrum, because it is not allowed according to Judd-Ofelt theory [23].

In Figure 4.4 it is observed that the spaces between the different $^5D_{0,1} \rightarrow ^7F_J$ transitions increase with an increase in J value. This phenomenon is explained by the fact that the splitting of the ^7F_J multiplet corresponds to the Landé interval rule, which states that the interval between successive energy levels is directly proportional to the larger of the total angular momentum value of J [23]. Emission from the excited states to the $^7F_5$ and $^7F_6$ levels was not observed, because this emission occurs in the infrared region which is outside the range of detection of the PMT detector. Figure 4.4 also shows that some of the emission regions, like the $^5D_0 \rightarrow ^7F_2$ transition, consist of several peaks. These peaks result due to the formation of sublevels caused by crystal-field splitting, as illustrated in Figure 2.11. The splitting of the crystal field level is influenced by the symmetry class of the lattice. Therefore, by studying these fine structures of the emission spectrum, the symmetry class of the host lattice can be estimated. For example, in Figure 4.4 the $^5D_0 \rightarrow ^7F_1$ transition is split into two peaks which according to theory is characteristic of hexagonal, tetragonal or trigonal crystal fields. By XRD it was confirmed that the host lattice has a hexagonal structure [23]. For simplicity, the splitting of the peaks was ignored during data analysis by either studying only the main peak or taking the average of the peaks associated with the specific transition.

4.1.4 Lifetime of luminescence

Decay measurements of the different transitions of the La_2O_2S:Eu(III) phosphor material were obtained at room temperature using the Varian Cary Eclipse fluorescence spectrophotometer. Shown in Figure 4.5 are examples of the decay measurements for transitions originating from the different excited states. From inspection, it is observed that the overall emission decay is less than 100 ms after termination of the excitation source, therefore the La_2O_2S:Eu(III) phosphor material displays properties of fluorescence. A variation in the decay time for the different transitions is also observed, with the decay time decreasing the higher the excited state the transition is originating from.

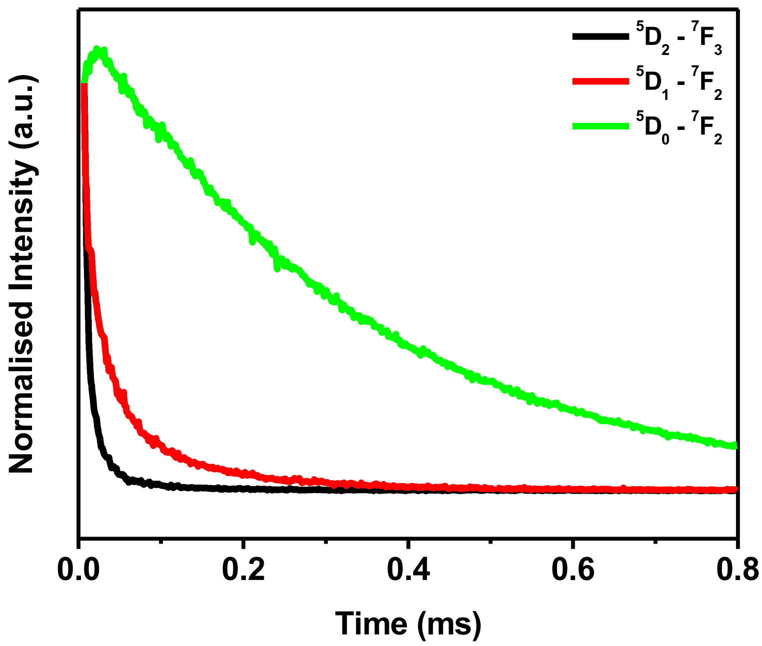

Figure 4.5: *Luminescence intensity decay for the different transitions of La_2O_2S:Eu(III).*

As explained in the Theory and Literature Review chapter, luminescence intensity during the decay process is represented by Equation 2.8. After mathematical manipulation, this expression can also be written as Equation 2.9. The natural logarithm of the data from Figure 4.5 was plotted against time as shown in Figure 4.6. As seen in Figure 4.5 the emission originating from the $^5D_0$ excited state is proven to be increasing directly after termination of the excitation source before decaying. This increase could be due to population of electrons that occur from the higher excited states to the $^5D_0$ excited state [59]. Emission originating from the $^5D_0$ excited state was however treated as a single exponential decay proses. Figure 4.6 shows that the transitions originating from the $^5D_2$ and $^5D_1$ excited states has a double exponential decay. By using Equation 2.10 the FAST (Advanced Analysis of Fluorescence Kinetics) program was able to determine the emission decay constants for the different components τ_1 and τ_2 of each transition [60]. The resulting decay constants for the different transitions is noted in Table 4.1 Equation 2.12 was used to estimate the average emission decay constant $\langle\tau\rangle$ for each transition as noted in Table 4.1.

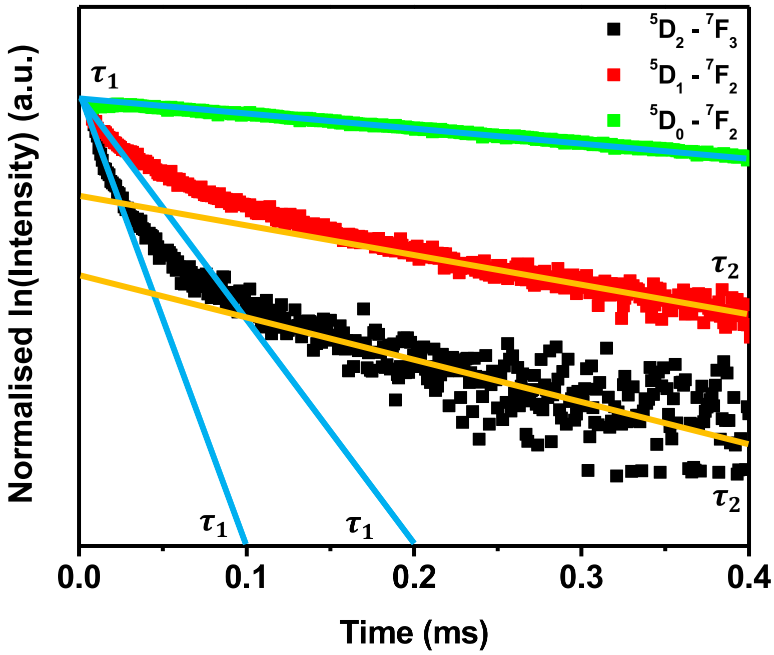

Figure 4.6: *Determination of emission decay constants for the different transitions of La_2O_2S:Eu(III).*

From Table 4.1 it is observed that the component labelled τ_1 has a short emission decay constant while the component labelled τ_2 has a longer emission decay constant. Literature indicates that in nano-sized phosphor materials τ_1 is the emission decay constant of the conventional emission from the rare earth ions while τ_2 is the emission decay constant that results from the emission from rare earth ions that are in the vicinity of a defect or impurity group. These defect or impurity groups capture the electrons and release them after some time resulting in the longer decay constant τ_2. In the case of the La_2O_2S:Eu(III) phosphor material, the presence of defect or impurity groups can be due to the hydroxide groups that forms when the material is exposed to water vapour in the atmosphere at room temperature [20]. It can be seen in Figure 4.6 that the decay curve of the emission originating from the $^5D_2$ excited state has a low signal-to-noise ratio. This is due to the low emission intensity for this transition at room temperature. The average emission decay constant for the emission originating from the $^5D_2$ excited state is also very short and the convolution of multiple emission sources is likely enhanced by the pulsed excitation source [61]. This could be the case since the excitation pulse of this system have a FWHM of 2 μs that is within a factor of 5 of the average emission decay constant which is 10 μs for this transition [43]. In Table 4.1 it is observed that the average emission decay constants of the transitions from the higher excited states of the Eu(III) ion, is significantly shorter than those from the lower excited states. The reason for this is due to the lower activation energies of the higher excited states that cause an increase in the non-radiative transition probability as described by Equation 2.19. In return, the lower non-radiative transition probability causes a shortening in the average emission decay constant as described by Equation 2.17 [62].

Table 4.1: *Lifetime of luminescence results for different transitions of La_2O_2S:Eu(III).*

Transition	**Wavelength (nm)**	τ_1 **(ms)**	τ_2 **(ms)**	$\langle\tau\rangle$ **(ms)**
$^5D_2$-$^7F_3$	512	0.01	0.03	0.01
$^5D_1$-$^7F_1$	537	0.02	0.11	0.08
$^5D_1$-$^7F_2$	555	0.02	0.11	0.08
$^5D_0$-$^7F_0$	581	0.03	0.25	0.20
$^5D_1$-$^7F_3$	585	0.03	0.22	0.17
$^5D_0$-$^7F_1$	593	0.33	-	0.33
$^5D_0$-$^7F_2$	624	0.34	-	0.34
$^5D_0$-$^7F_4$	704	0.34	-	0.34

By comparing the average emission decay constants of the different emission peaks, the identity of some of the different transitions could be confirmed. According to literature the transitions from $^5D_2$ excited state has an average decay constant ten times shorter than the average decay constant of the transitions from the $^5D_1$ excited state, which confirms these measurements [4]. The decay constants for the transitions from $^5D_0$ excited state is also in accordance with a previously reported value of 0.3 ms [56]. The decay constants from the $^5D_0$-$^7F_0$ and $^5D_1$-$^7F_3$ show to be respectively shorter and longer compared to transitions from the same levels. This is due to an overlap of the emission peaks from both the $^5D_0$ and $^5D_1$ excited states [59].

4.1.5 Thermal quenching

The effect of thermal quenching, as discussed in detail in the Theory and Literature Review chapter, was studied for the different transitions of the La_2O_2S:Eu(III) phosphor material by utilising the modified PL system. The programming that was done was used to change the temperature and record spectra of the La_2O_2S:Eu(III) phosphor material automatically. Similar results are expected for the transitions from the different excited states and therefore they are discussed in groups. To preserve a good signal-to-noise ratio the emission from the different excited levels were also measured in groups by measuring the emission spectra in specific wavelength ranges. Measurements for each group were also taken from the onset temperature for the thermal quenching process for each excited state, as given in Table 2.4.

$^5D_2$ excited state

Due to thermal quenching, the emission from the $^5D_2$ excited state at room temperature is weak compared to the emission from the other excited states as seen in Figure 4.4. However, by increasing the PMT voltage and slits width, the emission spectra of the $^5D_2 \rightarrow {}^7F_3$ transition could be measured with a good signal-to-noise ratio, as seen in Figure 4.7. By using the custom-built temperature controller unit, the sample was heated from 30 to 140 °C and an emission spectrum were measured at every 10 °C interval. For temperatures above 140 °C the emission intensity became too low for a proper measurement. The temperature of each spectrum was taken as the average of all the temperature values measured throughout the measurement of each spectrum. The emission spectra measured at four temperatures are shown in Figure 4.7.

It was observed that the emission of this transition consists of several peaks caused by the formation of sublevels as illustrated in Figure 2.11 that in return results from the crystal-field splitting. The intensity for this emission was determined for each temperature by determining the area under the peak from 511 to 512 nm. The area was used instead of the peak height to ensure a high signal-to-noise ratio. The emission intensity as a function of temperature is shown in Figure 4.8. The obtained data was plotted in the form of Equation 2.27 as shown in Figure 4.9. A linear fit was done through the data as seen in Figure 4.9. The slope and y intercept of this line were used to determine both the activation energy and pre-exponential constant of the excited state respectively, by using Equation 2.27.

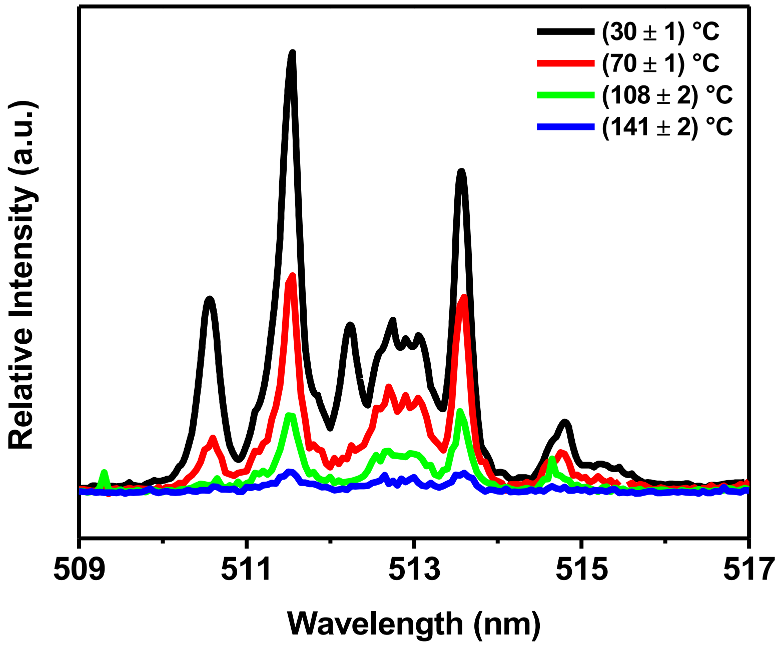

Figure 4.7: *Emission spectra of the transition from the* $^5D_2$ *excited state at different temperatures.*

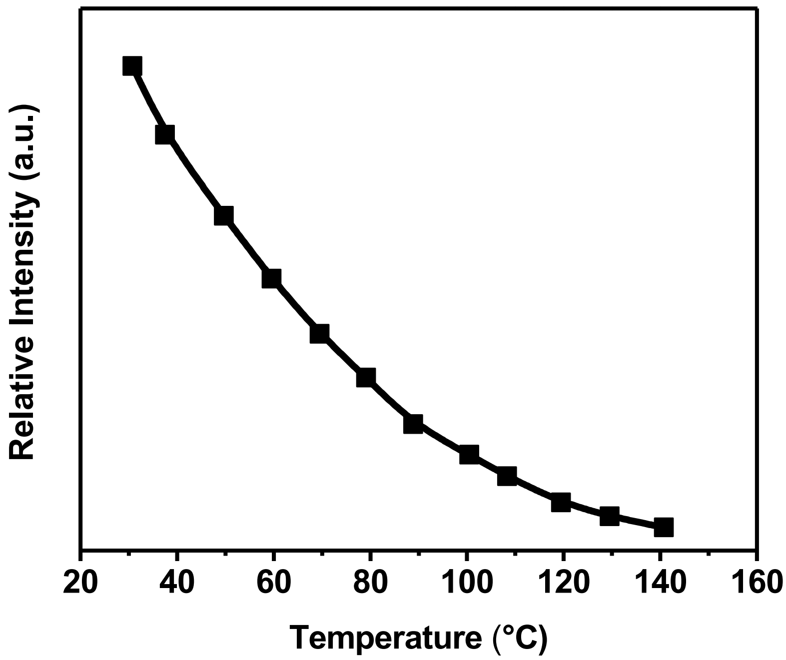

Figure 4.8: *Emission intensity of the* $^5D_2 \rightarrow {}^7F_3$ *transition at different temperatures.*

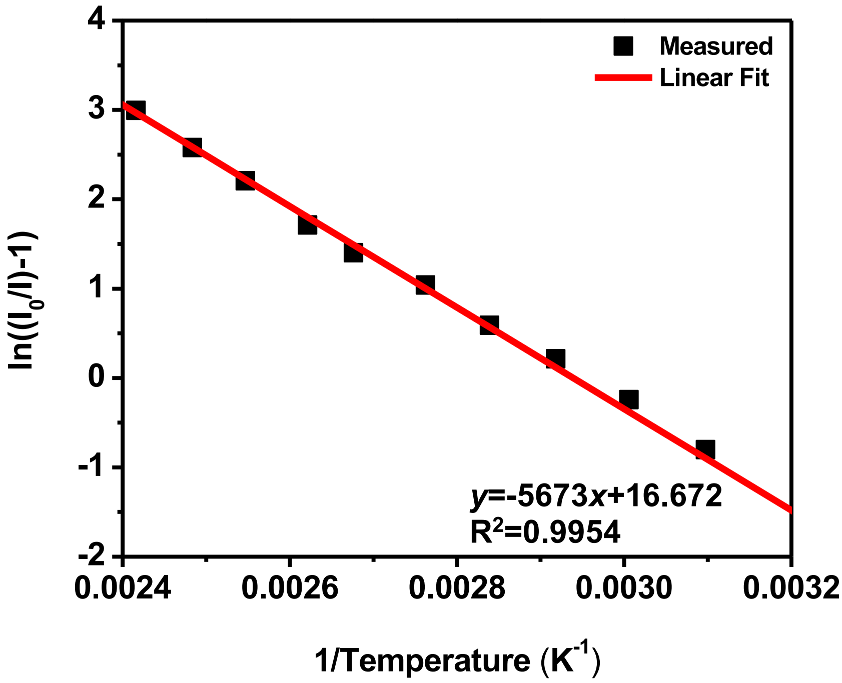

Figure 4.9: *Determination of the activation energy and pre-exponential constant for the thermal quenching process of the* $^5D_2 \rightarrow ^7F_3$ *transition.*

The activation energy for the thermal quenching process of the level $^5D_2$ excited level was determined as E_2= 0.49 eV. This value is larger than the value of E_2=0.37 eV that was measured in a previous study [3]. The pre-exponential constant was determined as G = 1.6×10^7 s^{-1} which is lower than the value previously measured of G = 3.2×10^7 s^{-1} in the same study [3]. The accuracy of these values can possibly be increased by measuring emission spectra below room temperature, however it is not currently possible on this modified system.

$^5D_1$ excited state

The activation energy for thermal quenching and pre-exponential constant of the $^5D_1$ excited state were determined using the same process as for the $^5D_2$ excited state. The necessary data was obtained by measuring the emission spectra of the different transitions originating at the $^5D_1$ excited state, at every 10 °C interval between 90 to 230 °C as shown in and Figure 4.11.

The obtained data was plotted in the form of Equation 2.27 as shown in Figure 4.12 and the calculated values are shown in Table 4.2 for all the transitions.

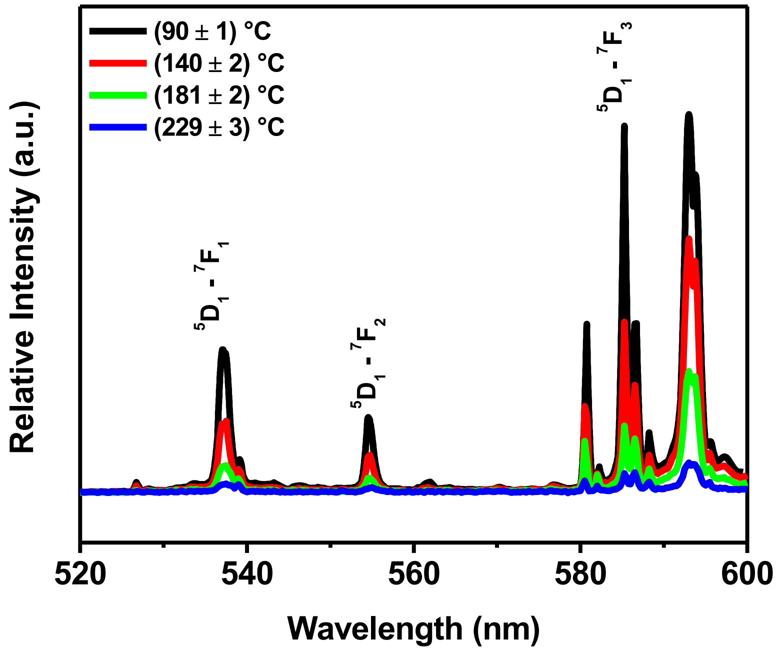

Figure 4.10: *Emission spectra of transitions from the $^5D_1$ excited state at different temperatures.*

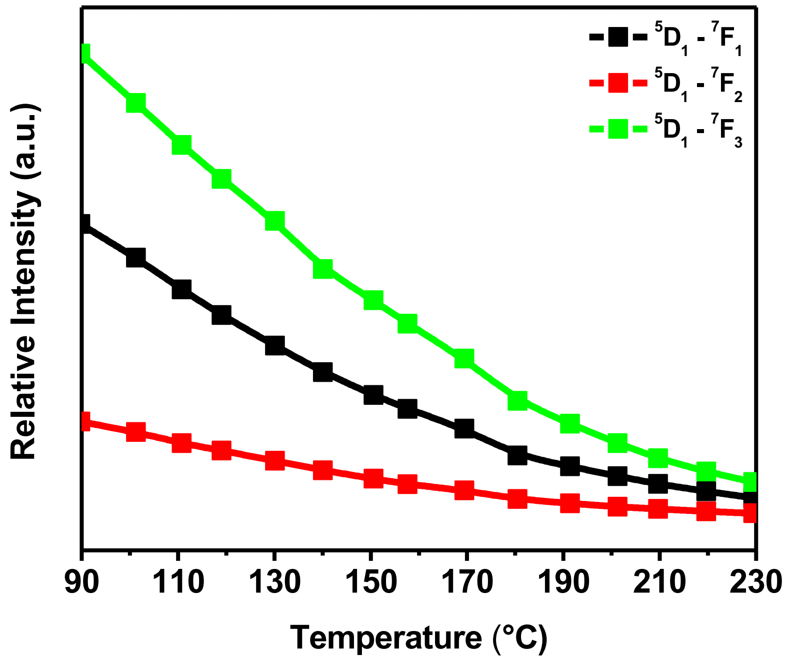

Figure 4.11: *Emission intensity of the $^5D_1$ transitions at different temperatures.*

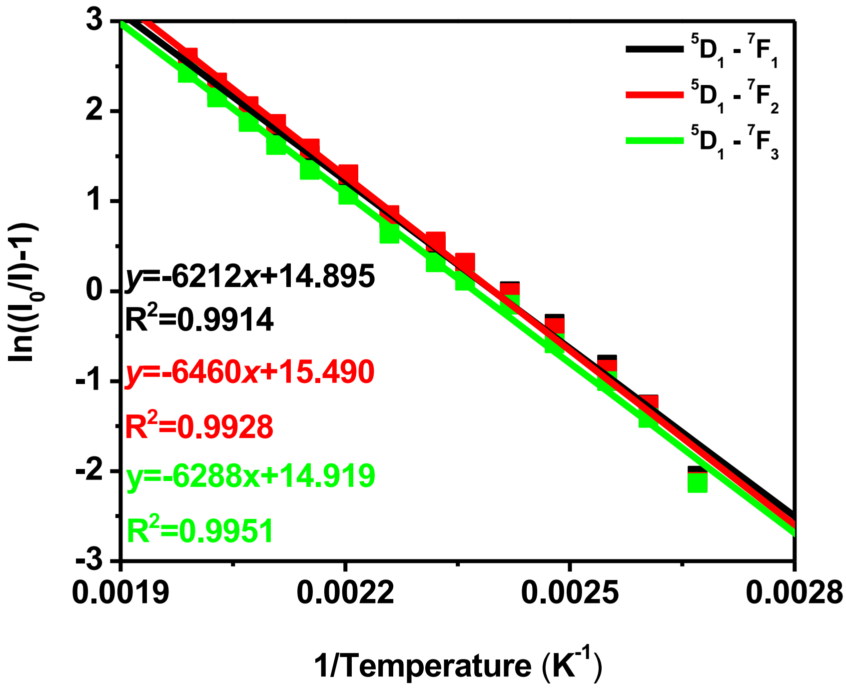

Figure 4.12: *Determination of activation energy and pre-exponential constant for the thermal quenching process of the $^5D_1$ transitions.*

Table 4.2: *Results of the determination of activation energy and pre-exponential constant for the thermal quenching process of the transitions from the $^5D_1$ excited state.*

Transitions	**E_1 (eV)**	**G (s^{-1})**
$^5D_1$-$^7F_1$	0.54	3.2×10^6
$^5D_1$-$^7F_2$	0.56	5.0×10^6
$^5D_1$-$^7F_3$	0.54	3.2×10^6

The average activation energy for thermal quenching for emission originating from the $^5D_1$ excited state was determined from the data in Table 4.2 as E_1= 0.55 eV. This value is smaller than the value of E_1=0.62 eV that was measured in a previous study, however it is still in range [3]. The average pre-exponential constant was determined as G = 3.8×10^6 s^{-1} which is lower than the value previously measured of G = 3.2×10^7 s^{-1} [3].

$^5D_0$ excited state

The activation energy for thermal quenching and pre-exponential constant of the $^5D_0$ excited state were initially determined by using the same process as for the $^5D_2$ and $^5D_1$ excited states. The necessary data was obtained by measuring the emission spectra of the different transitions originating at the $^5D_0$ excited state from 180 to 330 °C measured in 10 °C intervals, as shown in Figure 4.13 and Figure 4.14. The emission data from the $^5D_0 \rightarrow ^7F_0$ was ignored, because it could not successfully be deconvoluted from the emission of the $^5D_1 \rightarrow ^7F_3$ as the lifetime data in Table 4.1 also suggested. The obtained data was plotted in the form of Equation 2.27 as shown in Figure 4.15 and the calculated values are shown in Table 4.3. The average activation energy for thermal quenching of the $^5D_0$ excited state was determined as E_0= 1.24 eV from the data in Table 4.2. This value does not agree with the value of E_0= 0.78 eV that was measured in a previous study. The average pre-exponential constant was determined as G = 1.3×10^{13} s^{-1} which is higher than the value previously measured as G = 3.2×10^{7} s^{-1} [3].

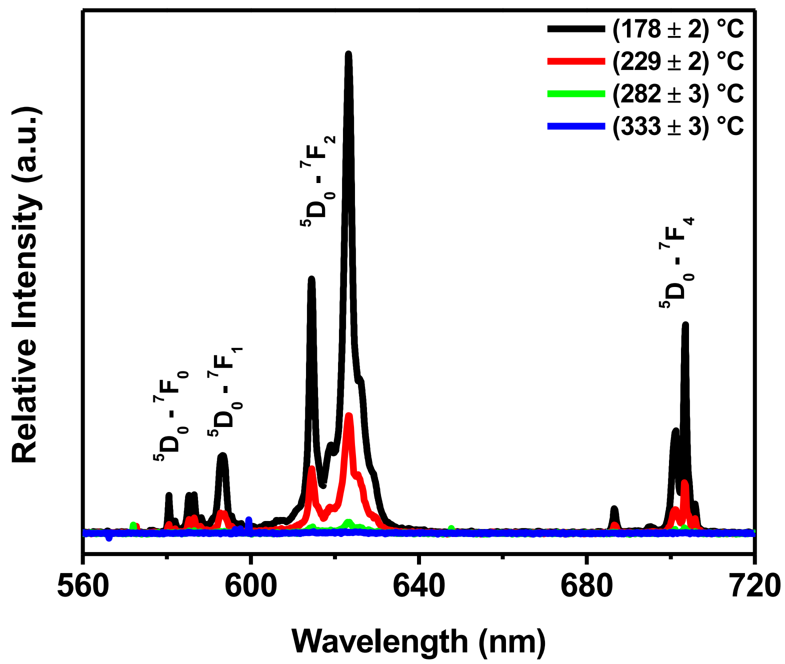

Figure 4.13: *Emission of transitions from the $^5D_0$ excited state at different temperatures.*

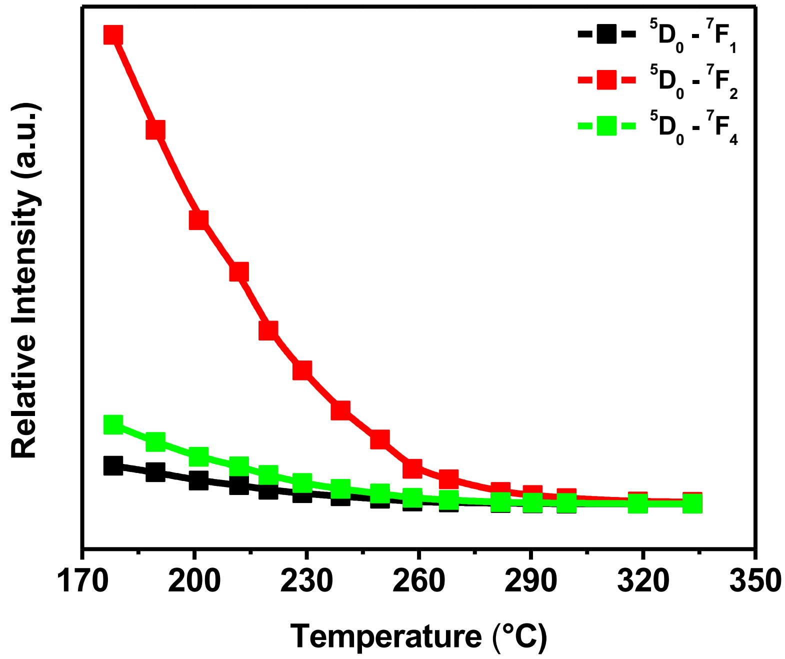

Figure 4.14: *Emission intensity of the $^5D_0$ transitions at different temperatures (small range).*

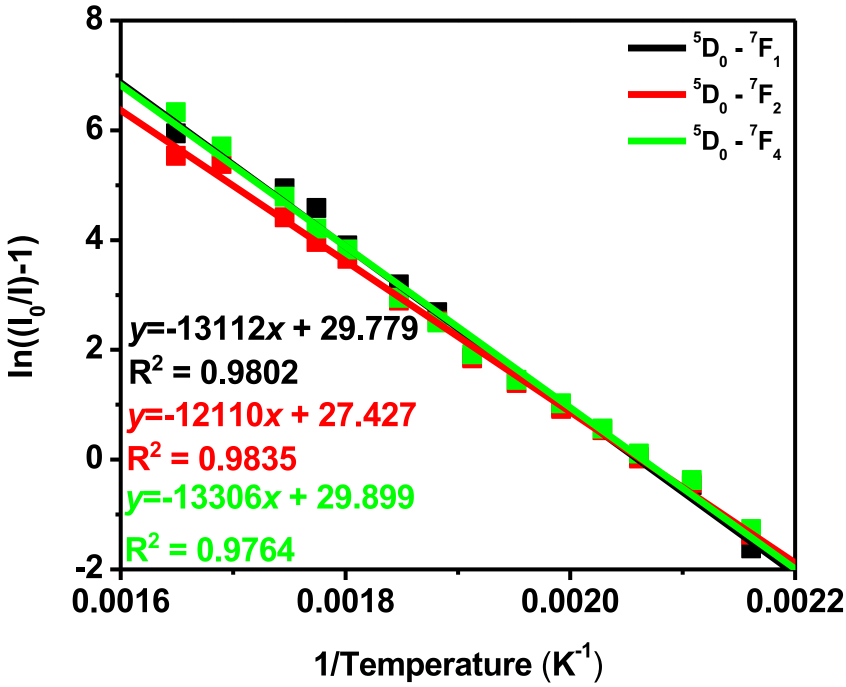

Figure 4.15: *Determination of activation energy and pre-exponential constant for the thermal quenching process of the $^5D_0$ transitions.*

***Table 4.3**: Initial results of the determination of activation energy and pre-exponential constant for the thermal quenching process of the transitions from the $^5D_0$ excited state.*

Transitions	E_0 (eV)	G (s^{-1})
$^5D_0$-$^7F_1$	1.29	2.0×10^{13}
$^5D_0$-$^7F_2$	1.18	2.0×10^{12}
$^5D_0$-$^7F_4$	1.27	1.6×10^{13}

To study the disagreement between the values measured and theoretical values, the emission spectra of the different transitions originating at the $^5D_0$ excited state were measured from 30 to 170 °C in 10 °C intervals. According to the theory of thermal quenching, in this temperature region, the emission from the $^5D_0$ is supposed to stay constant. However, as seen in Figure 4.16 the emission intensity also decreases with an increase in temperature in this temperature range. This data was modelled as a thermal quenching process by plotting the obtained data together with the data obtained at higher temperatures in the form of Equation 2.27 as shown in Figure 4.17. Lastly a linear fit was also obtained for this data as displayed.

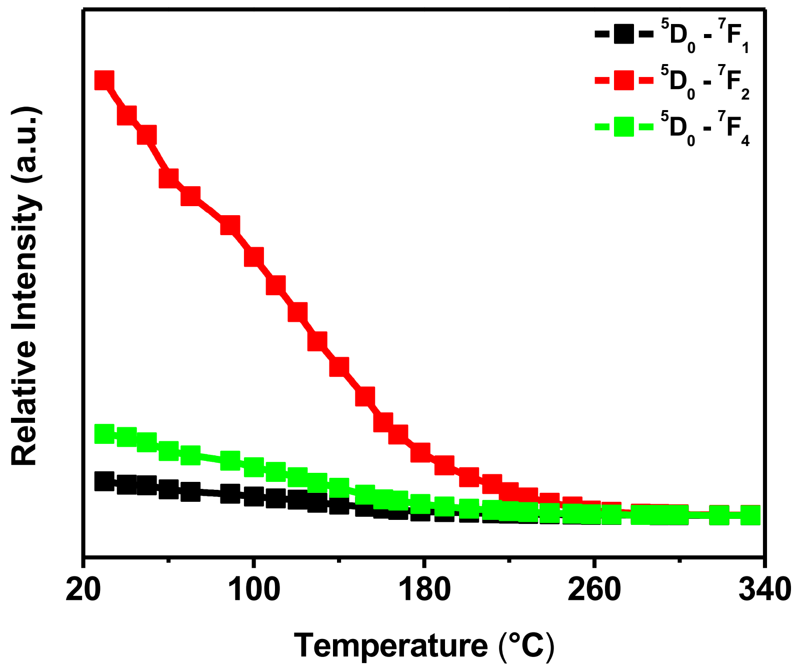

***Figure 4.16:** Emission intensity of the $^5D_0$ transitions at different temperatures (full range).*

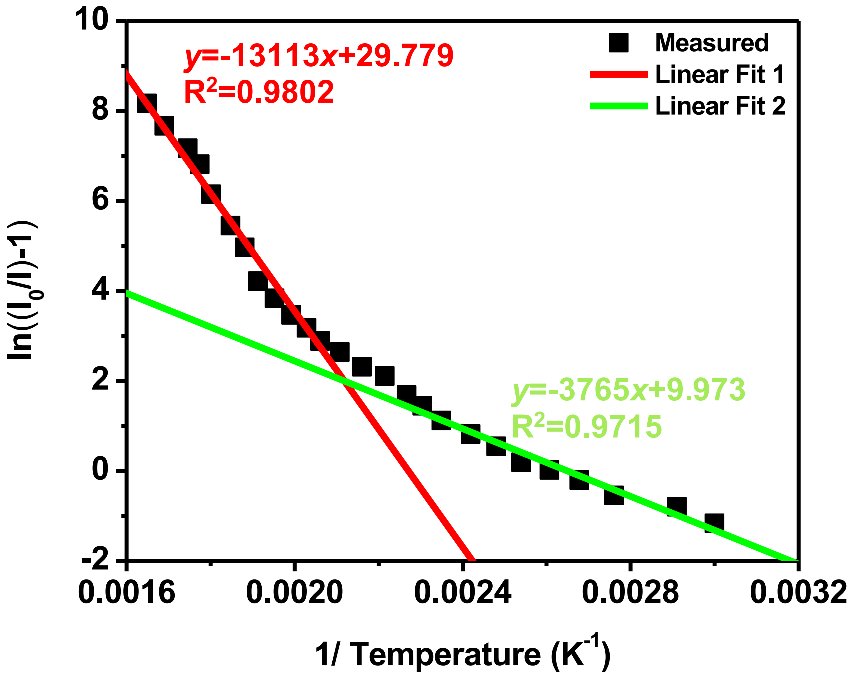

Figure 4.17: *Determination of the final activation energy and pre-exponential constant for the thermal quenching process of the* $^5D_0\rightarrow{}^7F_1$ *transition.*

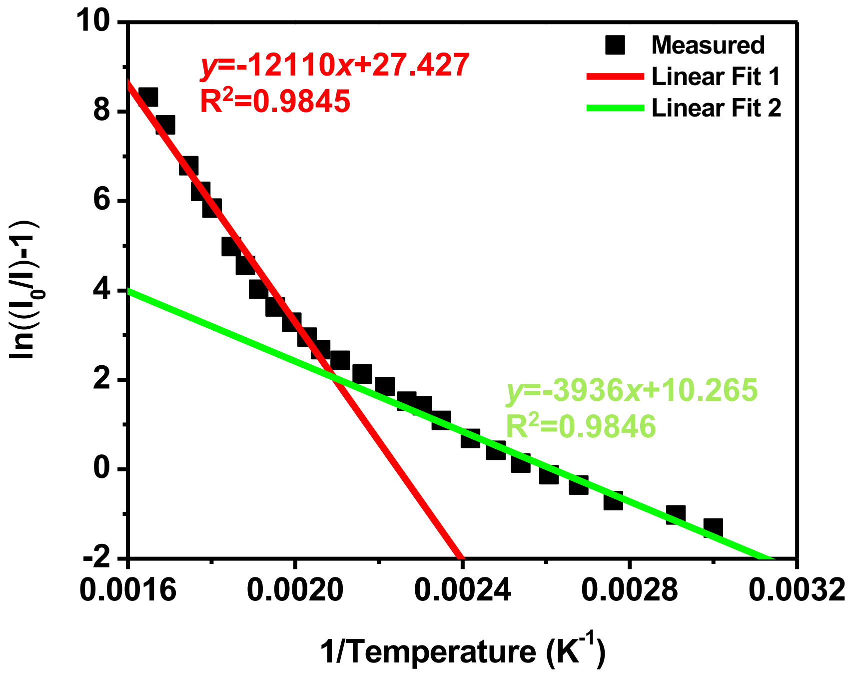

Figure 4.18: *Determination of the final activation energy and pre-exponential constant for the thermal quenching process of the* $^5D_0\rightarrow{}^7F_2$ *transition.*

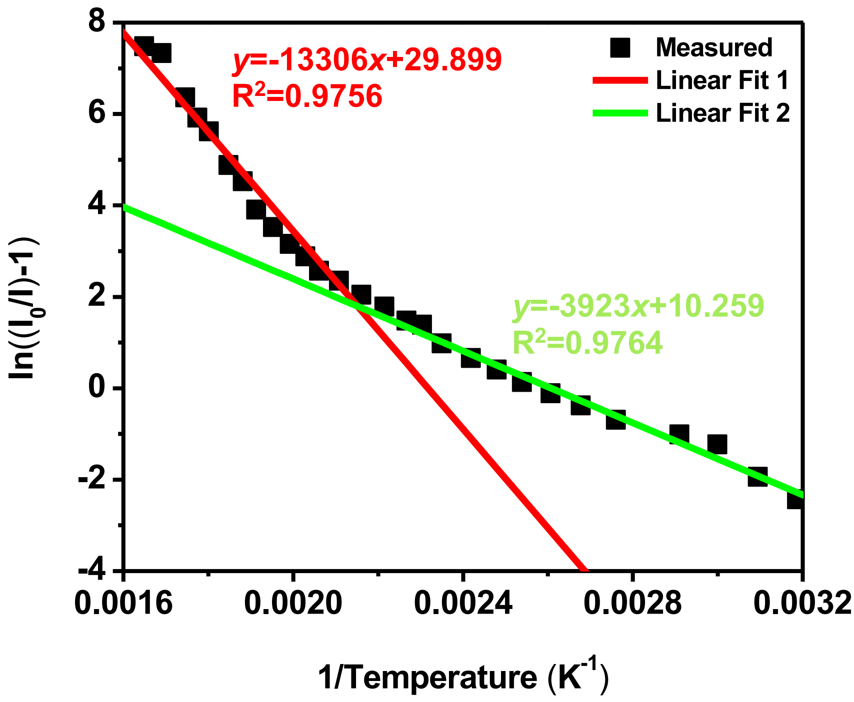

Figure 4.19: *Determination of the final activation energy and pre-exponential constant for the thermal quenching process of the* $^5D_0 \rightarrow ^7F_3$ *transition.*

With the assumption that the process that causes the intensity to decrease at the lower temperature region is still at work at the higher temperature region, this unknown effect was subtracted from the thermal quenching data to isolate the thermal quenching process. As a first order approximation, the average activation energy and the average pre-exponential constant was calculated for the isolated thermal quenching process as E_0=0.77 eV and G = 2.5×10^8 s^{-1} respectively, as shown in Table 4.4. The obtained results correlate well with the values that literature suggests of E_0=0.78 eV for the activation energy and G = 3.2×10^7 s^{-1} for the average pre-exponential constant [3].

Table 4.4: *Final results of the determination of activation energy and pre-exponential constant for the thermal quenching process of the transitions from the* $^5D_0$ *excited state.*

Transitions	**E_0 (eV)**	**G (s^{-1})**
$^5D_0$-$^7F_1$	0.81	4.0×10^8
$^5D_0$-$^7F_2$	0.70	3.2×10^7
$^5D_0$-$^7F_4$	0.81	3.2×10^8

The extent of the unknown effect could not be measured with the same method for the higher excited states, due the fact that measurements below room temperature are not currently possible on this modified system.

4.1.6 Intensity ratio

The modified PL system was used to measure the emission spectra of La_2O_2S:Eu(III) phosphor material from 582 to 598 nm in the temperature range from 70 to 190 °C in 10 °C increments. It was observed that between 80 and 180 °C there is a relative change in the intensity between the emission originating from the $^5D_1$ and $^5D_0$ excited states as shown by the normalised data in Figure 4.20. By calculating the peak areas of the different emission peaks for different temperatures, the ratio of the intensity from the different excited states could be plotted as a function of temperature as shown in Figure 4.21.

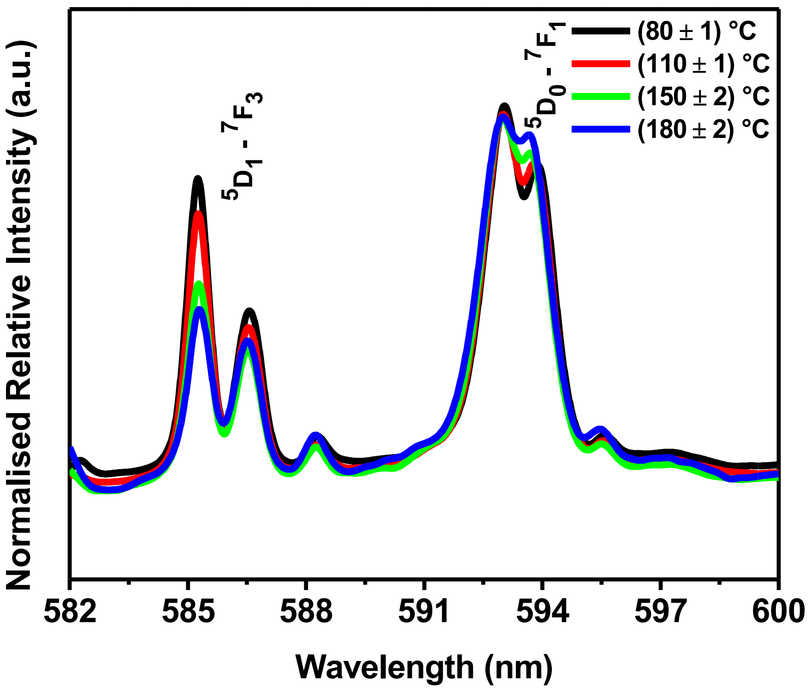

Figure 4.20: *Comparison between emission from the $^5D_1$ and $^5D_0$ excited states at different temperatures.*

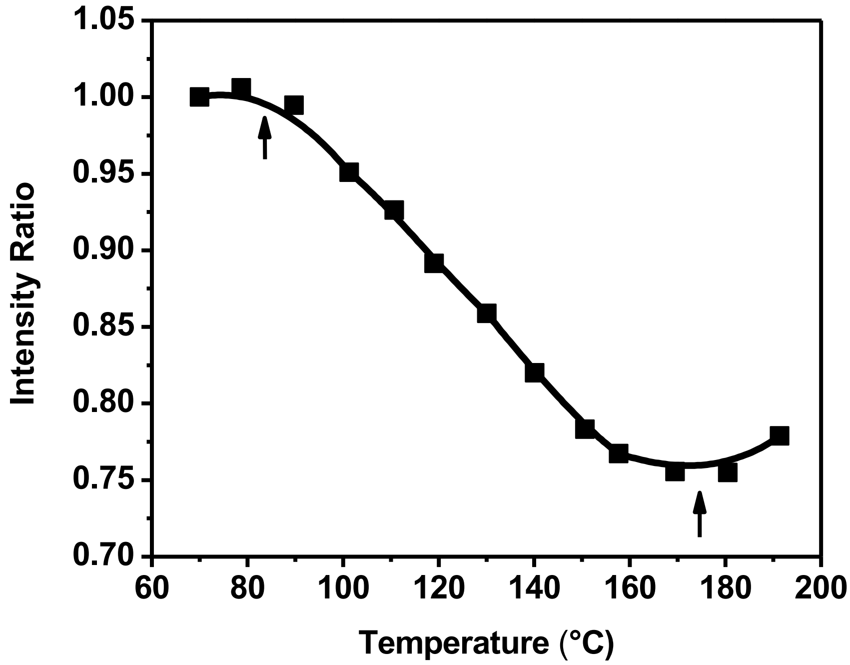

Figure 4.21: *Intensity ratio between $^5D_1$ and $^5D_0$ excited states.*

This observed ratio change as a function of temperature can be explained by the thermal quenching model. In the low temperature region, the electrons from both the $^5D_1$ and $^5D_0$ do not have enough energy to thermally quench and therefore the intensity of both excited states is relatively constant. However, according to theory, at temperatures greater than 83 °C (indicated with arrow on Figure 4.21) the electrons from the $^5D_1$ excited state start to thermally quench which causes the observed emission to decrease while the observed emission from $^5D_0$ is decreased by the unknown process. This causes a relative change in the emission between the two excited states, which is observed in Figure 4.21. According to theory, at temperatures of greater than 175 °C (indicated with arrow on Figure 4.21) the electrons from the $^5D_0$ excited state start to thermally quench and the intensity ratio starts to level out. The ratio of the $^5D_1$ and $^5D_0$ emission lines can possibly be used as calibration data to measure temperature within the range from 80 °C to 180 °C by use of the fluorescence intensity ratio technique as explained in the Theory and Literature Review chapter. However, the temperature to luminescence sensitivity of this specific commercial phosphor material is relatively weak. This is mainly due to the weak emission from the $^5D_1$ excited state.

4.1.7 Luminescence stability

The luminescence stability of this material at high temperatures was tested by using the modified PL system. This was done by utilising the Time Scan Spectrum function that was programmed as explained in the Experimental Techniques and Methodology chapter. The material was annealed at 400 °C while measuring the emission spectra every 30 min for a period of 480 min. As shown in Figure 4.22 the spectral resolution of the spectra is low. The reason for this is the wide slit width that had to be used due to the low emission intensity. This is also due to the large effect of thermal quenching on all the transitions at this temperature. In Figure 4.22 it is observed that the peak positions do not change as a function of annealing time, therefore there are no major structural changes as confirmed in the next section [23]. However, the cumulative intensity of the emission from both the excited states increase over time while kept at a constant temperature of 400 °C. The cause of this increase in luminescence was studied by considering the structural and chemical stability of the host material as explained in the next two sections. The intensity of the emission from both excited states increases proportionally, therefore the temperature sensing capabilities of this material is preserved.

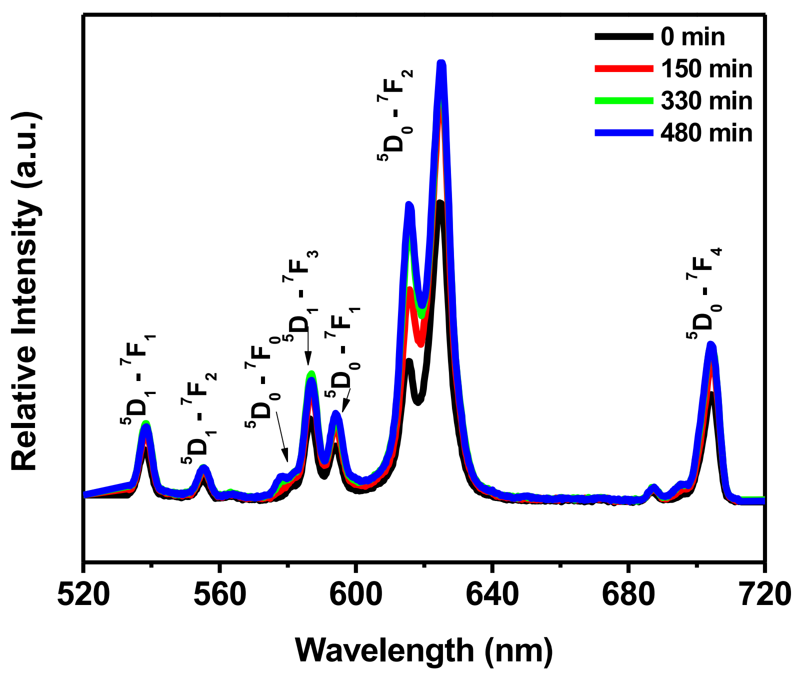

Figure 4.22: *Emission spectra as function of time at (400 ± 4) ℃.*

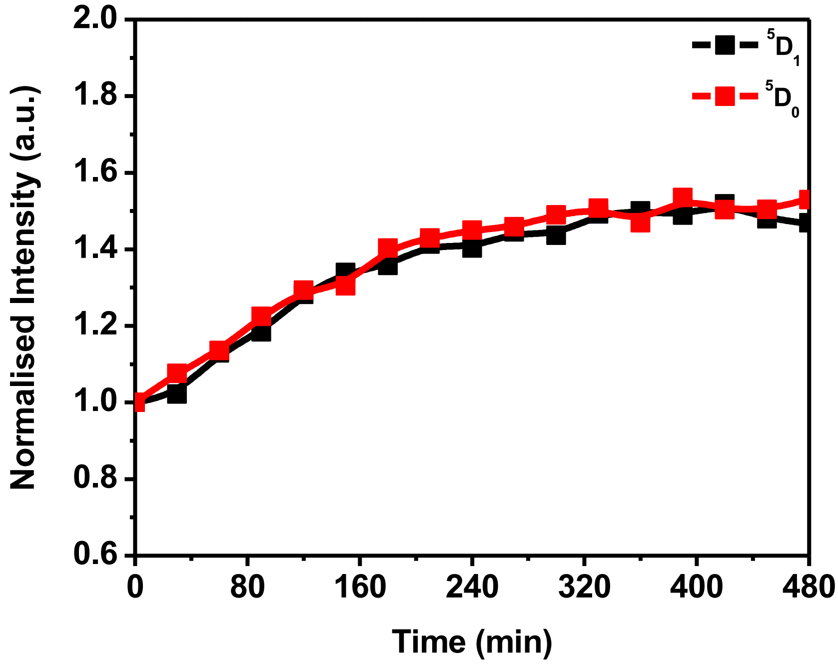

Figure 4.23: *Emission intensity from $^5D_1$ and $^5D_0$ excited states as function of time at 400 ℃.*

4.2 Structural properties

The structural properties of the La_2O_2S:Eu(III) phosphor material as a function of annealing time was studied, by using the XRD technique. This was done by using the temperature controller unit to anneal La_2O_2S:Eu(III) samples at 400 °C for 0 min, 30 min, 60 min, 120 min and 240 min. After these periods of time the samples were cooled to room temperature and placed in the D8 Advanced AXS GmbH X-ray Diffractometer for structural analysis.

4.2.1 Structure

Figure 4.24 shows that there is a good correlation between the measured patterns and the standard data for the hexagonal structure of La_2O_2S (JCPDS-Number 27-0263). The corresponding peaks are labelled with their respective Miller indexes. The peaks marked with * are due to La_2O_3 (JCPDS-Number 05-0602) impurities while those marked with a # are due to $La(OH)_3$ (JCPDS-Number 36-1481) impurities present in the samples. The La_2O_3 impurities are due to O(II) ions which substitute S(II) ions while the $La(OH)_3$ impurities form due to spontanuous reaction with water vapour as explained in the Theory and Literature Review chapter.

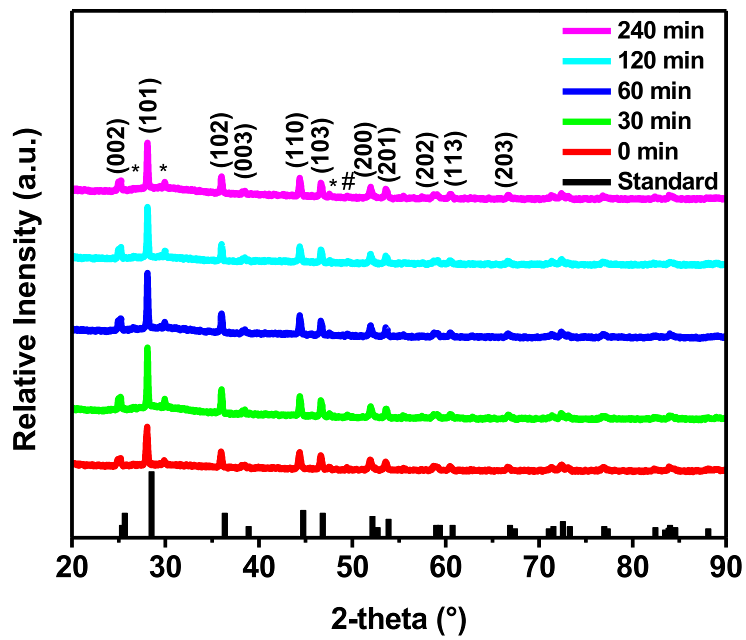

Figure 4.24: *XRD patterns of different samples annealed at 400 °C for different periods.*

From the XRD patterns it is observed that there are no major structural changes as a function of different periods of annealing. By using Equation 3.12 the inter-planar distance of the lattice planes for the different peaks was determined as explained in the Experimental Techniques and Methodology chapter. Equation 2.23 together with the inter-planar distance and corresponding Miller indexes of the (003), (200), (002) and (110) peaks was used to determine the lattice parameters. The averages of the lattice parameters for the samples exposed to different annealing periods are a = 4.04 Å and c = 6.99 Å. These values differ from the values for the standard lattice parameters of a = 4.05 Å and c = 6.94 Å for reasons explained in the next section.

4.2.2 Strain and crystallite size

On closer inspection, it is observed in Figure 4.25 that the (101) peaks of the different samples are shifted to the left compared to that of the standard pattern. This is due to the presence of the Eu(III) dopant ions, impurities and defects that causes an increase in the lattice parameters. However, it is also observed that these peaks shift to the right and narrows as a function of annealing time. This is an indication of a variation in the strain or crystallite size of the samples as impurities or defects are removed.

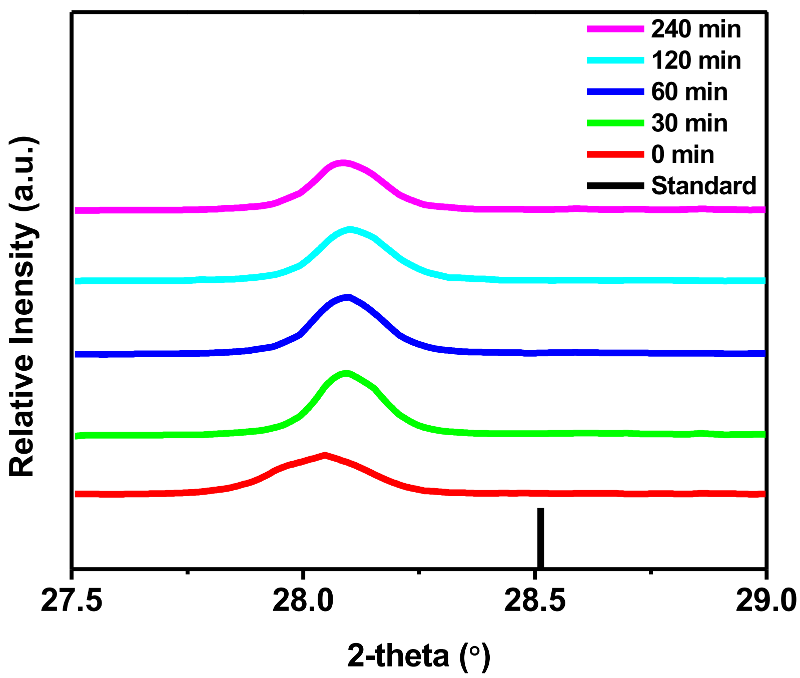

Figure 4.25: *(101) peak of samples after different periods of annealing at 400 ℃.*

To estimate the strain and crystallite size of the different samples the Williamson-Hall plot was used as explained in the Experimental Techniques and Methodology chapter. The FWHMs and positions of the (101), (102), (110), (103), (200) and (201) peaks were determined in order to obtain the plots for the different samples as seen in Figure 4.26. From the incline and y intercept of the linear fit through the data points respectively the strain and crystallite size of the different samples were estimated by using Equation 3.13 and Equation 3.14. The strain and crystallite size for the different samples are noted in Table 4.5.

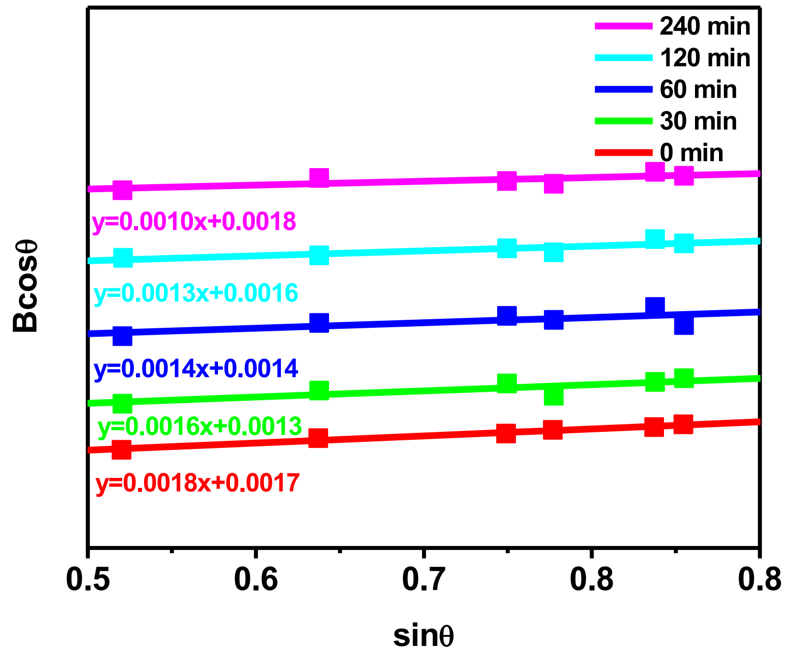

Figure 4.26: *Williamson-Hall plot for different samples annealed at 400 ℃ for different periods.*

In Table 4.5 it is observed that the strain decreases with an increase in the annealing time. However, the crystallite size is observed to stay relatively constant with an average size of 61 nm. The decrease in the strain confirms the removal of defects or impurities in the crystal lattice at high temperatures. To explore this effect in more detail the chemical properties of this material were studied by the XPS technique as explained in the next section.

Table 4.5: *Strain and crystallite size results for different samples annealed at 400 ℃ for different periods.*

Time (min)	**Strain ($\times 10^{-4}$)**	**Crystallite Size (nm)**
0	4.5	57
30	4.0	72
60	3.5	65
120	3.3	59
240	2.5	54

4.3 Chemical properties

The chemical properties of the La_2O_2S:Eu(III) phosphor material as a function of annealing time was studied, by using the XPS technique. This was done by using the temperature controller unit to anneal La_2O_2S:Eu(III) samples at 400 °C for 0 min, 30 min, 60 min, 120 min and 240 min. After these periods of time the samples were cooled to room temperature and placed in the XPS for chemical analysis. Measurements were made of the La $3d_{5/2}$ and O 1s peak regions. Due to the low atomic sensitivity factor of the XPS technique for S(II), the S 2p peak region is weakly observed and therefore the S 2p region was ignored for this study [53]. As a result, it was impossible to accurately quantify the different elements in the commercially produced La_2O_2S:Eu(III) phosphor material.

This work was done with the objective to successfully qualify the relative changes in the different La_2O_2S:Eu(III) samples and relate them with changes in the chemical environment of the La(III) ions. This objective was achieved by performing peak fitting, with as little as possible restriction, on the acquisitioned data. For the annealed samples (30 min, 60 min, 120 min and 240 min) the relative changes in the energy peak positions were considered and not the absolute energy positions. The reason for this is because it was observed that the C 1s peak of the annealed samples underwent a change in the chemistry and therefore this peak could not be used for accurate charge correction. This chemical change can be due to oxidation of the C contaminants during the process of annealing the samples in atmosphere [21].

4.3.1 Lanthanum peaks

Figure 4.27 shows the XPS spectrum for the La $3d_{5/2}$ region for the sample that was not annealed (0 min). After Shirley background subtraction, the La $3d_{5/2}$ peak region was deconvoluted into three components as explained in the Theory and Literature Review chapter [54]. To ensure repeatability it was decided to constrain the FWHMs of the peaks of the three components to 2.7 eV. However, the energy positions and peak areas of the three components were not constrained. The corresponding determined component parameters are shown in Table 4.6.

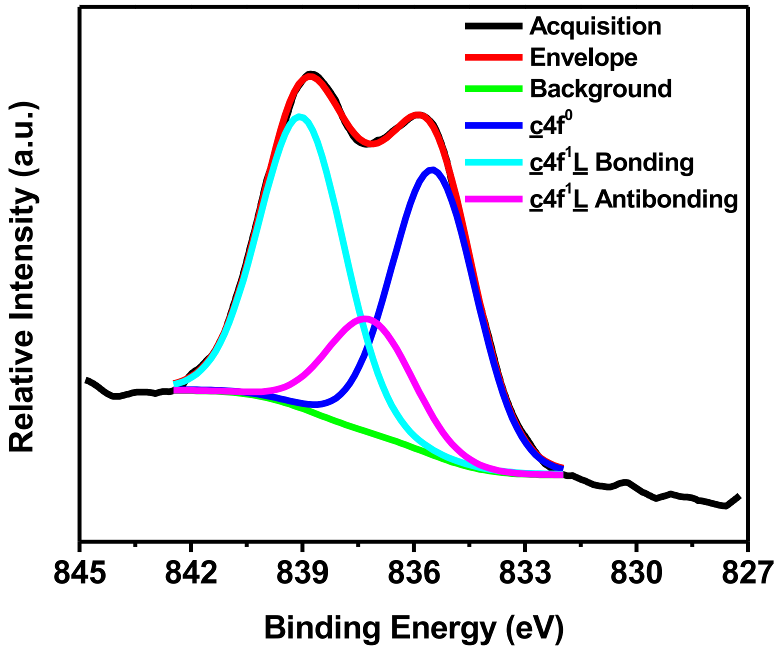

Figure 4.27: *La 3d$_{5/2}$ XPS spectrum of sample that was not annealed (0 min).*

Table 4.6: *La 3d$_{5/2}$ XPS peak parameters of sample that was not annealed (0 min).*

Chemical Component	Position (eV)	Relative Area
$\underline{c}4f^0$	835.4	7959
$\underline{c}4f^1\underline{L}$ Bonding	839.0	8128
$\underline{c}4f^1\underline{L}$ Antibonding	837.1	3080

As seen in Table 4.6 the absolute peak position of the $\underline{c}4f^0$ component correlates well with the value measured in the previous study of 835.1 eV for the $La(OH)_3$ compound [21]. As indicated in Table 4.7 the relative peak positions and relative areas of the peaks of the three components of the sample that was not annealed (0 min), correlates well with the values measured for the $La(OH)_3$ compound (coloured in grey) in the previous study. These values from the previous study were calculated from the absolute peak values that are given in Table 2.2 in the Theory and Literature Review chapter. Figure 4.28 compares the La 3d$_{5/2}$ region of the sample that was not annealed and the sample that was annealed for 240 min. A definite change in the envelope of the region is observed. This change in the envelope indicates a possible change in the chemical environment of the La(III) ion. To explore this effect, the same peak fitting procedures were used for the La $3d_{5/2}$ region of the samples that were annealed (30 min, 60 min, 120 min and 240 min) as shown by the example in Figure 4.29.

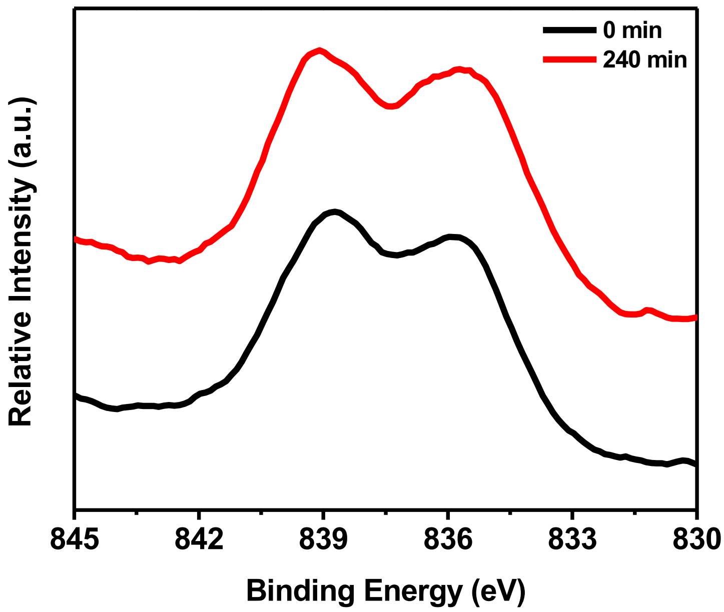

Figure 4.28: *Comparison between La $3d_{5/2}$ peak region of sample not annealed (0 min) and sample annealed for 240 min.*

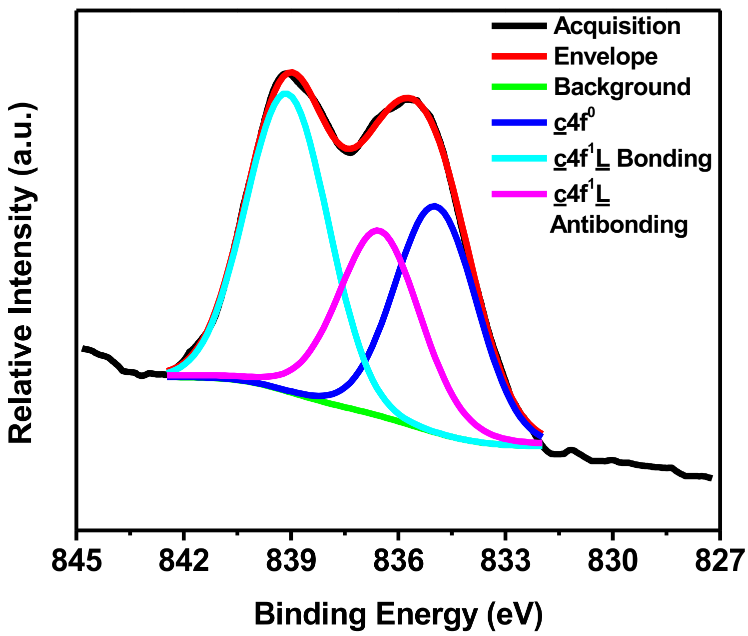

Figure 4.29: *La $3d_{5/2}$ XPS spectrum of sample that was annealed to 400 ℃ for 240 min.*

The obtained relative peak positions and areas, together with the values for the $La(OH)_3$ and La_2O_3 compounds (coloured in grey) measured in the previous study, are listed in Table 4.7 [21]. As seen the relative peak positions of the $\underline{c}4f^1\underline{L}$ Bonding and $\underline{c}4f^1\underline{L}$ Antibonding, with respect to the $\underline{c}4f^0$ peak, shifts as a function of period of annealing. Also, the relative area of the $\underline{c}4f^0$ peak, with respect to the total fit area, quench as a function of period of annealing. Table 4.7 illustrates how the character of the La $3d_{5/2}$ region is changed during the annealing process from that of $La(OH)_3$ to that of La_2O_3 as hydroxide impurities are removed. The removal of some of these impurities during the annealing process, confirm the reduction of the strain in the crystal lattice as proven by the XRD results.

Table 4.7: *Relative changes in La $3d_{5/2}$ XPS peak parameters.*

Time (min)	**Relative position of $\underline{c}4f^1\underline{L}$ Bonding to $\underline{c}4f^0$ (eV)**	**Relative position of $\underline{c}4f^1\underline{L}$ Antibonding to $\underline{c}4f^0$ (eV)**	**Area of $\underline{c}4f^0$ to total fit area (%)**
$La(OH)_3$	3.5	1.7	43
0	3.6	1.7	42
30	3.9	1.7	38
60	4.0	1.7	36
120	4.1	1.4	34
240	4.2	1.6	31
La_2O_3	4.1	0.6	10

4.3.2 Oxygen peaks

Figure 4.27 shows the XPS spectrum for the O 1s region of the sample that was not annealed (0 min). The absolute peak energy is 532.0 eV which correlates with the O 1s peak energy value that literature suggests for $La(OH)_3$ of 531.4 eV [21]. After Shirley background subtraction, the O 1s region was deconvoluted into five components as indicated by Table 2.3. The relative peak positions of these components were constrained by use of the values supplied in Table 2.3, however the absolute peak positions were not constrained [22]. The FWHM were restricted to less than or equal to 2.0 eV. The obtained parameters of the deconvolution, for the O 1s region of the sample that was not annealed (0 min), are shown in Table 4.8.

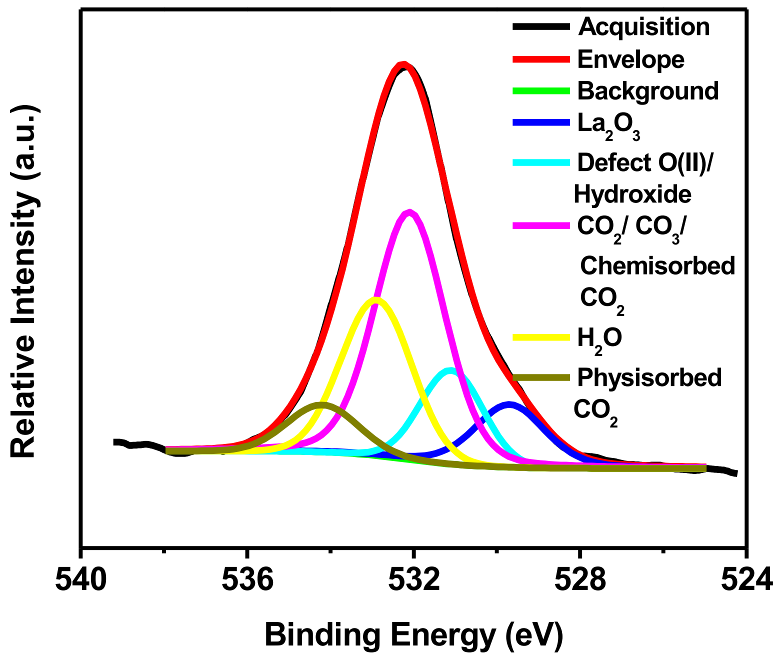

Figure 4.30: *O 1s XPS spectrum of sample that was not annealed (0 min).*

Table 4.8: *O 1s XPS peak parameters of sample that was not annealed (0 min).*

Chemical Component	**Peak Position (eV)**	**FWHM (eV)**	**Relative Area**
La_2O_3	529.5	2.0	1193
Defects O(II)/ Hydroxide	530.9	1.8	2619
CO_2/ CO_3/ Chemisorbed CO_2	531.9	2.0	7660
H_2O	532.7	2.0	3590
Physisorbed CO_2	534.0	2.0	1814

This same peak fitting procedures were followed for the O 1s regions of the samples that were annealed (30 min, 60 min, 120 min and 240 min). From the obtained results, the relative peak areas were calculated for the O(II) defects/ hydroxides component as shown in Table 4.9. As seen in Table 4.9 the relative concentration of O(II) defects/hydroxide decrease with an increase in period of annealing.

Table 4.9: *Comparison of O(II) defects/hydroxides as a function of annealing period.*

Time (min)	**Area of O(II) defects/hydroxide to total fit area (%)**
0	16
30	12
60	13
120	12
240	13

The reason this effect is weakly observed is due to the large CO_2/ CO_3/ Chemisorbed CO_2 component present in the O 1s XPS spectrum, which resulted from contaminants present on the surface of the samples. In order to improve the results of the study of this effect, the contaminants were removed by sputtering the samples with Argon$^+$ ions as explained in the Experimental Techniques and Methodology chapter. Also in an attempt to accelerate this effect a La_2O_2S:Eu(III) sample was annealed at 800 °C for 480 min in atmosphere by using an Udian Annealing Furnace. After this period of time the sample was cooled to room temperature and placed in the XPS for chemical analysis. As seen in Figure 4.31 there is a dramatic change in the O 1s peak region of the different samples, which results in it being difficult to quantitatively analyse the results by means of deconvolution. Therefore, the relative positions of the different components given in Table 4.8 are indicated with numbered arrows as shown in Figure 4.31. Due to the effect of sputtering a relative decrease in the component related to CO_2/ CO_3/ Chemisorbed CO_2 (indicated with arrow 4) is observed for all the samples. The O 1s peak region of the sample annealed at 800 °C for 480 min clearly indicate an extra component present at 528.8 eV (indicated with arrow 1). According to literature this results from the formation of Eu_2O_3 on the surface of the sample due to segregation of Eu(III) ions to the surface of the sample at sufficiently high temperatures [63]. Lastly a relative increase in the host material component (indicated with arrow 2) compared to that of the hydroxide component (indicated with arrow 3) is observed. This confirms the fact that annealing reduces the hydroxide impurities present in the host material of the La_2O_2S:Eu(III) phosphor material.

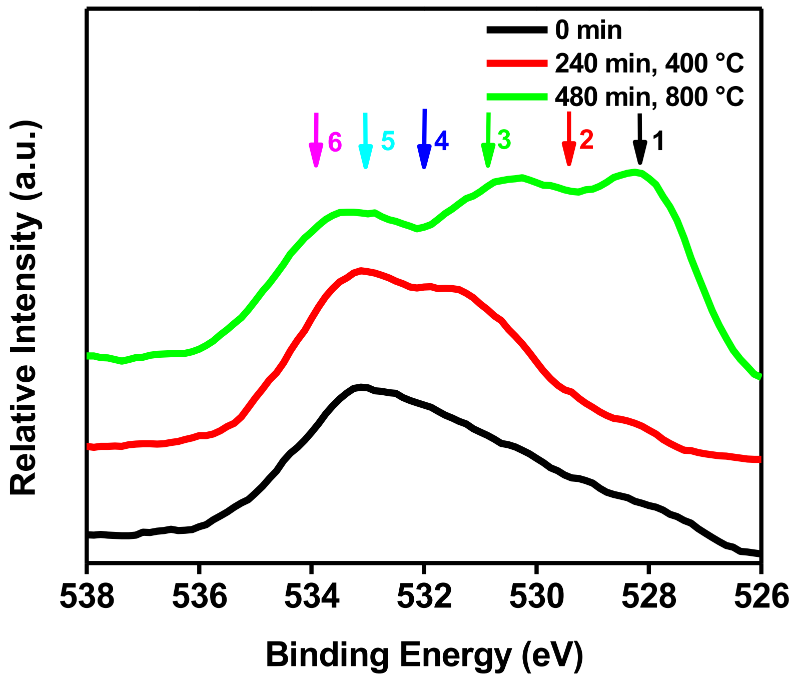

Figure 4.31: *Comparison between O 1s peak region of sample not annealed (0 min), sample annealed for 240 min at 400 °C and sample annealed for 480 min at 800 °C (Components: 1 - Eu_2O_3, 2- La_2O_3, 3 - Defects O(II)/ Hydroxide, 4 - CO_2/ CO_3/ Chemisorbed CO_2, 5 - H_2O, 6 - Physisorbed CO_2).*

4.3.3 Decay of luminescence

In an effort to correlate the observed increase in the cumulative intensity as a function of annealing time, as shown in Figure 4.23, to the removal of hydroxide impurities, the luminescence decay properties of the samples were studied. As discussed in a previous section, transitions originating from the $^5D_2$ and $^5D_1$ excited states has a double exponential luminescence decay resulting from the conventional emission from the rare earth ions and emission from rare earth ions that are in the vicinity of a hydroxide groups. These hydroxide groups capture the electrons and release them after some time that results in the longer decay constant. To prove this the luminescence decay properties of the La_2O_2S:Eu(III) phosphor material was studied as a function of period of annealing, by using the Fluorescence spectroscopy technique. This was done using the temperature controller unit to anneal La_2O_2S:Eu(III). samples at 400 °C for 0 min, 60 min and 240 min. After these periods of time the samples were cooled to room temperature and placed in the Varian Cary Eclipse fluorescence spectrophotometer for luminescence decay analysis.

Using Equation 2.10, Equation 2.11 and the luminescence decay data for the different samples (0 min, 60 min and 240 min), the FAST (Advanced Analysis of Fluorescence Kinetics) program was able to determine the fraction of Eu(III) ions in the presence of the hydroxide groups for the transitions listed in Table 4.10 [12]. From these results, it is observed that the fraction of Eu(III) ions, in the presence of the hydroxide groups, decreases as a function of annealing period. This also proves the removal of hydroxide impurities during the annealing process as observed with the study of both the structural and chemical properties. Therefore, the observed increase in the cumulative intensity as a function of annealing time, shown in Figure 4.23 results from the removal of the hydroxide impurities that act as quenching centres for luminescence [64].

Table 4.10: *Fraction of Eu(III) ions, in the vicinity of the hydroxide groups as a function of annealing period.*

Transition	**0 min**	**60 min**	**240 min**
$^5D_2$-$^7F_3$	29.2 %	23.1 %	17.5 %
$^5D_1$-$^7F_1$	62.4 %	61.8 %	60.0 %
$^5D_1$-$^7F_2$	62.0 %	60.1 %	55.2 %
$^5D_0$-$^7F_0$	79.9 %	77.0 %	75.8 %
$^5D_1$-$^7F_3$	72.9 %	71.7 %	70.9 %

5. Conclusions

The main objective of this study was achieved by successfully developing a system that can be used to study the emission of phosphor materials at various temperatures. The PL system at the Department of Physics at the University of the Free State was studied in detail and modified to measure the emission of a phosphor material from 350 to 800 nm while the temperature can be set or scanned between 30 to 420 °C. Modifications to this system include a temperature controller to allow the accurate measurement and control of the temperature of the phosphor materials, a beam splitter together with a power meter to be used as a reference detector for the excitation source and a sample holder together with an XYZ stage that ensures position-stability and position-control for the samples throughout measurements. An analog-to-digital/digital-to-analog converter was utilised to read and write voltage signals from and to the various components of the modified system. The analog-to-digital converter was setup in such a fashion to average out the effect of the 50 Hz noise from the mains grid supply, on the electrical signals read from the various components. A program was developed to allow user-friendly control and automation of the modified system and to allow the accurate acquisition of various conditions and parameters.

To obtain a better understanding of the mechanism behind the photoluminescence process of the commercially available La_2O_2S:Eu(III) phosphor powder, the absorption, charge transfer bands and lifetime properties were studied by utilising the ultraviolet-visible and fluorescence spectroscopy techniques. By using diffused reflectance spectra, the absorption process was studied and the optical band gap was determined as 2.75 eV, while the charge transfer band structure was determined to have both O(II) → Eu(III) and S(II) → Eu(III) character. It was determined that using an excitation source of 325 nm, the S(II) to Eu(III) charge transfer band is responsible for both the absorption of the excitation and the transfer of the excited electrons to the excited states of the Eu(III) ions. Lifetime of luminescence results show that the higher excited states of the Eu(III) ion have a double exponential lifetime which results from the emission from both the conventional rare earth ions and rare earth ions that are in the vicinity of a defect or impurity group. These defect or impurity groups capture the electrons and release them after some time that result in the longer decay constant. It was determined that in the case of the La_2O_2S:Eu(III) phosphor material, the presence of defect or impurity groups are due to hydroxide groups that form when the material is exposed to water vapour in the atmosphere at room temperature. The average emission decay constants of the $^5D_2$, $^5D_1$ and $^5D_0$ excited states were determined as 0.01, 0.08 and 0.34 ms respectively. The average emission decay constants of the transitions from the higher excited states of the Eu(III) ion, is significantly shorter than those from the lower excited states. The reason for this is due to the lower activation energies of the higher excited states that cause an increase in the non-radiative transition probability and that in return cause a shortening in the total emission decay constant.

The in-house modified PL system was used to study the thermal quenching effect by measuring the emission intensity of the different transitions of commercially available La_2O_2S:Eu(III) phosphor powder from 510 to 720 nm in the temperature range from 30 to 330 °C. The average activation energies for the thermal quenching process of the emission from the $^5D_2$, $^5D_1$ and $^5D_0$ excited states were determined as 0.49, 0.55 and 0.77 eV respectively, while the average pre-exponential constant was determined as 9.5×10^7 s^{-1}. The modified PL system was also used to determine if the emission properties of this material could be used as an accurate optical thermometry and to determine universal pre-calibrated data necessary. It was determined that this material can be utilised as a temperature sensor in the temperature range from 80 to 180 °C by monitoring the intensity ratio between the emissions that occurred from the $^5D_1$ and the $^5D_0$ excited states.

The above-mentioned system was developed to allow the study of the stability of the emission of thermographic phosphors at various temperatures. It was observed that the overall luminescence intensity of the La_2O_2S:Eu(III) increased at a constant temperature of 400 °C as a function of time. The emission stability results were investigated by the aid of the structural- and chemical properties by utilising the XRD- and XPS techniques respectively. The XRD results indicate a decrease of the strain in the lattice as a function of period of annealing. This is due to the removal of defects or impurities in the crystal lattice. The reduction of hydroxide impurities was firstly confirmed using the XPS technique by monitoring the intensity and positions of the different components of the La(III) and O(II) peaks. Lastly this was confirmed with the measurement of the decrease of the hydroxide component of the decay of luminescence, as a function of annealing time.

5.1 Future studies

This study serves to be just another step on the ladder of science. However future work is still required. Here follow proposals for possible future studies:

- Modify the PL system with cryostat to allow the study of the emission of the $^5D_4$, $^5D_3$, $^5D_2$, $^5D_1$ and $^5D_0$ excited states of the La_2O_2S:Eu(III) phosphor material at temperatures below room temperature.
- Setup the modified PL system to study the luminescence decay as a function of temperature by utilising the pulsed excitation source, the fast response time of the PMT detector and the 1 MHz sampling rate of the analog-to-digital converter.
- Study the emission from different excited states as a function of Eu(III) activator ion concentration in the host matrix, with the objective to increase the sensitivity for temperature sensing using the FIR technique.
- Design a study to investigate the effect that cause the emission from the $^5D_0$ excited state to quench at lower than expected temperatures.
- A detailed study of the effect of the hydroxide impurities/defects on the different excited states and the determining the mechanism that causes the luminescence to increase with a reduction in hydroxide impurity groups.

Bibliography

[1] A. H. Khalid and K. Kontis, "Thermographic phosphors for high temperature measurements: principles, current state of the art and recent applications," *Aerospace Sensor Systems,* vol. 8, no. 9, pp. 5673-744, 15 09 2008.

[2] S. W. Allison and G. T. Gillies, "Remote thermometry with thermographic phosphors: instumentation and applications," *Review of Scientific Instruments,* vol. 68, no. 7, pp. 2615-24, 04 1997.

[3] G. Laufer, Introduction to Optics and Lasers in Engineering, Cambridge University Press, 1996.

[4] S. V. Yap, R. M. Ranson, W. M. Crant and D. Koutsogeorgis, "Decay time characteristics of La2O2S:Eu and La2O2S:Tb for use with an optical sensor for human skin temperature measurement," *Applied Optics,* vol. 47, no. 27, pp. 4895-9, 20 09 2008.

[5] Intematix Corporation, "Intematix Technology," 2016. [Online]. Available: http://www.intematix.com/technology/whatisphosphor. [Accessed 20 10 2016].

[6] W. M. Yen, S. Shionoya and H. Yamamoto, Fundamentals of Phosphors, CRC Press, 2006.

[7] H. Föll, "Types of Luminescence," [Online]. Available: http://www.tf.uni-kiel.de/matwis/amat/admat_en/kap_5/advanced/t5_2_4.html. [Accessed 23 10 2016].

[8] Pan Alytical, "ASDInc," [Online]. Available: http://www.asdi.com/learn/faqs/what-is-luminescence. [Accessed 20 10 2016].

[9] S. A. Bakar, S. T. Hussain and M. Mazhar, "CdTiO3 thin films from an octa-nuclear bimetallic single source precursor by aerosol assisted chemical vapor deposition," *The Royal Society of Chemistry and the Centre National de la Recherche Scientifique,* vol. 36, pp. 1844-51, 15 06 2012.

[10] Boundless Physics, "Boundless Fluorescence and Phosphorescence," 08 08 2016. [Online]. Available: https://www.boundless.com/physics/textbooks/boundless-physics-textbook/introduction-to-quantum-physics-28/applications-of-quantum-mechanics-183/fluorescence-and-phosphorescence-676-4913/. [Accessed 20 10 2016].

[11] A. Leike, “Demonstration of the exponential decay law using beer froth,” *European Journal of Physics,* vol. 23, no. 1, pp. 21-6, 17 12 2001.

[12] Edinburgh Instruments Ltd, “Operating Instructions FAST Advanced Analysis of Fluorescence Kinetics,” 12 2011. [Online]. Available: https://www.edinst.com/products/fast-software-advanced-lifetime-analysis/.

[13] A. Sillen and Y. Engelborghs, “The Correct Use of “Average” Fluorescence Parameters,” *Photochemistry and Photobiology,* vol. 67, no. 5, pp. 475-86, 05 1998.

[14] D. M. Hanson, E. Harvey, R. Sweeney and T. J. Zielinski, “The Born-Oppenheimer Approximation,” 11 30 2015. [Online]. Available: https://chem.libretexts.org/Textbook_Maps/Physical_and_Theoretical_Chemistry_Textbook_Maps/Map%3A_Physical_Chemistry_(McQuarrie_and_Simon)/09%3A_The_Chemical_Bond%3A_Diatomic_Molecules/09.1%3A_The_Born-Oppenheimer_Approximation_Simplifies_the_Schrodinger_. [Accessed 06 02 2018].

[15] K. N. Shinde, S. J. Dhoble, H. C. Swart and K. Park, Phosphate Phosphors for Solid-State Lighting, vol. 14, Springer, 2012.

[16] K. Narita, T. Hase, S. Kamiya, E. Nakazawa, K. Ohno, M. Tamatani, M. J. Weber and H. Yamamoto, Phosphor Handbook, P. R. Society, Ed., CRC Press, 2006.

[17] R. Vali, “Electronic, dynamical, and dielectric properties of lanthanum oxysulfide,” *Computational Materials Science,* vol. 37, no. 3, pp. 300-5, 03 09 2006.

[18] Shimanzu Corporation, “Measurements of Band Gap in Compound Semiconductors - Band Gap Determination from Diffuse Re ectance Spectra -,” Tokyo.

[19] Y. F. Li, B. Xia, Y. M. Gao and Y. H. Cheng, “Theoretical study of anisotropic structural, electronic, mechanical and thermodynamic properties of rare-earth (R = Y, La) oxysulfides,” *Computational Materials Scienc,* vol. 125, pp. 154-67, 10 09 2016.

[20] D. Ma, S. Liu, Y. Zhang, C. Zhang and S. Huang, “Controlled synthesis of Eu3+-doped La2O2S nanophosphors by refluxing method,” *Journal of Experimental Nanoscience,* vol. 8, no. 3, pp. 434-41, 28 06 2012.

[21] M. F. Sunding, K. Hadidi, S. Diplas, O. M. Løvvik, T. E. Norby and A. E. Gunnæs, “XPS characterisation of in situ treated lanthanum oxide and hydroxide using tailored charge referencing and peak fitting procedures,” *Journal of Electron Spectroscopy and Related Phenomena,* vol. 184, no. 7, pp. 399-409, 07 2011.

[22] W. D. Roos, Interviewee, *Prof.*. [Interview]. 30 8 2016.

[23] K. Binnemans, “Interpretation of europium(III) spectra,” *Coordination Chemistry Reviews,* vol. 295, pp. 1-45, 1 07 2015.

[24] R. D. Shannon, “Revised Effective Ionic Radii and Systematic Studies of Interatomic Distances in Halides and Chalcogenides,” *Acta Crystallographic,* vol. A32, pp. 751-67, 9 3 1976.

[25] IEEE GlobalSpec, “Engineering 360,” 2016. [Online]. Available: http://www.globalspec.com/learnmore/optical_components_optics/lasers/helium_cadmium_hecd_lasers. [Accessed 29 12 2016].

[26] S. M. Goldwasser, “Helium-Cadmium Lasers,” 2016. [Online]. Available: https://www.repairfaq.org/sam/laserhec.htm. [Accessed 27 12 2016].

[27] Kimmon Koha CO., LTD., “Helium-Cadmium Laser Instruction Manual for Laser Head IK3401R-F and Power Supply KR1801C5001,” 04 2014. [Online]. Available: http://www.kimmon.com/datasheets/IK%20KP%20Manual(E).pdf. [Accessed 16 12 2016].

[28] User Manual, “Certificate of spectral characteristics, Set number 8186”.

[29] Coherent, “FieldMaxII-TOP,” 12 2014. [Online]. Available: https://www.coherent.com/measurement-control/measurement/fieldmaxii-top. [Accessed 15 12 2016].

[30] Edmund Optics Inc., “Edmund Optics, Techspec, UV Plate Beamsplitter,” 2016.

[31] Andor, “Andor an Oxford Instruments Company,” [Online]. Available: http://www.andor.com/learning-academy/diffraction-gratings-understanding-diffraction-gratings-and-the-grating-equation. [Accessed 30 08 2017].

[32] Horiba Jobin Yvon, “iHR Fully Automated Imaging Spectrometer, iHR320, iHR550, User Manual,” [Online]. Available: http://chemistry.unt.edu/~verbeck/LIMS/Manuals/iHR_user.pdf. [Accessed 18 05 2016].

[33] Horiba Scientific, “Diffraction Gratings,” [Online]. Available: http://www.horiba.com/us/en/scientific/products/optics-tutorial/diffraction-gratings/. [Accessed 22 12 2016].

[34] J. R. Lakowicz, “Intrumentation for Fluorecence Spectroscopy,” in *Principles of Fluorescence Spectroscopy*, vol. 26, Springer, 2006, pp. 27-61.

[35] Hamamatsu, “Hamamatsu Photomultiplier tube R943-02 Data Sheet,” [Online]. Available: https://www.hamamatsu.com/resources/pdf/etd/R943-02_TPMH1115E.pdf. [Accessed 08 07 2016].

[36] Hamamatsu Photonics, “Thermoelectric Coolers C10372/C10373 Instruction Manual,” [Online]. Available: https://www.hamamatsu.com/resources/pdf/etd/PMT_116-119_en.pdf. [Accessed 09 07 2016].

[37] Burk, Polansky, Repetto, Roberts and Rockmore. [Online]. Available: http://cmc.music.columbia.edu/MusicAndComputers/chapter3/03_03.php. [Accessed 08 10 2017].

[38] Stanford Research Systems Inc., “MODEL SR830 DSP Lock-In Amplifier,” 10 2011. [Online]. Available: http://www.thinksrs.com/downloads/PDFs/Manuals/SR830m.pdf. [Accessed 12 06 2005].

[39] EAGLE Technology, “USB-26/30-BNC Product Datasheet,” 2016.

[40] EAGLE Technology, “User´s Manual for USB uDAQ, USB Rugged uDAQ, SERIAL uDAQ, SERIAL Rugged uDAQ, WIRELESS uDAQ, WIRELESS Rugged uDAQ, Eagle Technology Data Acquisition and Process Control,” 2004.

[41] Maxim Integrated, “Implementing Cold-Junction Compensation in Thermocouple Applications,” 26 04 2007. [Online]. Available: https://www.maximintegrated.com/en/app-notes/index.mvp/id/4026. [Accessed 21 12 2016].

[42] Omega, “Revised Thermocouple Reference Tables, K-Type,” [Online]. Available: http://www.omega.com/temperature/z/pdf/z204-206.pdf. [Accessed 14 04 2016].

[43] Varian, “Cary Eclipse Guaranreed Specifications,” [Online]. Available: https://www.qui.ufmg.br/wp-content/uploads/2013/10/Cary_Eclipse_Specifications.pdf. [Accessed 15 1 2017].

[44] Agilent Technologies, “VarianInc.,” [Online]. Available: https://www.agilent.com/cs/library/brochures/Cary-Eclipse_FLR-brochure.pdf. [Accessed 2017 08 31].

[45] N. Knighton and B. Bugbee, “A Mixture of Barium Sulfate and White Paint is a Low-Cost Substitute Reflectance Standard for Spectralon,” Utah State University Merrill-Cazier Library, 2005.

[46] Agilent Technologies, “Agilent Cary 4000/5000/6000i Series UV-VIS-NIR,” [Online]. Available: http://www.agilent.com/cs/library/brochures/5990-7786EN_Cary-4000-5000-6000i-UV-Vis-NIR_Brochure.pdf. [Accessed 11 09 2017].

[47] R. Territ, “Chemistry Stack Exchange,” 1 09 2013. [Online]. Available: https://chemistry.stackexchange.com/questions/6091/what-is-the-principle-of-diffuse-reflectance-spectroscopy-behind-band-gap-measur. [Accessed 26 2 2017].

[48] J. J. Terblans, J. Du Plessis and G. N. Van Wyk, Die ontwikkeling van ´n sagtewarepakket vir die beheer van en die dataverwerking vanaf ´n skandeeraugermikroskoop, University of the Free State, 1997.

[49] B. L. Dutrow and C. M. Clark, “Geochemical Instrumentation and Analysis,” 04 09 2017. [Online]. Available: https://serc.carleton.edu/research_education/geochemsheets/techniques/XRD.html. [Accessed 05 09 2017].

[50] J. K. Cockcorft, “Birkbeck College,” 2006. [Online]. Available: http://pd.chem.ucl.ac.uk/pdnn/inst1/monoc.htm. [Accessed 23 02 2017].

[51] D. L. Bish and J. E. Post, “X-ray Generation and Powder Diffraction,” [Online]. Available: http://ruby.colorado.edu/~smyth/G30105.html. [Accessed 22 2 2017].

[52] A. Monshi, M. R. Foroughi and M. R. Monshi, “Modified Scherrer Equation to Estimate More Accurately Nano-Crystallite Size Using XRD,” *World Journal of Nano Science and Engineering,* vol. 2, no. 3, pp. 154-60, 28 8 2012.

[53] C. D. Wagner, W. M. Riggs, L. E. Davis and J. F. Moulder, Handbook of X-ray Photoelectron Spectroscopy, Perkin-Elmer Corporation, 1979.

[54] Centro De Investigación Y De Estudios Avanzados Del Ipn Unidad Querétaro, “The Peak-Shirley Background,” Cinvestav- Queretaro, 2012.

[55] Thermo Fisher Scientific Inc., “Analysis Features, Charge Compensation,” 2016. [Online]. Available: http://xpssimplified.com/charge_compensation.php. [Accessed 24 02 2017].

[56] X. Wang, J.-G. Li, Q. Zhu, X. Li, X. Sun and Y. Sakka, “Facile and green synthesis of (La0.95Eu0.05) 2 O2 S red phosphors with sulfate-ion pillared layered hydroxides as a new type of precursor: controlled hydrothermal processing, phase evolution and photoluminescence,” *Science and Technology of Advanced Materials,* vol. 15, pp. 1-9, 20 12 2013.

[57] B. J. Van Zeghbroeck, “Principles of Semiconductor Devices,” 2011. [Online]. Available: https://ecee.colorado.edu/~bart/book/contents.htm. [Accessed 21 5 2017].

[58] R. H. Krauss, R. G. Hellier and J. C. McDaniel, “Surface temperature imaging below 300 K using La2O2S:Eu,” *Applied Optics,* vol. 33, no. 18, pp. 3901-4, 1994.

[59] M. D. Chambers, P. A. Rousseve and D. R. Clarke, “Decay pathway and high-temperature luminescence of Eu3+ in Ca2Gd8Si6O26,” *Journal of Luminescence,* vol. 129, no. 3, pp. 263-269, 03 2009.

[60] Edinburgh Photonics, FAST Advanced Analysis of Fluorescence Kinetics, vol. 3.4.0, 2011.

[61] M. P. Neary and H. M. David, Nonlinear Parameter Estimation of Convolved Excitation and Multiple Emission Response Functions, vol. 4, Springer, 2017, pp. 141-204.

[62] S. V. Yap, R. M. Ranson and W. M. Cranton, “Temperature Dependent Characteristics of La2O2S: Ln [Ln=Eu, Tb] with Various Ln Concentrations over 5 – 60 ˚C.,” *Journal of Luminescence,* vol. 129, no. 5, pp. 416-22, 05 2009.

[63] T. Suzukia, S. Hishitab, K. Oyoshib and R. Soudaab, “Surface segregation of implanted ions: Bi, Eu, and Ti at the MgO(100) surface Author links open overlay panel,” *Applied Surface Science,* vol. 130, no. 132, pp. 534-8, 26 01 1999.

[64] D. V. Skobel tsyn, Soviet Researches on Luminescence, vol. 23, Springer, 1964.

[65] J. R. Church, Thin film subsurface environments: advanced X-ray spectroscopies and a novel Bayesian inference modeling algorithm, University of Delaware, 2015, p. 10.

[66] N. R. Finney, “Science Projects Modern Physics Lab,” 2008. [Online]. Available: http://natefinney.com/science/. [Accessed 4 5 2017].

[67] A. Messerschmidt and R. Huber, X-Ray Crystallography of Biological Macromolecules, Encyclopedia of Analytical Chemistry, 2006.

[68] Structural Medicine, “Basic diffraction: waves, interference and reciprocal space,” 07 04 2009. [Online]. Available: http://www-structmed.cimr.cam.ac.uk/Course/Basic_diffraction/Diffraction.html. [Accessed 27 02 2017].

[69] Thermo Fisher Scientific Inc., “Learn XPS,” [Online]. Available: http://xpssimplified.com/whatisxps.php. [Accessed 21 02 2017].

Appendix A – Apparatus Specifications

Excitation Source

Specifications of Kimmon KOHA CO., LTD. Helium-Cadmium Laser.

Item	**IK3401R-F**
Wavelengths	325.0 nm, 441.6 nm
Initial Power	42.6 mW
Transverse Mode	TEM00
Beam Diameter ($1/e^2$)	0.91 mm
Beam Divergence	0.10 mrad
Polarization	Linear
Noise (Peak-to-Peak)	4.7 %
Warm Up Time (90 % Power)	13.0 min
Beam Pointing Stability	± 25 μrad

Measured by manufacturer on 20-05-2009.

Spectroscope

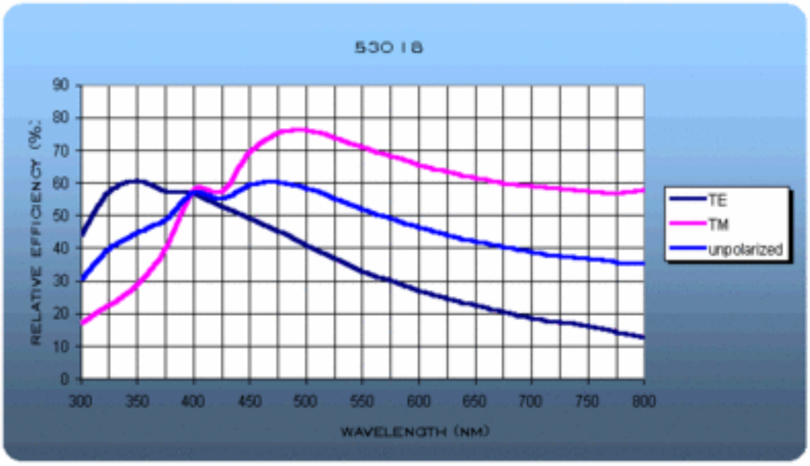

Relative efficiency of 1800 lines/mm diffraction grating (TE: Transverse Electric, TM: Transverse Magnetic).

Specifications of iHR320 spectroscope and the 1800 lines per mm diffraction grating.

Spectral Resolution	0.06 nm
Wavelength Position Accuracy	± 0.20 nm
Wavelength Repeatability	± 0.075 nm
Minimum Drive Step Size	0.002 nm
Diffraction Grating Typical Linear Dispersion	1.57 nm/mm
Diffraction Grating Typical Array Resolution	<0.1 nm
Diffraction Grating Typical Spectral Coverage	41 nm
Diffraction Grating Scan Range	0-1000 nm
Turret Repeatability Test	0.049 nm
Drive Repeatability Test	0.001 nm
Resolution Test (Entrance and Exit Slit Width=0.01 nm)	0.017 nm
Drive Linearity Test (Entrance and Exit Slit Width=0.01 nm)	0.030 nm

Detector

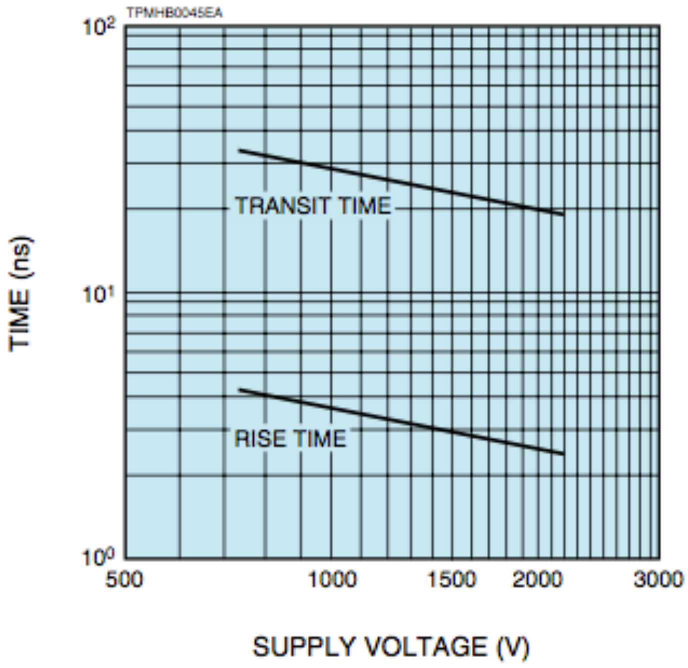

Response time of Hammamatsu Photomultiplier Tube R943-02.

Appendix B – Programming Code

For more information, complete programming code and Program see included compact disc.

Set Slits Width

```
Public Sub Slits(FrontEntrance As Double, FrontExit As Double, SideEntrance As Double, SideExit As Double)
    Mono1.SetDefaultUnits jyutSlitWidth, jyuMicrons
    Mono1.IsTargetWithinLimits jyMonoMoveTypeSlit, Val(FrontEntrance), InLimits, MinSlits, MaxSlits, 0
        If FrontEntrance < MinSlits Then
        FrontEntrance = MinSlits
        End If
        If FrontEntrance > MaxSlits Then
        FrontEntrance = MaxSlits
        End If
    Mono1.MovetoSlitWidth Front_Entrance, Val(FrontEntrance)
        While (Mono1.IsBusy = True)
            DoEvents
        Wend
    FrontEntranceCurrent = Mono1.GetCurrentSlitWidth(Front_Entrance)
    FrontEntranceBox.Text = Format(FrontEntranceCurrent, "0")
    If FrontEntrance > 0 Then
        FrontEntranceBox.BackColor = QBColor(2)
        Else
        FrontEntranceBox.BackColor = QBColor(4)
    End If
    Mono1.IsTargetWithinLimits jyMonoMoveTypeSlit, Val(FrontExit), InLimits, MinSlits, MaxSlits, 1
        If FrontExit < MinSlits Then
        FrontExit = MinSlits
        End If
        If FrontExit > MaxSlits Then
        FrontExit = MaxSlits
        End If
    Mono1.MovetoSlitWidth Front_Exit, Val(FrontExit)
```

```
        While (Mono1.IsBusy = True)
             DoEvents
        Wend
    FrontExitCurrent = Mono1.GetCurrentSlitWidth(Front_Exit)
    FrontExitBox.Text = Format(FrontExitCurrent, "0")
    If FrontExitCurrent > 0 Then
        FrontExitBox.BackColor = QBColor(2)
        Else
        FrontExitBox.BackColor = QBColor(4)
    End If

Mono1.IsTargetWithinLimits jyMonoMoveTypeSlit, Val(SideEntrance), InLimits, MinSlits, MaxSlits, 2
        If SideEntrance < MinSlits Then
        SideEntrance = MinSlits
        End If
        If SideEntrance > MaxSlits Then
        SideEntrance = MaxSlits
        End If
    Mono1.MovetoSlitWidth Side_Entrance, Val(SideEntrance)
        While (Mono1.IsBusy = True)
            DoEvents
        Wend
    SideEntranceCurrent = Mono1.GetCurrentSlitWidth(Side_Entrance)
    SideEntranceBox.Text = Format(SideEntranceCurrent, "0")
    If SideEntranceCurrent > 0 Then
        SideEntranceBox.BackColor = QBColor(2)
        Else
        SideEntranceBox.BackColor = QBColor(4)
    End If
    Mono1.IsTargetWithinLimits jyMonoMoveTypeSlit, Val(SideExit), InLimits, MinSlits, MaxSlits, 3
        If SideExit < MinSlits Then
        SideExit = MinSlits
        End If
        If SideExit > MaxSlits Then
        SideExit = MaxSlits
```

```
        End If
    Mono1.MovetoSlitWidth Side_Exit, Val(SideExit)
        While (Mono1.IsBusy = True)
            DoEvents
        Wend
    SideExitCurrent = Mono1.GetCurrentSlitWidth(Side_Exit)
    SideExitBox.Text = Format(SideExitCurrent, "0")
    If SideExitCurrent > 0 Then
        SideExitBox.BackColor = QBColor(2)
        Else
        SideExitBox.BackColor = QBColor(4)
    End If
End Sub
```

Adjust Grating

```
Public Function Grating(Wavelength As Single)
Mono1.SetDefaultUnits jyutWavelength, jyuNanometers
Mono1.IsTargetWithinLimits jyMonoMoveTypeWavelength, Val(Wavelength), InLimit, MinGrating, MaxGrating
    If Wavelength < MinGrating Then
    Wavelength = MinGrating
    End If
    If Wavelength > MaxGrating Then
    Wavelength = MaxGrating
    End If
Mono1.MovetoWavelength Val(Wavelength)
            While (Mono1.IsBusy = True)
                DoEvents
            Wend
Grating = Mono1.GetCurrentWavelength
End Function
```

Adjust Fold Away Mirror

```
Private Sub Btn_Mirror_Exit_Front_Click()
On Error GoTo jyHandler
Dim mirrorLocation As Integer
    Mono1.MovetoMirrorPosition ExitMirror, Front
    mirrorLocation = Mono1.GetCurrentMirrorPosition(ExitMirror)
    If mirrorLocation = Front Then
        Frame_Mirror_Exit.Caption = "Exit = Axial"
    Else
        Frame_Mirror_Exit.Caption = "Exit = Lateral"
    End If
Exit Sub
jyHandler:
MsgBox "HRESULT: " & Hex(Err.Number) & vbCr _
    & "Source: " & Err.Source & vbCr _
    & "Description: " & Err.Description
End Sub

Private Sub Btn_Mirror_Exit_Side_Click()
On Error GoTo jyHandler
Dim mirrorLocation As Integer
    Mono1.MovetoMirrorPosition ExitMirror, Side
    mirrorLocation = Mono1.GetCurrentMirrorPosition(ExitMirror)
    If mirrorLocation = Front Then
        Frame_Mirror_Exit.Caption = "Exit = Axial"
    Else
        Frame_Mirror_Exit.Caption = "Exit = Lateral"
    End If
Exit Sub

jyHandler:
MsgBox "HRESULT: " & Hex(Err.Number) & vbCr _
    & "Source: " & Err.Source & vbCr _
    & "Description: " & Err.Description
```

```
End Sub
```

Scan Spectrum

```
Public Sub ScanSpectrum()
Dim Wavelength As Single
    ScanCounter = 0
    DataPoints = 0
    Erase WavelengthArray
    Erase IntensityArray
    Erase TemperatureArray
    Erase RoomTemperatureArray
    Erase LaserIntensityArray
    Erase MatrixWavelengthArray
    Erase MatrixIntensityArray
    Erase MatrixTemperatureArray
    Erase MatrixRoomTemperatureArray
    Erase MatrixLaserIntensityArray
        DataPoints = (WavelengthStop - WavelengthStart) / WavelengthStep + 10
    ReDim WavelengthArray(DataPoints) As Single
    ReDim IntensityArray(DataPoints) As Double
    ReDim TemperatureArray(DataPoints) As Double
    ReDim RoomTemperatureArray(DataPoints) As Double
    ReDim LaserIntensityArray(DataPoints) As Double

    For GraphClear = 11 To 15
            Graph.Clear_Graph (GraphClear)
    Next GraphClear

    If SpectrumCounter = 1 Then
        Legend.Visible = True
    End If

    Legend.Height = (SpectrumCounter - 1) * 360 + 585
```

```
    LegendCheck(SpectrumCounter).Enabled = False
    LegendCheck(SpectrumCounter).Value = 1
    If TemperatureCheck = 0 Then
        SpectrumStatus = SpectrumCounter
        LegendText(SpectrumCounter).Text = SpectrumStatus
        Else
        LegendText(SpectrumCounter).Text = Format(Temperature, "0.0" & " C")
    End If
    LegendText(SpectrumCounter).ForeColor = QBColor(SpectrumCounter)
    LegendText(SpectrumCounter).Enabled = True
Do
DoEvents
    ScanCounter = ScanCounter + 1
    Grating WavelengthStart
    Slits Val(FrontEntranceBox), Val(FrontExitBox), Val(SideEntranceBox), Val(SideExitBox)
        DataCount = 0
        DataNumber = 0
    DelayTime (1)
        For Wavelength = WavelengthStart To WavelengthStop Step WavelengthStep
            DelayTime (0.05)
            WavelengthCurrent = Grating(Wavelength)
            WavelengthBox = Format(WavelengthCurrent, "0.0" & " nm")
           ReadVoltage (PointsToAverage)
           If Intensity > 2.5 Then
            ShutterClose
            Grating WavelengthStart
            StopFlag = 1
           End If
        IntensityBox.Text = Format(Intensity, "0.0" & " V")
        TemperatureBox.Text = Format(TemperatureCurrent, "0.0" & " C")
        LaserIntensityBox.Text = Format(LaserIntensity, "0.0" & " mW")
        RoomTemperatureBox.Text = Format(RoomTemperature, "0.0" & " C")
            GraphDraw WavelengthStart, WavelengthStop, 10 + ScanCounter, WavelengthCurrent, Intensity, 1
            DataCount = DataCount + 1
            WavelengthArray(DataCount) = WavelengthArray(DataCount) + WavelengthCurrent
```

```
            IntensityArray(DataCount) = IntensityArray(DataCount) + Intensity
            TemperatureArray(DataCount) = TemperatureArray(DataCount) + TemperatureCurrent
            RoomTemperatureArray(DataCount) = RoomTemperatureArray(DataCount) + RoomTemperature
            LaserIntensityArray(DataCount) = LaserIntensityArray(DataCount) + LaserIntensity
            If StopFlag = 1 Then
                Exit For
            End If
        Next Wavelength

    If ScansToAverage = ScanCounter Then
        Exit Do
    End If
    If StopFlag = 1 Then
        Exit Do
    End If

Loop

    DataNumber = DataCount
    DataNumberArray(SpectrumCounter) = DataNumber

    For DataCount = 1 To DataNumber
        WavelengthMatrix(SpectrumCounter, DataCount) = WavelengthArray(DataCount) / ScanCounter
        IntensityMatrix(SpectrumCounter, DataCount) = IntensityArray(DataCount) / ScanCounter
        TemperatureMatrix(SpectrumCounter, DataCount) = TemperatureArray(DataCount) / ScanCounter
        RoomTemperatureMatrix(SpectrumCounter, DataCount) = RoomTemperatureArray(DataCount) / ScanCounter
        LaserIntensityMatrix(SpectrumCounter, DataCount) = LaserIntensityArray(DataCount) / ScanCounter
    Next DataCount

    ReDim MatrixWavelengthArray(DataPoints) As Single
    ReDim MatrixIntensityArray(DataPoints) As Single
    ReDim MatrixTemperatureArray(DataPoints) As Double
    ReDim MatrixRoomTemperatureArray(DataPoints) As Double
    ReDim MatrixLaserIntensityArray(DataPoints) As Double
```

```
    Graph.XAxisMinimum = WavelengthMatrix(SpectrumCounter, 1)
    Graph.XAxisMaximum = WavelengthMatrix(SpectrumCounter, DataNumber)

    For DataCount = 1 To DataNumber
        MatrixWavelengthArray(DataCount) = WavelengthMatrix(SpectrumCounter, DataCount)
        MatrixIntensityArray(DataCount) = IntensityMatrix(SpectrumCounter, DataCount)
        MatrixTemperatureArray(DataCount) = TemperatureMatrix(SpectrumCounter, DataCount)
        MatrixRoomTemperatureArray(DataCount) = RoomTemperatureMatrix(SpectrumCounter, DataCount)
        MatrixLaserIntensityArray(DataCount) = LaserIntensityMatrix(SpectrumCounter, DataCount)
    Next DataCount

    For DataCount = 1 To DataNumber
        Graph.LineGraphArray SpectrumCounter, MatrixWavelengthArray, MatrixIntensityArray, QBColor(SpectrumCounter),_
4, DataNumber, [Spectra]
    Next DataCount
    LegendCheck(SpectrumCounter).Value = 1
    LegendCheck(SpectrumCounter).Enabled = True
    IntensityMaximum = IntensityMatrix(SpectrumCounter, 1)
    For DataCount = 1 To DataNumber
        If IntensityMaximum < IntensityMatrix(SpectrumCounter, DataCount) Then
            IntensityMaximum = IntensityMatrix(SpectrumCounter, DataCount)
            WavelengthMaximum = WavelengthMatrix(SpectrumCounter, DataCount)
        End If
    Next DataCount

WavelengthPositionBox.Text = Format(WavelengthMaximum, "0.0")
Grating WavelengthStart

End Sub
```

Grating Settings

```
Private Sub Combo_Grating_Click()
On Error GoTo jyHandler
 Mono1.MovetoTurret (Combo_Grating.ListIndex)
Exit Sub

jyHandler:
MsgBox "HRESULT: " & Hex(Err.Number) & vbCr _
    & "Source: " & Err.Source & vbCr _
    & "Description: " & Err.Description
End Sub
Private Sub Combo_Mono_Click()
Rem
Rem recreate the mono if mono has been loaded before.  This IS necessary for mono because
Rem different types of monos have different configuration settings right after load.
Rem A newly selected mono needs to be created FRESH.
Rem
If (m_monoLoaded = True) Then
    Set Mono1 = Nothing
    Set Mono1 = CreateObject("JYMono.Monochromator")
End If

Rem Load the current mono
Dim UseIndex As Integer
Dim monoUID As String
Dim iCommType As Integer
Dim iCommPort As Integer

UseIndex = Combo_Mono.ListIndex
monoUID = IDARRAY(UseIndex + 1, 1)
Mono1.Uniqueid = monoUID

Mono1.Load
iCommType = Mono1.ReadCommSetting(jyCPTCommType)
```

```
iCommPort = Mono1.ReadCommSetting(jyCPTPortNum)

Select Case (iCommType)
    Case jyGPIB:
        'Label_Communications_Type = "GPIB"
    Case jySerial:
        'Label_Communications_Type = "Serial"
    Case jyUSB:
        'Label_Communications_Type = "USB"
    Case jyIP:
        'Label_Communications_Type = "TCPIP"
End Select
    'Label_Communications_Port = iCommPort
    Menu_Initialise.Caption = "Initialise"
    'Label_Status.Caption = "Uninitialized"
End Sub
```

Optimisation

```
Private Sub Optimise_Click()
Enable False, False, True, False, True, False, False, True, False, False
WavelengthPosition = WavelengthPositionBox.Text
StopFlag = 0
WavelengthBox.BackColor = QBColor(0)
WavelengthCurrent = Grating(WavelengthPosition)
Slits Val(FrontEntranceBox), Val(FrontExitBox), Val(SideEntranceBox), Val(SideExitBox)
Do
DoEvents
    Graph.Clear_Graph (0)
        WavelengthBox.Text = Format(WavelengthCurrent, "0.0" & " nm")
           ReadVoltage (1)
           If Intensity > 2.5 Then
           ShutterClose
           Grating (WavelengthPosition * 0.6)
           WavelengthBox.BackColor = QBColor(4)
```

```
            StopFlag = 1
            End If
        IntensityBox.Text = Format(Intensity, "0.0" & " V")
        TemperatureBox.Text = Format(TemperatureCurrent, "0.0" & " C")
        RoomTemperatureBox.Text = Format(RoomTemperature, "0.0" & " C")
        LaserIntensityBox.Text = Format(LaserIntensity, "0.0" & " W")
    Graph.PointGraph 0, WavelengthCurrent, Intensity, QBColor(15), 4, 0, 4, 2, 1, Spectra
    If StopFlag = 1 Then
    Exit Do
    If ScanFlag = 1 Then Exit Do
    End If
Loop
Graph.Clear_Graph (0)
Enable True, False, False, True, True, True, True, True, True, True
Exit Sub
jyHandler:
MsgBox "HRESULT: " & Hex(Err.Number) & vbCr _
    & "Source: " & Err.Source & vbCr _
    & "Description: " & Err.Description
Enable False, False, True, False, True, False, False, True, False, False
End Sub
```

Time Scan Spectrum

```
Public Function ScanTime()
TimeZero = Timer
For TheTime = 0 To TimeStopSec Step TimeStepSec
    SpectrumCounter = SpectrumCounter + 1
    TimeCurrentBox.Text = Format((Timer - TimeZero) / 60, "0.00" & " min")
    TimeCurrentBox.BackColor = QBColor(4)
    Do
        DoEvents
        'ReadVoltage (1)
        IntensityBox.Text = Format(Intensity, "0.000" & " V")
        TemperatureBox.Text = Format(TemperatureCurrent, "0.00" & " C")
```

```
    LaserIntensityBox.Text = Format(LaserIntensity, "0.000" & " W")
        TimeCurrentBox.Text = Format((Timer - TimeZero) / 60, "0.00" & " min")
        If (Timer - TimeZero) > TheTime Then
        Exit Do
        End If
        If StopFlag = 1 Then
        Exit Do
        End If
Loop

    If StopFlag = 0 Then
    TimeCurrentBox.BackColor = QBColor(2)
    ScanSpectrum
    LegendText(SpectrumCounter).Text = Format((TheTime) / 60, "0.00" & " min")
End If


Settings(SpectrumCounter).FrontEntranceSave = FrontEntranceBox
Settings(SpectrumCounter).SideEntranceSave = SideEntranceBox
Settings(SpectrumCounter).FrontExitSave = FrontExitBox
Settings(SpectrumCounter).SideExitSave = SideExitBox
Settings(SpectrumCounter).Combo_GratingSave = Combo_Grating
Settings(SpectrumCounter).WavelengthStartSave = WavelengthStart
Settings(SpectrumCounter).WavelengthStopSave = WavelengthStop
Settings(SpectrumCounter).WavelengthStepSave = WavelengthStep
Settings(SpectrumCounter).PointsToAverageSave = PointsToAverage
Settings(SpectrumCounter).ScansToAverageSave = ScansToAverage

Settings(SpectrumCounter).TemperatureValueSave = Temperature

Settings(SpectrumCounter).TimeSave = TheTime
Settings(SpectrumCounter).TimeStopSave = TimeStop
Settings(SpectrumCounter).TimeStepSave = TimeStep

If StopFlag = 1 Then
```

```
        Exit For
    End If
Next TheTime
End Function
```

Setup MicroDAQ

```
Public Sub SetupADC(SerialNr As Long, Frequency As Single, ChannelList() As Long, ListLenght As Long)
    Dim ClockSource As Long
    Dim TriggerSource As Long
    Dim eerr As Long
    'SerialNr       - Serial Number of the Card
    'Frequency      - Frequency at which measurement will be taken. (in kHz)
    'ChannelList()  - Channels to be measured  [0,1,2,Ö]
    'GainList()     - Gain setting of each Channel
    'ListLenght     - Number of channels in the channel list.
    'Clock Source - Internal [0]
    ClockSource = 0
    'Trigger Source - Internal [0]
    TriggerSource = 0

    Dim i As Long
    Dim Range As Long
    Dim Gain As Long
    Dim GainList() As Long

    'Gain - X1/4 (+/-10V) Single-ended [0]
    Gain = 1
    'Range - Single-ended [0]
    Range = 0
    'setup gain and channel list
    ReDim GainList(ListLenght)
    For i = 0 To ListLenght - 1
        GainList(i) = 256 * Range + Gain + AGND
    Next i
```

```
    'Parameters = Frequency, Clock Source, Burst, Range, Channel List, Gain List, List Size
    USBError = EDRE_ADConfig(SerialNr, Frequency * 1000, (TriggerSource * 256) + ClockSource, 0, 0, ChannelList(0),_
GainList(0), ListLenght)

    ListLenghtCurrent = ListLenght

End Sub
```

Acquisition Data

```
Public Function ReadVoltage(PointsToAverage) As Double
AverageIntensity = 0
AverageTemperature = 0
AverageRoomTemperature = 0
AverageLaserIntensity = 0
Counter = 0
For Counter = 1 To PointsToAverage

    Dim eerr As Long

    'start sampling
    USBError = EDRE_ADStart(1000033182)

    Do
        'DoEvents
        MeasurementsTaken = EDRE_Query(1000033182, 109, 0) 'See query codes. This will return the number of available_
samples
        If MeasurementsTaken > 3875 Then Exit Do
    Loop

    'EDRE_ADStop SerialNr
    eerr = EDRE_ADStop(1000033182)

    USBError = EDRE_ADGetData(1000033182, uvInput(0), 3876)
```

```
   Dim i As Long
    Dim j As Long
    Dim k As Long
    Dim Vsum(8) As Single

    k = 0
    For i = 0 To 3
        Vsum(i) = 0
    Next i
    For i = 0 To 3876 - 1 Step 4
        For j = 0 To 7
            Vsum(j) = Vsum(j) + uvInput(i + j) / 1000000#
        Next j
        k = k + 1
    Next i
For i = 0 To 3
        Vin_Avg(i) = Vsum(i) / (3876 / 4)
    Next i

AverageIntensity = AverageIntensity + Vin_Avg(0)
AverageTemperature = AverageTemperature + Vin_Avg(1)
AverageRoomTemperature = AverageRoomTemperature + Vin_Avg(2)
AverageLaserIntensity = AverageLaserIntensity + Vin_Avg(3)

Next Counter


'RoomTemperature
RoomTemperature = Format((((AverageRoomTemperature / PointsToAverage)*10*0.99929 + 2.739), "0.000")
CalibrationCounter = 0
Do
DoEvents

    If TCTemperature(CalibrationCounter) > RoomTemperature Then
```

```
    Exit Do
    End If
CalibrationCounter = CalibrationCounter + 1
Loop
Slope = (TCVoltage(CalibrationCounter) - TCVoltage(CalibrationCounter - 1))
RoomTemperatureVoltage = Slope * RoomTemperature

'Temperature
TemperatureVoltage = ((AverageTemperature / PointsToAverage) / 0.2442724613) - RoomTemperatureVoltage
NegativeWatch = 0
If 0 > TemperatureVoltage Then
    NegativeWatch = 1
    TemperatureVoltage = TemperatureVoltage * -1
End If
CalibrationCounter = 0
Do
DoEvents
    If TCVoltage(CalibrationCounter) > TemperatureVoltage Then
    Exit Do
    End If
CalibrationCounter = CalibrationCounter + 1
Loop
Slope = 1 / (TCVoltage(CalibrationCounter) - TCVoltage(CalibrationCounter - 1))
If NegativeWatch = 1 Then
    TemperatureCurrent = Format(-Slope * TemperatureVoltage + RoomTemperature, "0.000")
Else
TemperatureCurrent = Format(Slope * TemperatureVoltage + RoomTemperature, "0.000")
End If
```

Temperature Scan

```
Public Function ScanTemperature()
TemperatureTime = TemperatureTimeBox.Text
For Temperature = TemperatureStart To TemperatureStop Step TemperatureStep
    ExitDo = 0

    TemperatureTotal = Temperature
    SpectrumCounter = SpectrumCounter + 1
    TemperatureVoltage = ((((((Temperature - 4.3067) / 0.9796) * 0.01015 + 0.00900305) / 1.0074) * 10 ^ 6))
    EDRE_DAWrite 1000033182, 0, TemperatureVoltage
    TemperatureValueBox.Text = Format(Temperature, "0.0")
    TemperatureBox.BackColor = QBColor(4)
        Do
        DoEvents
           ReadVoltage (1)
            IntensityBox.Text = Format(Intensity, "0.0" & " V")
            TemperatureBox.Text = Format(TemperatureCurrent, "0.0" & " C")
            RoomTemperatureBox.Text = Format(RoomTemperature, "0.0" & " C")
            LaserIntensityBox.Text = Format(LaserIntensity, "0.0" & " W")

                If  TemperatureCurrent  >  Temperature  -  TemperatureBand  And  TemperatureCurrent  <  Temperature  +_
TemperatureBand Then
                    StartTime = Timer
                    Do
                    DoEvents
                        ExitDo = 0

                        TemperatureTimeCount = TemperatureTime - (Timer - StartTime)
                        TemperatureTimeBox.Text = Format(TemperatureTimeCount, "0")
                       ReadVoltage (1)
            IntensityBox.Text = Format(Intensity, "0.0" & " V")
            TemperatureBox.Text = Format(TemperatureCurrent, "0.0" & " C")
            RoomTemperatureBox.Text = Format(RoomTemperature, "0.0" & " C")
            LaserIntensityBox.Text = Format(LaserIntensity, "0.0" & " W")
```

```
                            If TemperatureCurrent > Temperature + TemperatureBand Then
                                Exit Do
                            End If

                            If TemperatureCurrent < Temperature - TemperatureBand Then
                                Exit Do
                            End If

                            If TemperatureTimeCount < 0 Then
                                ExitDo = 1
                                Exit Do
                            End If

                            If StopFlag = 1 Then
                                Exit Do
                            End If
                    Loop
Else
TemperatureBox.BackColor = QBColor(4)
        StartTime = Timer
        Do
        DoEvents
            If (Timer - StartTime) > 60 Then Exit Do
            If StopFlag = 1 Then Exit Do
            ReadVoltage (1)
            IntensityBox.Text = Format(Intensity, "0.0" & " V")
            TemperatureBox.Text = Format(TemperatureCurrent, "0.0" & " C")
            RoomTemperatureBox.Text = Format(RoomTemperature, "0.0" & " C")
            LaserIntensityBox.Text = Format(LaserIntensity, "0.0" & " W")
        Loop
    TemperatureVoltage = (((((((TemperatureTotal + (Temperature - TemperatureCurrent)) - 4.3067) / 0.9796) * 0.01015_
+ 0.00900305) / 1.0074) * 10 ^ 6))
    EDRE_DAWrite 1000033182, 0, TemperatureVoltage
    TemperatureTotal = TemperatureTotal + (Temperature - TemperatureCurrent)
```

```
TemperatureBox.BackColor = QBColor(0)
If StopFlag = 1 Then Exit Do
End If

    If ExitDo = 1 Then
        Exit Do
    End If

    If StopFlag = 1 Then
        Exit Do
    End If

    Loop

If StopFlag = 0 Then
    TemperatureBox.BackColor = QBColor(2)
    ScanSpectrum
    LegendText(SpectrumCounter).Text = Format(Temperature, "0.0" & " C")
End If

If StopFlag = 1 Then
    Exit For
End If
Settings(SpectrumCounter).FrontEntranceSave = FrontEntranceBox
Settings(SpectrumCounter).SideEntranceSave = SideEntranceBox
Settings(SpectrumCounter).FrontExitSave = FrontExitBox
Settings(SpectrumCounter).SideExitSave = SideExitBox
Settings(SpectrumCounter).Combo_GratingSave = Combo_Grating
Settings(SpectrumCounter).WavelengthStartSave = WavelengthStart
Settings(SpectrumCounter).WavelengthStopSave = WavelengthStop
Settings(SpectrumCounter).WavelengthStepSave = WavelengthStep
Settings(SpectrumCounter).PointsToAverageSave = PointsToAverage
Settings(SpectrumCounter).ScansToAverageSave = ScansToAverage
Settings(SpectrumCounter).TemperatureValueSave = Temperature
Settings(SpectrumCounter).TemperatureStartSave = TemperatureStart
```

```
    Settings(SpectrumCounter).TemperatureStopSave = TemperatureStop
    Settings(SpectrumCounter).TemperatureStepSave = TemperatureStep
    Settings(SpectrumCounter).TemperatureBandSave = TemperatureBand
    Settings(SpectrumCounter).TemperatureTimeSave = TemperatureTime

Next Temperature

EDRE_DAWrite 1000033182, 0, 0

End Function
```

Appendix C – Publications and Conference Contributions

This study published or contributed to the following papers, during the period from 2015 to 2017:

- L. J. B. Erasmus, H. C. Swart, J. J. Terblans, R. E. Kroon, "Measuring the optical thermometry properties of La_2O_2S:Eu," *Proceedings of The 60th annual conference of The South African Institute of Physics*, pp. 422-7, 17 7 2016.
- L. J. B. Erasmus, H. C. Swart, J. J. Terblans, "Measuring the optical thermometry properties of La_2O_2S:Eu phosphor material," *South African Journal of Science and Technology*, vol. 35, no. 1, pp. 1, 29 7 2016.
- L. J. B. Erasmus, H. C. Swart, J. J. Terblans, "Determination of the optical thermometry properties of a phosphor material for application as an optical temperature sensor," *South African Journal of Science and Technology*, vol. 36, no. 1, pp. 1, 2017.
- B. P. Kore, A. Kumar, L. J. B. Erasmus, R. E. Kroon, J. J. Terblans, S. J. Dhoble, H. C. Swart, "Energy Transfer Mechanisms and Optical Thermometry of $BaMgF_4$:Yb^{3+}, Er^{3+} Phosphor," *Inorganic Chemistry*, vol. 57, pp. 288-99, 2018.
- J. Prakash, V. Kumar, L. J. B. Erasmus, M. Duvenhage, G. Sathiyan, S. Bellucci, S. Sun, H. C. Swart, "Phosphor Polymer Nanocomposite: ZnO:Tb^{3+} Embedded Polystyrene Nanocomposite Thin Films for Solid-State Lighting Applications," *ACS Applied Nano Materials*, 2018.

This study contributed to the following conferences, during the period from 2015 to 2017:

- South African Institute of Physics 2015 Conference, Poster Presentation, Port Elizabeth, Eastern Cape, South Africa.
- Die Suid-Afrikaanses Akademie vir Wetenskap en Kuns 2015 Studentesimposium, Oral Presentation, Bloemfontein, Free State, South Africa.
- South African Institute of Physics 2016 Conference, Oral Presentation, Cape Town, Western Cape, South Africa.

- International Conference on Physics of Advance Materials 2016, Poster Presentation, Cluj-Napoca, Transylvania, Romania.
- Die Suid-Afrikaanses Akademie vir Wetenskap en Kuns 2016 Studentesimposium, Oral Presentation, Potchefstroom, North West Province, South Africa.
- South African Conference on Photonics Materials 2017, Amanzi Private Game Reserve, Free State, South Africa.
- International Conference on Advanced Materials 2017, Oral Presentation, Bucharest, Muntenia, Romania.
- Die Suid-Afrikaanses Akademie vir Wetenskap en Kuns 2017 Studentesimposium, Oral Presentation, Pretoria, Gauteng, South Africa.

This study received the following conference awards, during the period from 2015 to 2017:

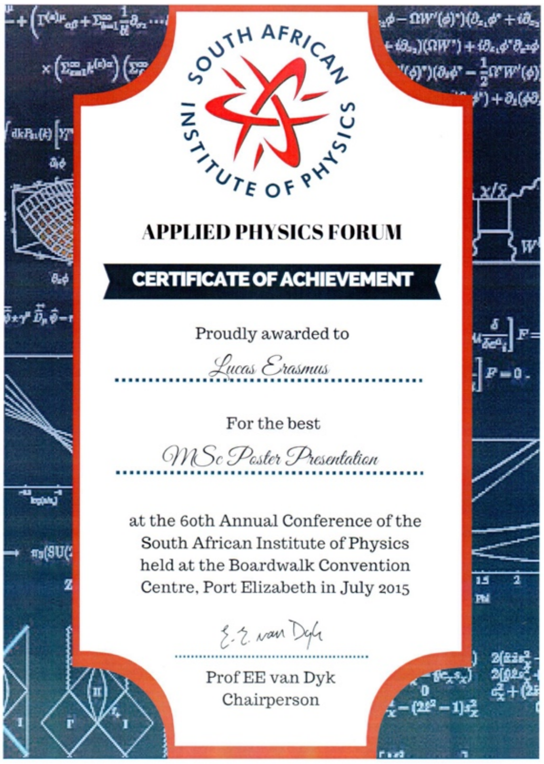
SOUTH AFRICAN INSTITUTE OF PHYSICS
APPLIED PHYSICS FORUM
CERTIFICATE OF ACHIEVEMENT
Proudly awarded to
Lucas Erasmus
For the best
MSc Poster Presentation
at the 60th Annual Conference of the South African Institute of Physics held at the Boardwalk Convention Centre, Port Elizabeth in July 2015
Prof EE van Dyk
Chairperson

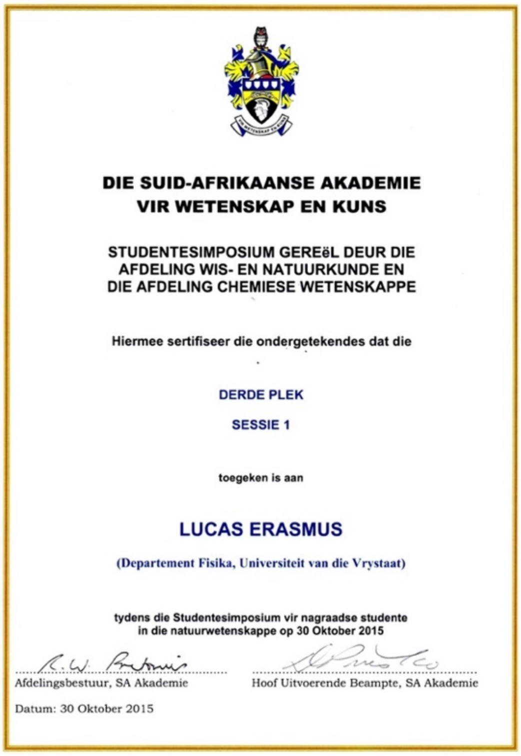
DIE SUID-AFRIKAANSE AKADEMIE VIR WETENSKAP EN KUNS
STUDENTESIMPOSIUM GEREëL DEUR DIE AFDELING WIS- EN NATUURKUNDE EN DIE AFDELING CHEMIESE WETENSKAPPE
Hiermee sertifiseer die ondergetekendes dat die
DERDE PLEK
SESSIE 1
toegeken is aan
LUCAS ERASMUS
(Departement Fisika, Universiteit van die Vrystaat)
tydens die Studentesimposium vir nagraadse studente in die natuurwetenskappe op 30 Oktober 2015
Afdelingsbestuur, SA Akademie
Hoof Uitvoerende Beampte, SA Akademie
Datum: 30 Oktober 2015

SOUTH AFRICAN INSTITUTE OF PHYSICS

APPLIED PHYSICS FORUM

CERTIFICATE OF ACHIEVEMENT

Proudly awarded to

Lucas Erasmus

For the best

MSc Oral Presentation

at the 61st Annual Conference of the South African Institute of Physics held at the University of Cape Town, Cape Town in July 2016

Prof EE van Dyk
Chairperson

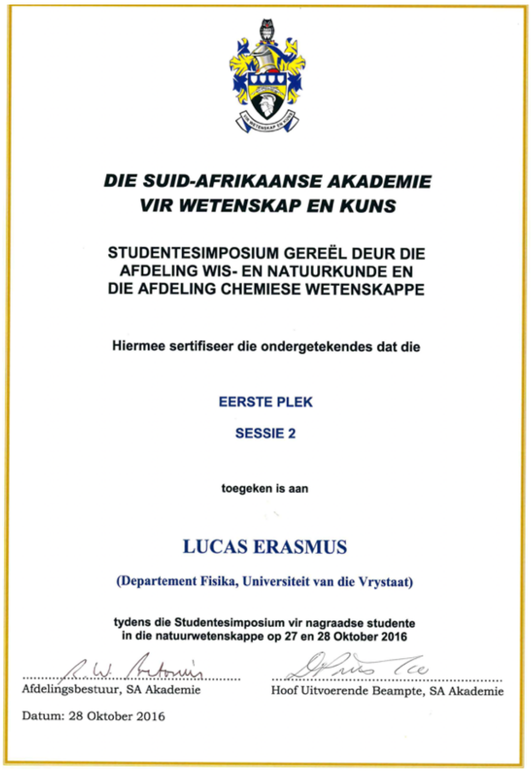

DIE SUID-AFRIKAANSE AKADEMIE VIR WETENSKAP EN KUNS

STUDENTESIMPOSIUM GEREËL DEUR DIE AFDELING WIS- EN NATUURKUNDE EN DIE AFDELING CHEMIESE WETENSKAPPE

Hiermee sertifiseer die ondergetekendes dat die

EERSTE PLEK

SESSIE 2

toegeken is aan

LUCAS ERASMUS

(Departement Fisika, Universiteit van die Vrystaat)

tydens die Studentesimposium vir nagraadse studente in die natuurwetenskappe op 27 en 28 Oktober 2016

Afdelingsbestuur, SA Akademie

Hoof Uitvoerende Beampte, SA Akademie

Datum: 28 Oktober 2016